DATING THE ATERIAN USING TECHNIQUES OF LUMINESCENCE DATING AND IMPLICATIONS FOR MAPPING THE DISPERSAL OF MODERN *HOMO SAPIENS*

VOLUME II

Laine Clark-Balzan

Research Laboratory for Archaeology and the History of Art
Keble College
University of Oxford

Thesis submitted for the degree of
Doctor of Philosophy

Michaelmas Term 2012

Chapter Six

SR-OSL Development

Two general methods are available for the measurement of spatially-resolved luminescence: imaging and scanning. Imaging may be thought of as taking a series of pictures of a sample in rapid sequence. A time series of intensity measurements is thereby obtained for the sample as a whole, whether it is a slice of rock, brick, pottery, or resin-impregnated sediment. The other method available involves scanning a light source over the sample and recording luminescence curves point-by-point as the sample is stimulated. The bonus of this method is that the highly sensitive PMT can be used to sense emitted photons, since one knows precisely the laser position and therefore where in the sample they are being emitted. This type of measurement can be extremely slow, however, as about a second of measurement per point will be necessary, and one may measure many hundreds of points per sample. In addition, crosstalk between neighboring grains cannot be excluded, as the light emitted from one grain may trigger another to emit luminescence as well. For this reason, and because of recent technological advances, a proof-of-concept study was conducted to investigate the feasibility of imaging luminescence.

This chapter records a feasibility study of imaging luminescence with electron multiplying charge-coupled device (EMCCD) cameras. A portion of this chapter has been published by Clark-Balzan and Schwenninger (2012).

6.1 Imaging and luminescence

To be competitive with photomultiplier tubes, an imager must detect signal in broadly the same regime of wavelength, low light intensity detection, and with temporal and spatial resolution sufficient for the intended applications. Though previous SR-OSL attempts were hampered by inherent limitations in the technology of the time (see section 6.1.2), recent advances necessitate another look at the possibilities of imaging OSL.

6.1.1 Imaging requirements

Quartz and feldspar emission spectra have been investigated thoroughly. Quartz emits photons primarily in blue (approx 470 nm) and orange-red bands (approx. 620 nm) during TL (Krbetschek et al., 1997), though either band can be dominant (Kuhn et al., 2000). Emissions in the UV band during TL are <1% of the intensity of the blue band emissions (Kuhn et al., 2000). During quartz OSL, the intensity of the emissions increases with increasing stimulation light energy (Bøtter-Jensen et al., 1994; Kuhn et al., 2000), but there seems to be only one emission band either around 360nm (Huntley et al., 1991) or 380 nm (Martini et al., 2009; Stoneham and Stokes, 1991). Feldspar emissions are similar for both TL and IRSL, and dominant peaks have been noted in blue (400-420 nm) and yellow (550-570 nm) bands (Bøtter-Jensen et al., 1994; Huntley et al., 1991; Krbetschek and Rieser, 1995). Again, the chemical composition of the feldspars seems to dictate the dominant emission band. Ultraviolet, green, and IR emissions have been noted as well, and indeed it seems to be much more difficult to draw general conclusions about behavior across this mineral family (see review by Krbetschek et al., 1997).

Absolute emission intensity of either quartz or feldspar is difficult to find in published material, but feldspar emissions are known to be several orders of magnitude brighter than quartz and grains of quartz can vary by orders of magnitude within the same sample. It has been

suggested that stimulation light intensity is approximately 10^{18} times greater than emissions (Risø DTU, 2009). Emission intensity decreases with increased temperature for quartz (thermal quenching), but increases up to 175°C and then decreases for feldspar (thermal assistance) (Duller, 2003).

OSL or IRSL decay rate depends on the sample, temperature, and optical power density. Broadly, for standard Riso measurements of blue LED OSL (approximately 36 mW cm^{-2}, 125°), the majority of the quartz signal will have decayed after several seconds, whereas feldspar emissions for blue LED stimulation and IRSL takes several tens of seconds. Single grain laser measurements (50W cm^{-2}, 125°) can be completed in a second. Conversely, during pulsed blue light stimulation, most of the feldspar signal has decayed after several tens of microseconds and quartz after several hundred (Ankjaergaard et al., 2010). Quartz OSL signals decay more quickly with higher temperature, however feldspar has no significant change in decay rate with temperature (Duller, 2003).

6.1.2 Previous research in SR-OSL

Attempts to record the spatial distribution of luminescence in a sample have been made since the 1980's with varying degrees of success. Both scanning and imaging systems have been investigated by Risø (Markey et al., 1997), and a scanning system was developed into today's single grain measurement equipment (Duller et al., 1999). A similar system was incorporated into the Daybreak OSL reader (Bortolot, 2000). Another laser scanning system has been successful at mapping spatially resolved OSL of quartz crystals, Al_2O_3:C, porcelain, brick, and concrete (Bailiff, 2006; Bailiff and Mikhailik, 2003). Confocal microscopy, which also allows depth discrimination, has been used to record OSL from Al_2O_3:C (Gaza et al., 2006) and is being developed further (DeWitt and Klein, 2009).

Only recently has imaging technology become sensitive enough to compete with scanning methods. Early attempts required the building of specialized detectors, several of which incorporated film-based cameras (Debenham et al., 1982; Hashimoto et al., 1986, 1987,

2002; Malik et al., 1973; Templer, 1986; Walton and Debenham, 1980, 1982). Another approach utilized a bialkali photocathode and a microchannel plate to detect spatial intensity patterns (Burggraaf and Haskell, 1994; McFee, 1995). These detectors were slow, difficult to work with, and typically only measured TL. More recently, scientific CCDs have been used to image TL (Olko et al., 2008; Spooner, 2000) and IRSL (Baril, 2004; Duller et al., 1997; Greilich, 2004; Greilich and Wagner, 2006; Greilich et al., 2002, 2005) from a variety of samples (quartz, porcelain, granite slices and feldspars, among others). The majority of the experimentation has focused on detecting luminescence emissions in visible wavelengths, with some exceptions. Duller et al. (1997) recorded combined UV and visible emissions during IR stimulation of feldspar by using a camera coated with a UV phosphor and a BG-39 filter (approx. 300-600nm; 1 second exposures). Greilich et al. (2002) managed to detect and record UV emissions from feldspar in granite slices, however, comparisons of SEM scans with the luminescence map show that negligible emissions were recorded from quartz in the same slice. Finally, UV band luminescence detection has recently been reported by McCulloch et al. (2011), utilizing a Princeton Instruments CCD detector. Other recent work has focused on the potential of EMCCDs, with imaging of infra-red radiofluorescence measurements on feldspar (Pfeifer and Krbetschek, 2009) and TL from siliceous rock slices (Schmidt et al., 2010).

6.1.3 Modern imaging technology

Current scientific imaging devices incorporate one of four main types of signal detection architecture:

-standard charge-coupled device (CCD)

-electron multiplying charge-coupled device (EMCCD)

-intensified charge-coupled device (ICCD)

-complementary metal-oxide semiconductor (CMOS) sensor.

The last, CMOS technology, is a type of signal integration device that is used in most low-cost digital cameras. The most significant difference between CMOS and CCD sensors for our

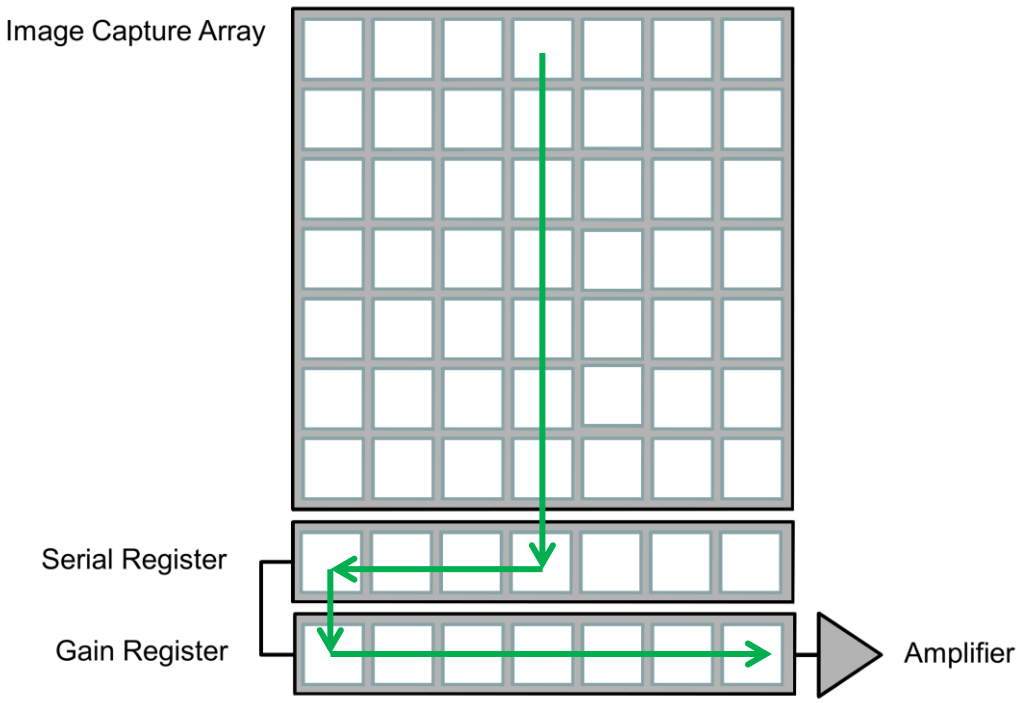


FIG. 6-1. CCDs comprise an array of potential wells called 'pixels' (white squares), which collect and store charge. Rows of charge are transferred vertically down the chip into the serial register, after which each row is transferred horizontally (green line). An EMCCD includes a 'gain register' before the charge is read out at the amplifier and analog-to-digital converter. In this register, the signal is multiplied many times during each pixel-to-pixel transfer.

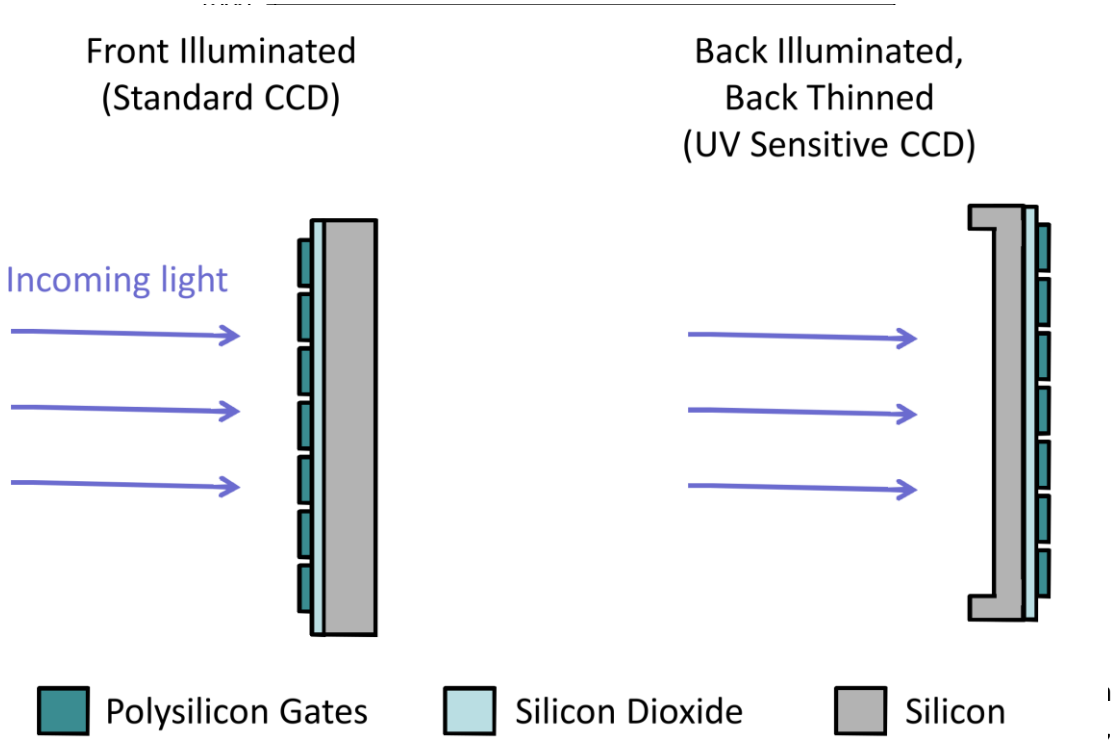


FIG. 6-2. Schematic diagrams of front-illuminated and back-illuminated CCDs. Since silicon strongly absorbs UV light, decreasing the distance travelled in the chip increases the UV sensitivity.

purposes lies in signal read-out: a CMOS can be read out from each pixel simultaneously rather than from a single node as with a CCD. Though this architecture allows much higher frame rate, CMOS sensors may have significantly higher noise values than CCDs and problems with linearity across the sensor (Magnan, 2003). The first scientific grade CMOS cameras have only been introduced over the past year, and the technology is relatively untested in quantitative applications. Hence, we will focus on CCD-based imaging in the following discussion.

The basic CCD is a three layer sandwich of material: polycrystalline silica gates, a silicon dioxide insulating surface, and then a semiconductor substrate (Fig. 6-2). Voltages applied at the gates create a grid of potential wells, or pixels. For a standard CCD, incident photons must travel through the gates and SiO_2 to reach the photosensitive region of the chip. Here, photons boost electrons from the silicon into the conduction band with a certain efficiency ('quantum efficiency', QE). The electrons migrate into the closest potential well, creating charge packets that are stored until transferred serially to a readout register and digitization node. Low light imaging with a CCD sensor is limited by the signal to noise ratio of each pixel:

$$\frac{S}{N} = \frac{QE * P}{\sqrt{QE * P + D + \delta_{read}^2}}$$

where P is the number of incident photons (desired signal plus any background light), QE is the quantum efficiency, D is the dark current level, and δ_{read}^2 is the read out noise (up to several tens of electrons per pixel). Photon ('shot') noise is inherent to the desired signal as photon arrival and capture is a statistically uncertain process governed by the Poisson distribution; this noise source cannot therefore be eliminated. Dark noise can be virtually eliminated by now-standard chip cooling and fast frame rates. Therefore, if one holds the imaging light intensity constant, the signal to noise ratio can be increased by either decreasing the read-out noise contribution to the final digitized signal (via binning of pixels or sensor architecture changes) or enhancing the QE of the detector.

To return to the types of imaging detector mentioned above, both ICCDs and EMCCDs apply gain to the signal so that the relative contribution of read-out noise is negligible. ICCDs incorporate an image intensifier, which is coupled to a CCD chip by either fiber optics or with a lens (Moomaw, 2007). Within the image intensifier, incident photons strike the photocathode, causing photoelectron emission. These electrons are accelerated through a micro-channel plate (MCP), a "honeycomb" of coated glass channels. As the electrons travel through the MCP, secondary electrons are created, thereby boosting the signal. Signal gain depends on the voltage applied. EMCCDs exploit “clock-induced charge,” a source of noise in CCDs that occurs when a charge that is being transferred causes ionization of the substrate, producing another charge. This effect is so slight as to be virtually undetectable in modern, standard CCDs, and is therefore usually neglected in noise calculations. EMCCDs incorporate a gain register, however, where signals are transferred by enough excess voltage to substantially boost the signal. Signal multiplication by approximately a thousand times is common (Ingley et al., 2009).

The signal to noise function is now different:

$$\frac{S}{N} = \frac{M * QE * P}{\sqrt{F^2 * M^2(QE * P + D + \delta_{CIC}^2) + \delta_{read}^2}}$$

In this case, the desired signal has been multiplied by *M* times, but so are electrons due to dark current and a new source of noise that was negligible in a standard CCD—clock induced charge. Furthermore, the multiplication process has its own associated noise, an ‘excess noise factor,’ that is introduced (F^2 approaches 2 as M gets larger) (Robbins and Hadwen, 2003). The effective readout noise, however, is near zero with high M. If readout speed and gain are kept constant, the magnitudes of M, F, δ_{read}, and δ_{CIC} will also remain stable. Dark noise will increase with exposure time (assuming good temperature stability), and photon noise will increase with signal (exposure time, or for OSL: more stimulation light breakthrough or brighter luminescence).

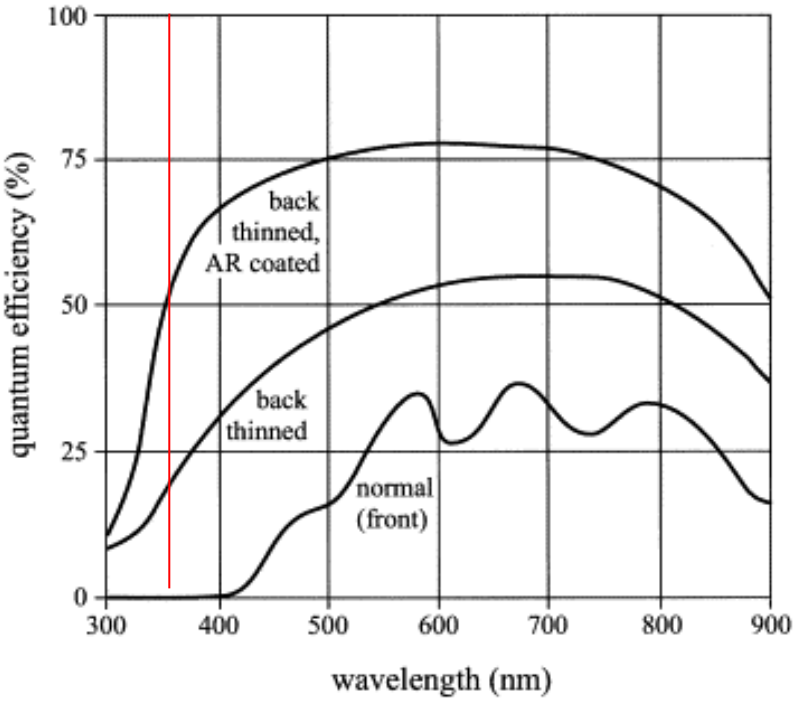


FIG. 6-3. Quantum efficiencies (typical) for a standard front-illuminated CCD, a back-thinned/back-illuminated CCD, and a back-thinned, AR coated CCD. The wavelength under consideration (UV emission of quartz) is indicated by the red line. Figure adapted from Berland et al. (2003).

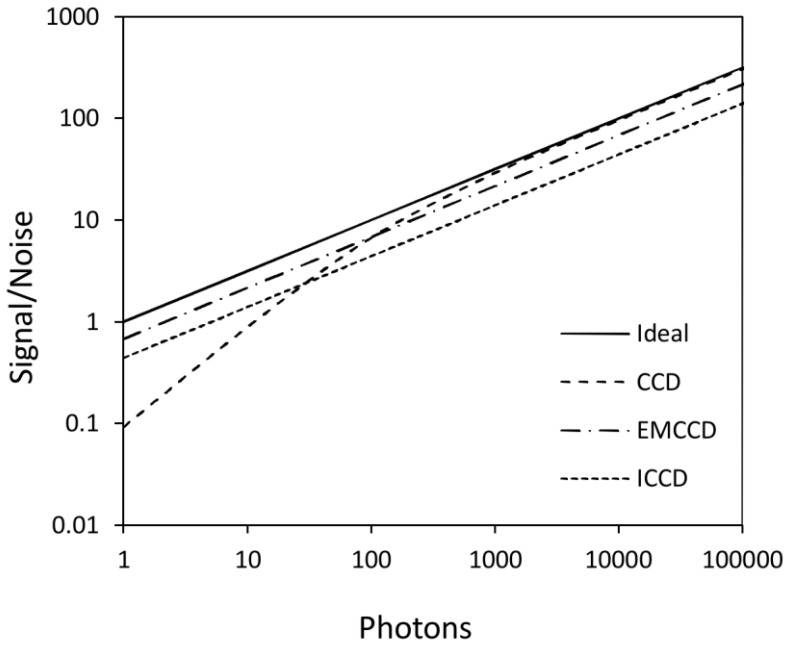


FIG. 6-4. Signal to noise ratios for various imaging detectors. Values used for the calculation are those suggested by Andor Technology (2012). At low signal levels (several tens of photons), the EMCCD has the highest signal to noise ratio.

When typical noise values are entered into the above equation, both ICCDs and EMCCDs have higher signal to noise ratios than a standard CCD at low light levels (Fig. 6-4). ICCD cameras can have exposure times on the order of nanoseconds by high-speed voltage switching (allowing electrons to travel through the MCP or not), but resolution is limited by the size of the MCP channels. When frame rates do not need to be that high, EMCCDs may be a better choice, as they have higher signal to noise than ICCDs in certain situations and typically have higher QE as well. Furthermore, and not inconsequentially, EMCCDs are usually about half the price of ICCDs. As stated previously, signal to noise can also be improved by raising the quantum efficiency of the CCD sensor. This is particularly necessary for UV imaging, as the QE of a standard front-illuminated CCD is almost nil below about 400 nm (Fig. 6-3). Standard front-illuminated CCDs are insensitive to UV both because the polysilicon and silicon dioxide layers strongly absorb light in these wavelengths and because no anti-reflection coatings can be applied.

Two methods have been designed to circumvent these issues. The first involves coating a chip with a phosphor that downconverts incident UV light to higher wavelength emissions (Blouke et al, 1980). While this has the advantages of being relatively simple and therefore cheap, the QE remains relatively low because as much as 50% of the downconverted light may be re-emitted away from the sensor. Hence, the maximum QE is typically half of the sensor's QE at the down-converted wavelength.

The second option, which may be used in conjunction with the first, flips the CCD sensor so that light does not have to travel through the gates (Fig. 6-2). These are known as back-illuminated sensors. UV wavelengths are still strongly absorbed by the silicon substrate, however, so that the signal may be entirely absorbed before reaching the photoactive potential wells. Most often, such chips (several hundred nanometers thick) are therefore thinned to between 10 and 30 nm, producing a back-thinned, back-illuminated chip. Because of the high failure rate during thinning of CCD sensors, this process makes the chip much more expensive. Yet a back-thinned, back-illuminated CCD offers the best QE possible for ultraviolet imaing, and

this may be enhanced further with special coatings. For instance, anti-reflection coatings are often applied, as silicon's high index of refraction can make reflection a significant problem in UV imaging.

With current technology, then, a back-thinned, back-illuminated, coated, EMCCD sensor offers the best possibility of imaging quartz OSL (Fig. 6-3, 6-4). This does create other problems such as the difficulty of imaging red wavelengths, as the absorption length of red light is greater than the thickness of a thinned chip. In general, however, if one can image UV OSL, then one will be able to image any other type of OSL or TL with the same system. Successful imaging, up to an EMCCD camera's potential limit of several hundred frames per second depends on the absolute intensity of the OSL emissions and the efficiency of the optics and filtering. The ultimate determination of an EMCCD's usefulness for a variety of OSL samples will become apparent through experimentation.

6.2 Methodology

Once EMCCD technology had been identified as most viable, several EMCCD cameras were obtained for initial testing: ImagEM (Hamamatsu), iXON (Andor), and Sensicam UV (PCO Imaging) (Fig. 6-5). The primary goal of these trials was to verify that an EMCCD device would be sensitive enough to register UV OSL emissions at a frame rate that would provide decay curve resolution. Each trial occurred over at least a week, and involved numerous tested combinations of filters, lenses, samples, stimulation light, and types of image series. Differences in available equipment during each trial (notably lenses) and uncontrollable variables in each set-up rendered quantitative comparisons between camera trials impossible. It was apparent, however, that UV emissions were detectable via EMCCD from both synthetic dosimeters and natural quartz. After these initial tests, a Rolera MGi camera was acquired and used for all further experimentation.

Three sample types were used to test the feasibility of measuring UV SR-OSL with EMCCDs: carbon-doped aluminum oxide grains (Al_2O_3:C: 200 μm), purified quartz extracts (Dar

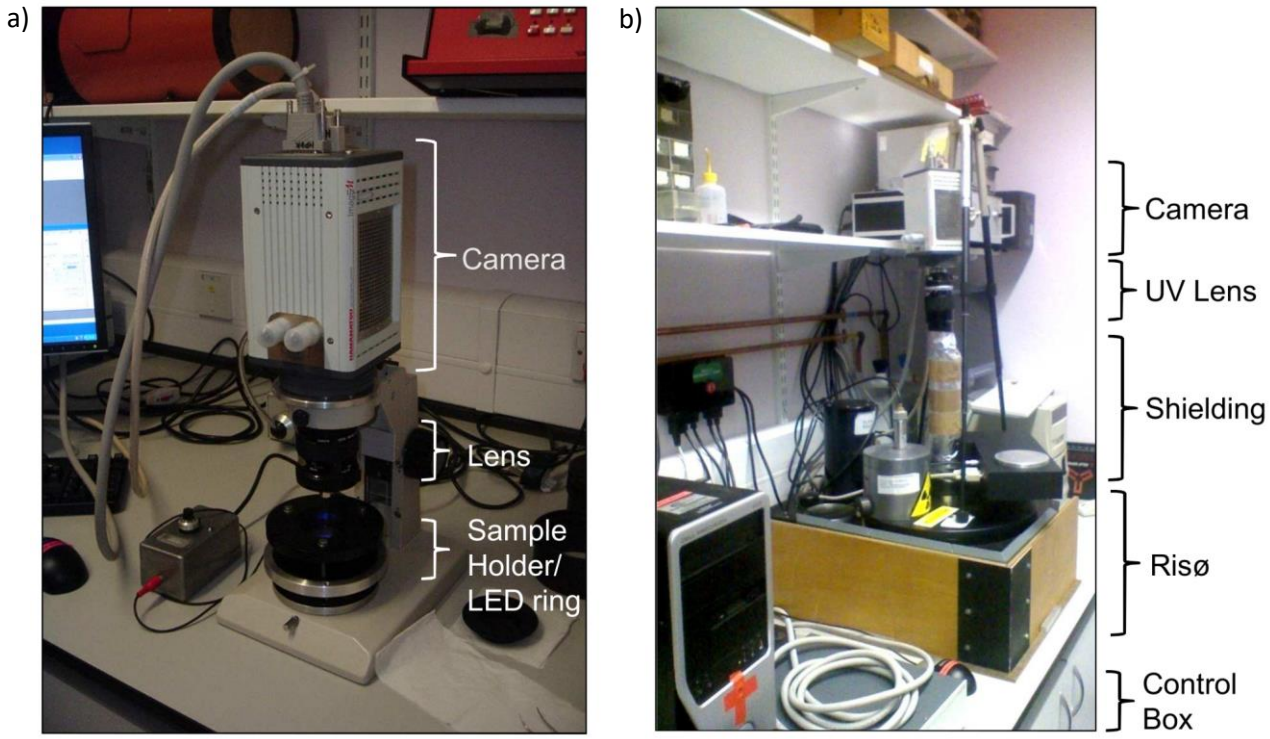


FIG. 6-5. Bench top (a) and Risø (b) EMCCD systems during the first EMCCD trial. Traditional photographic lenses were used, which significantly increased the working distance (distance from sample to front of lens). A better optical system was used for later experiments, but other basic system components remained essentially the same.

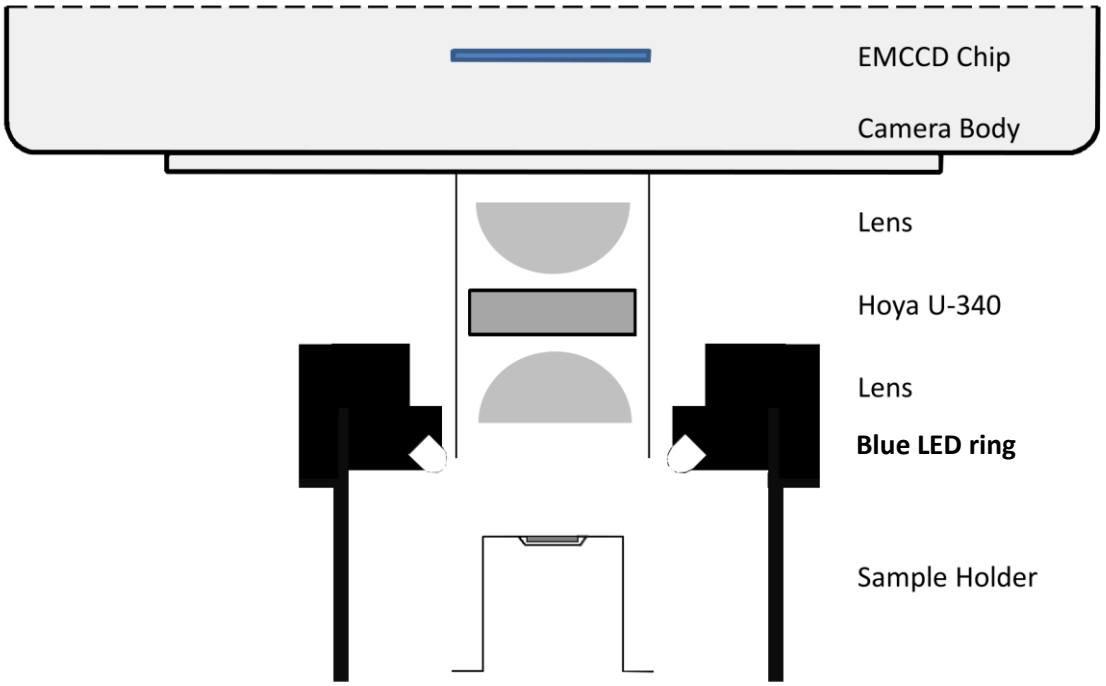


FIG. 6-6. Schematic of optics and bench-top sample holder/stimulation ring. Lenses are fused silica and anti-reflection coated (1 inch diameter, f=35 mm).

es-Soltan I, Morocco:180-255 µm; Risø calibration quartz: 180-255 µm), and sandstone slices (Stanton Moor, Dale View Quarry). Details of the Dar es-Soltan samples have been published previously (Barton et al., 2009). They are primarily pure quartz with occasional feldspars, bright, with good SAR characteristics. Grains (Al_2O_3:C or quartz) were attached with silicone oil to aluminum discs in a 3 to 4 mm diameter monolayer. Sandstone slices were first cut with a water-cooled saw, then ground to a thickness of approximately 2 mm and cut into a 1 cm diameter chip. During measurements, these slices were placed directly upon the heater/lifter. The sandstone slices have not been previously characterized.

Images were captured with a Rolera-MGi EMCCD camera (QImaging), which uses a frame transfer, e2V CCD97 back-illuminated sensor from L3Vision. The sensor has a photoactive area of 512 x 512 pixels, with each pixel measuring 16x16 µm square. The Rolera-MGi is Peltier cooled to -25˚C. Images were taken at maximum EM gain (signal multiplied approximately 1200 times), and read out at 10MHz, with 14 bit analog to digital conversion. Image acquisition was controlled by QCapture Pro, with FireWire connection between the camera and PC.

Camera optics were simple, comprising two fused silica, anti-reflection coated, plano-convex lenses (1 inch diameter, f=35 mm), as in Duller et al. (1997) (Fig. 6-6). This arrangement provides the most aberration correction with the fewest lens elements and ~1:1 magnification. Lenses were focused with a UV LED torch. Three Hoya U-340 filters, each 2.5 mm thick, separated stimulation and emission wavelengths. Two stimulation systems were used: a simple lab bench unit and a Risø Minisys TL/OSL-DA-15 reader. The lab bench system consisted of a sample base and a blue LED ring for stimulation. To use the camera with the Minisys, the PMT was removed, and the camera was positioned over the heating/lifting strip. Optical stimulation and heating were provided by the Minisys. The Minisys was also used to beta irradiate the multigrain aliquots, but the sandstone slices were irradiated in an external ELSEC irradiator. Synchronization in both systems was user controlled: programmed image sequences and optical

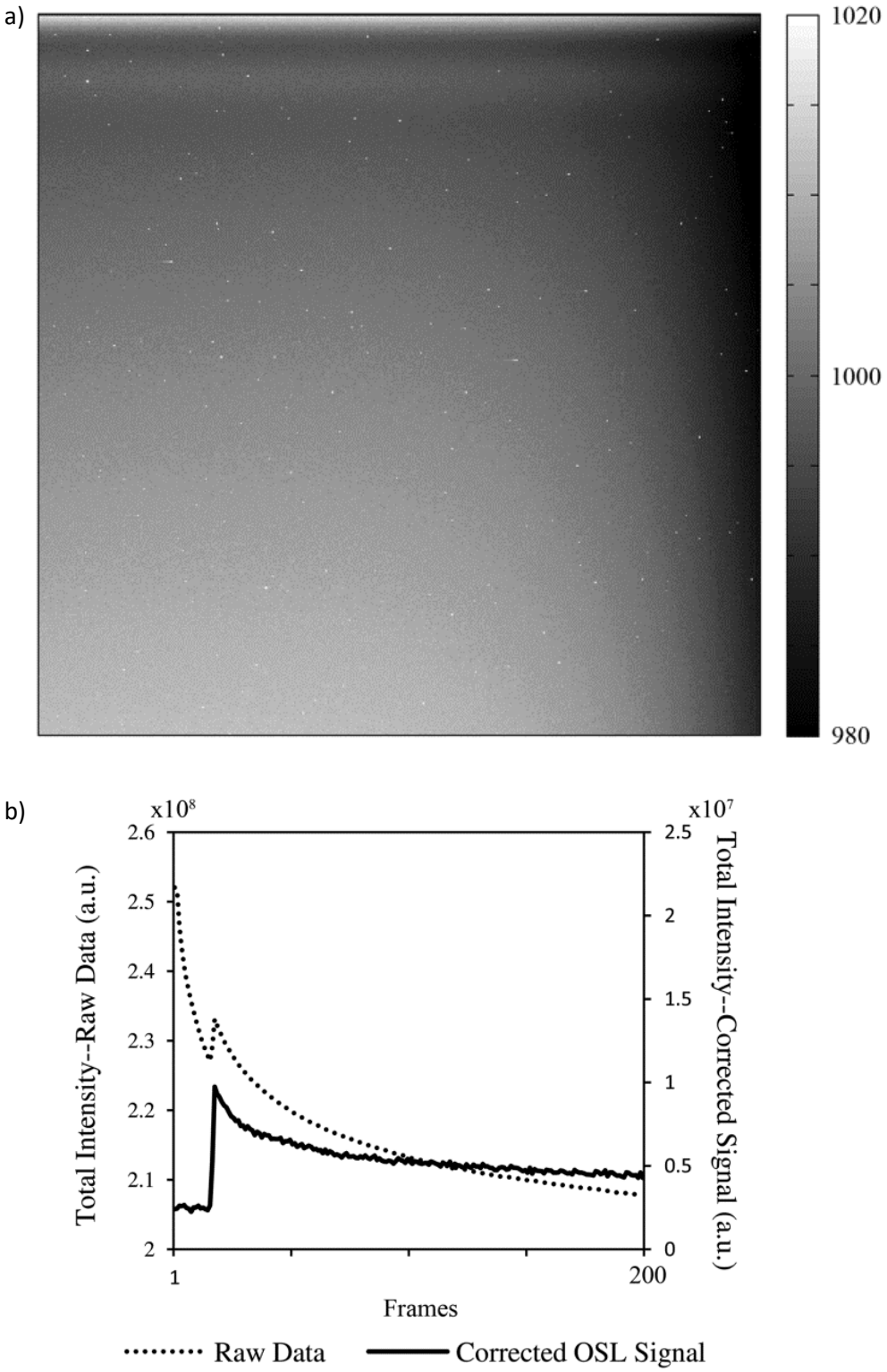


FIG. 6-7. EMCCD camera characteristics. a) An image of a 100 ms master dark frame, which includes patterned noise such as individual 'hot' pixels and overall sensor non-uniformity. This was created by scaling each frame to account for bias instability, then taking the median of 500 dark images. The bias signal is a value added at read-out to ensure digitization does not result in negative values. b) Total frame intensity data for a sequence of aluminum oxide OSL images (0.66 Gy dose). Raw data (dashed line) includes OSL emissions, dark noise, and a bias value that changes over time. The corrected OSL data (solid line) has been processed to remove dark noise and account bias instability (see Section 6-2 of text for details).

stimulation or heating were initiated separately by the experimenter. In order to record the initial emission peak, image sequences were begun several seconds before stimulation.

Post-processing of the digitized images was conducted in MATLAB. All image data (excluding the Dar es Soltan quartz images, Fig. 6-8) has been processed with basic techniques. Each OSL or TL cycle was recorded as an image sequence (see each section for exposure times and number of frames). To correct for bias instability and dark current build-up, master dark frames were created with exposure times corresponding to those used during OSL measurement. The offset between the master dark frame and each image sequence frame was determined by comparing median pixel values in two light-free portions of the sensor, after which the scaled master dark was subtracted from the emission image (see Fig. 6-7 for sensor variation). Otherwise, intrinsic system noise has not been characterized extensively, as it is believed that synchronization of imaging and stimulation produce the largest error (see Fig. 6-11 and discussion in Section 6.2.2.1).

OSL signals are in arbitrary grey-scale units, found by integrating pixel intensities over the chosen number of frames and the desired region of interest (ROI). ROIs were created by either thresholding an appropriate image or binning a desired number of pixels (in a square region). To create the first type of ROI, which can be used to isolate either individual grains or select the entire aliquot, an image (TL or OSL) of the aliquot with good grain visibility was chosen. A median filter was then applied to the image (typically a 3x3 window) in order to decrease the image noise. After this, the operator selected a threshold value that distinguished between the background disc and grains or between dim and bright grains (depending on the ROI desired), and an image mask created: a matrix of zeros for regions with signal intensity less than the threshold and ones for those with greater signal intensity. If necessary, interior 'holes' were filled (e.g. for the whole aliquot ROI). The image mask was then applied to the raw data, after which all pixels were summed to find the luminescence intensity for that ROI per frame.

Median filters were also used to aid image interpretation in Section 6.2.1, however, quantitative data in Section 6.2.2 was not processed in any way except for dark noise/bias removal.

Details on particular integration limits for signals vary with experiment and are given in the next section. OSL background comprises later OSL emission and reflected stimulation light, and a mean value is often subtracted from the initial signal to obtain the net signal. Here, background was not subtracted for quantitative assessments (Section 6.2.2), but it was subtracted for IR and OSL images of the sandstone slice (Section 6.2.1) to aid visual inspection. Registration of images was unnecessary for these experiments.

6.2.1 Images

The sensitivity of the current system is apparent in the selection of images (Fig. 6-8, 6-9), representing two sample types and the two optical stimulation systems. Raw images of Dar es-Soltan quartz taken with the lab bench system are shown in Fig. 6-8. Each of these images is a 20 s exposure taken at room temperature. Two natural-dose, multigrain aliquots are shown from each of the following samples: SOL1-05-01, SOL1-05-08, SOL1-05-14. Previous measurements on these samples resulted in equivalent doses of 74.1 ± 3.2 Gy, 147.6 ± 6.1 Gy, and 44.0 ± 2.3 Gy, respectively (Barton et al., 2009). The discs were not preheated or subjected to IR stimulation previous to these images. It is important to note that these images are not the result of any screening for the brightest discs or best images. These frames are the first that were taken after deciding upon an appropriate exposure time. Background reflections from the disc and lens have been removed by applying a morphological opening operation using a linear structuring element (Obara, 2007), then the images have been median filtered (5x5 window). Individual grains are readily visible, and intensity variations both within and between samples are clear.

Fig. 6-9 displays the signals that would be used in an SR-OSL dating study. These images depict net luminescence signals from a sandstone slice, obtained in conjunction with the Risø Minisys during standard, sequential preheat (260˚C), IR (100 s, 50˚C), and OSL measurement

cycles (100 s, 125˚C). After daylight bleaching, the sandstone slice was dosed to approximately 400 Gy. Each image sequence comprised 90 (TL) or 200 (IR/OSL) consecutive images with 500 ms exposure times. Net signals were obtained by integrating data over a suitable time period (IR and OSL: frames 6-25, TL: frames 31-90) and subtracting mean background (IR and OSL: frames 41:200, none subtracted for TL). The TL signal shown here is, of course, the unstable 110˚C peak, which would not be used for dating. No filtering was applied. Representative glow and decay curves were obtained by summing pixel intensities over two regions of interest: total displayed sensor area and the indicated single grain. All images have been cropped from the full sensor region; approximately one-quarter of the sensor is shown.

Both sets of images contain clearly defined grains (~30 pixels per grain) emitting UV band luminescence above background levels. Significant variation in grain brightness, between and within samples, is immediately apparent. The strongly emitting grains present in the Dar es-Soltan aliquots (Fig. 6-8 a, e) and indicated in the sandstone slice (Fig. 6-9) are likely to be feldspar. Characteristics indicative of feldspar have been seen in several of the Dar es-Soltan I samples previously (Barton et al. 2009), and earlier experiments with the camera and Risø reader indicated the presence of grains with significant IRSL. The relative strength of the quartz and presumed feldspars is apparent in both the images' color maps and the size of the reflection halo around the feldspar grain (multigrain aliquot). Exposure times must be based on the signal levels of the majority of the grains in a sample.

The image sequences taken during TL, IR, and OSL of the sandstone slice show the potential of the EMCCD as a measurement device. Over fifty distinct grains are apparent in the TL image, several in the IR image, and over fifteen in the OSL image. Decay and glow curves show characteristic, expected intensity changes over time. With 500 ms exposures, the curves have been sampled at reasonable frequency. Importantly, grains are well defined and correlation of particular grains between various images is possible. The quality of these images demonstrates that, with appropriate sample marking, subsequent investigations of the sample

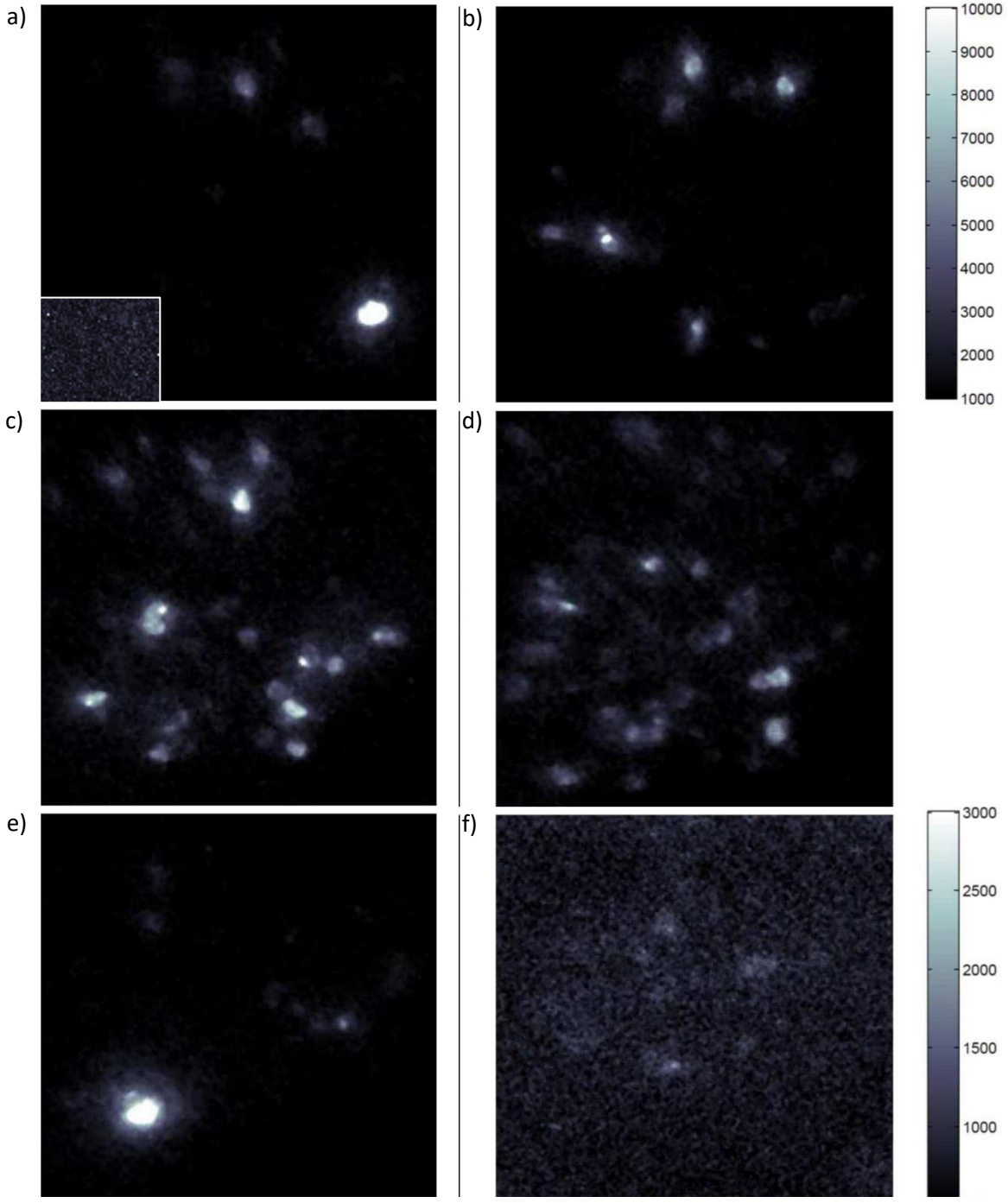


FIG. 6-8. Images of natural OSL signal from Dar es-Soltan I multigrain aliquots recorded with the bench-top mount at room temperature (20 second exposures). These images have been filtered for ease of visual grain identification (see text for details); for comparison, the inset box in a) shows a portion of the raw image which includes all noise. All images but f) use the colorbar displayed beside b); a different scale is used for f) so that the grains can be seen. a, b) SOL1-05-01: 74.1 ± 3.2 Gy. c, d) SOL1-05-08: 147.6 ± 6.1 Gy. e, f) SOL1-05-14: 44.0 ± 2.3 Gy. All equivalent doses are taken from Barton et al. (2009).

Sandstone Slice, Risø Minisys

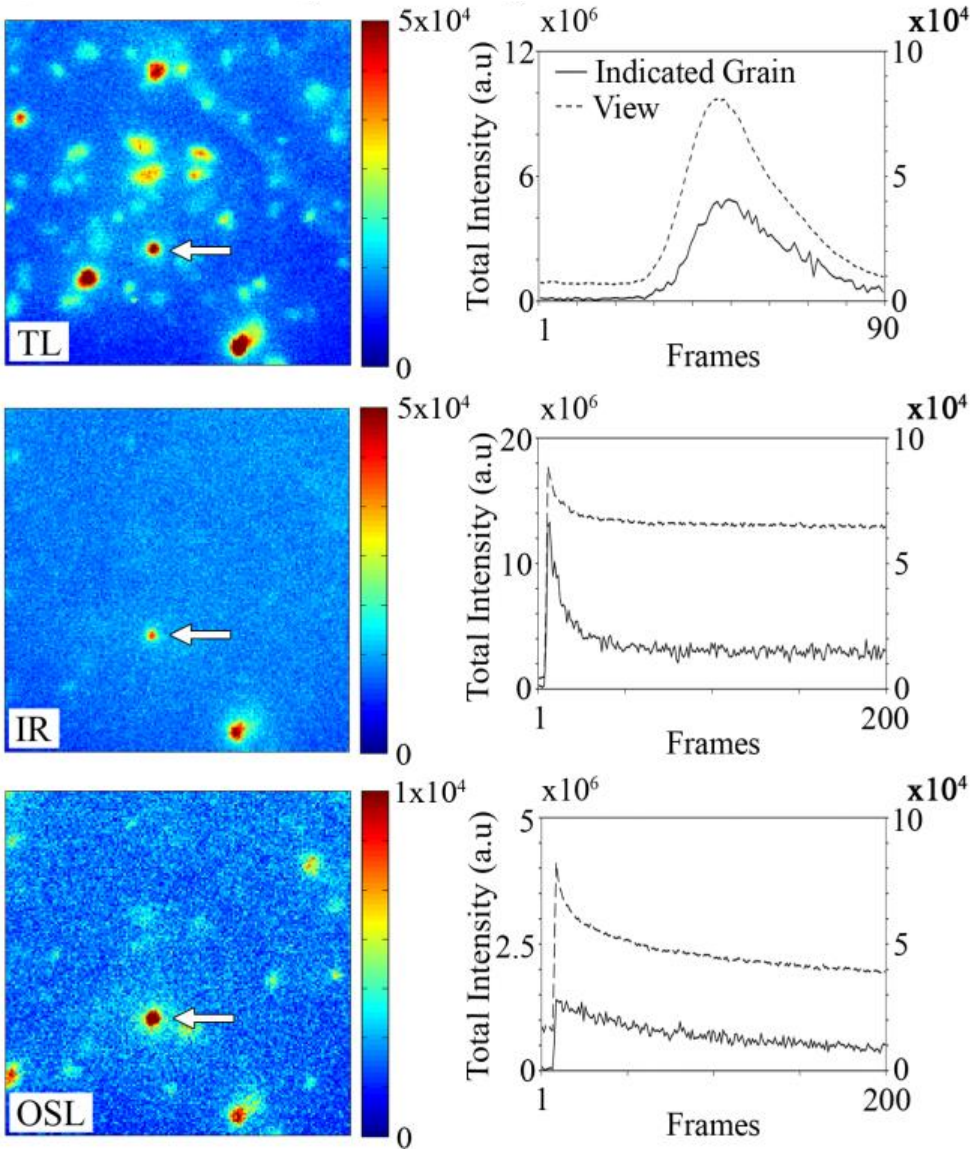


FIG. 6-9. TL, IR, and OSL net signal images and shine/decay curves (whole image region and indicated grain) for a bleached sandstone slice dosed to ~400 Gy. TL, IRSL, and OSL time series are shown for both the indicated grain, and the total image view. Exposure time was 500 ms.

could be readily correlated with luminescence measurements. The sandstone images also show the characteristic noise patterns produced by an EMCCD. Low intensity noise, apparent in the background of the TL image, is due primarily to intrinsic camera characteristics. The overall background and noise level is higher in the IR and OSL images due to imperfect filtering of the stimulation light. The signal to noise ratio of a measurement will change dramatically depending on the scale of analysis that is chosen. This is demonstrated in Fig. 6-9, with the comparison of decay and glow curves created by integrating across the two ROIs. As expected, more noise is apparent in the lower intensity, single grain ROI measurements.

6.2.2 Dose recovery

6.2.2.1 Al_2O_3:C

A repeatability experiment was performed with a multigrain aliquot (3 mm diameter) of 200 µm aluminum oxide grains. The aliquot was irradiated in sets of five repeated doses: 0.66, 1.31, 2.63, 5.25, and 10.5 Gy. One extra dose point was given in the 1.31 Gy set as a dose recovery test. Irradiation steps began with the lowest dose, repeated until all dose points at that level had been given, and increased sequentially. Between each irradiation the disc was bleached with blue LEDs for 300 s at 25˚C, and image sequences at maximum gain were recorded (200 frames, 100 ms exposure).

A whole aliquot ROI (Fig. 6-10a) was created by median filtering and thresholding a 0.66 Gy OSL image sequence (150 frames). After bias and dark current were subtracted from each sequence, the frame corresponding to the onset of luminescence was identified. Each OSL signal was calculated by integrating over the chosen ROI for 150 frames beginning with the onset of emission.

The resultant growth curve, including all 25 data points, and a representative decay curve are shown in Fig. 6-10b. The data is fitted closely with a linear equation and returns a high coefficient of determination, as expected for aluminum oxide in this dose range. The recovered dose for the additional dose point is 1.32 Gy, a difference of only 0.2% from the given dose

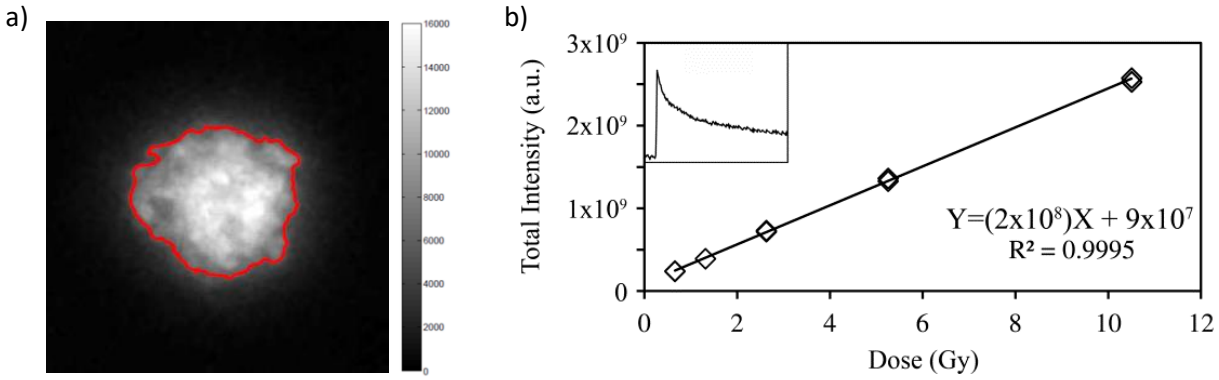


FIG. 6-10. Replicability experiment with Al_2O_3:C grains. a) Median filtered image of grains (0.66 Gy) with aliquot ROI indicated (red line). Individual grain boundaries are difficult to distinguish due to the close packing and constant intensity of each grain. b) Repeat OSL signal data (5x per dose step) this aliquot. A representative OSL decay curve (0.66 Gy) is shown inset.

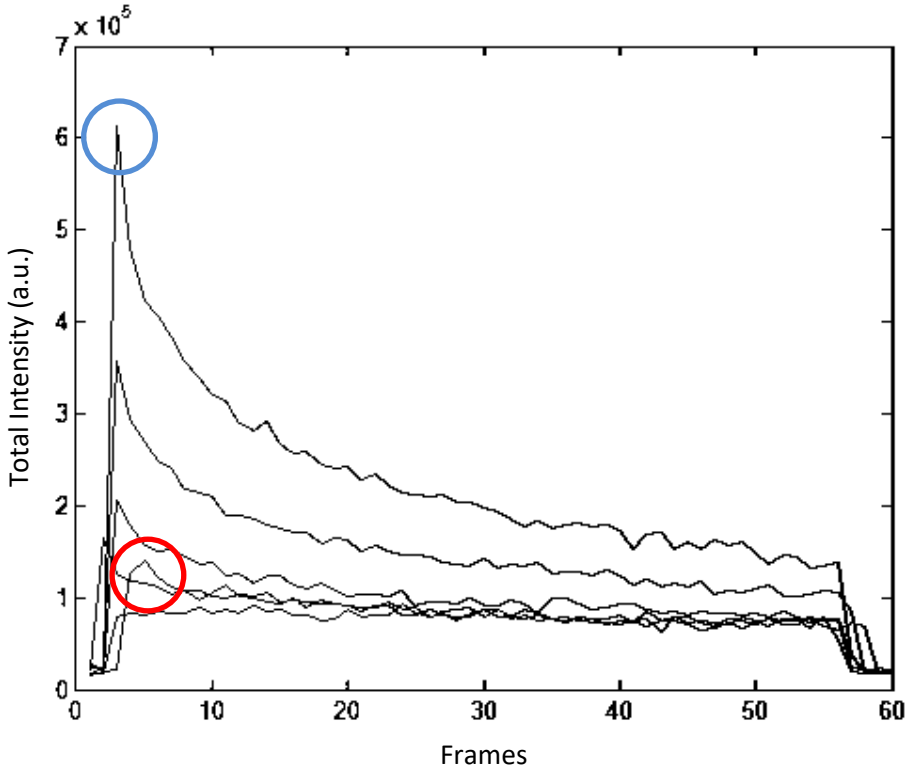


FIG. 6-11. Error induced via user-controlled image recording. OSL decay curves have been derived for the same aliquot from multiple image sequences recorded after repeated irradiation. Initial peak shape, however, varies significantly. In the case of the blue circle, optical stimulation was initiated near the beginning of a single exposure; by the next exposure, luminescence emissions had decreased. Conversely, the red circle indicates a less successful recording: optical stimulation began near the end of an exposure, so that luminescence emission increases in the next frame. These variations in signal recording combine to limit the precision of OSL SAR measurements, and highlight the importance of imaging/stimulation synchronization.

before rounding. The standard deviation of each dose set tends to increase as the signal level increases. Sources of uncertainty include the user-controlled synchronization, photon shot noise inherent in the signal, and noise related to camera integration and readout (dark current, clock-induced charge, and gain and bias instability). Experiments to determine the relative magnitude of each source of uncertainty will be necessary, but it is expected that synchronization is currently the major source of error (Fig. 6-11).

6.2.2.2 Quartz

Two sequential, identical dose recoveries (Experiment A, B) were performed upon a previously measured, multigrain disc of Risø calibration quartz (Fig. 6-12). The given dose was 26.3 Gy, and growth curves were constructed with regeneration doses of 8.8, 17.5, 35, and 70 Gy with zero dose and recycled dose points (8.8 Gy). Test doses of 8.8 Gy were used. Measurements were made with a single aliquot regeneration protocol: the sample was preheated for 10 s at 260˚C (doses) and 240˚C (test doses), followed by blue LED stimulation (100 s, 125˚C). Image sequences at maximum gain were recorded during TL (1 s exposures) and OSL emission (10 s exposures excepting one 70 Gy measurement with 5 s exposures).

OSL signal was calculated based on the first image in each measurement sequence (for 10 s exposures) or summed over the first two images (for the 70 Gy sequence with 5 s exposures). Four ROI types were investigated: whole aliquot, single grain, 10x10 bins, and 5x5 bins. The whole aliquot region (Fig. 6-12a) was created by subtracting bias/dark current from a TL sequence (70 Gy) and then integrating the 110˚C signal. The resultant image was median filtered and thresholded to isolate the pixels corresponding to luminescent grains. Single grain ROI creation was similar, but it was based upon the OSL signal image (70 Gy; Fig. 6-12c). Six grain regions were isolated. For both ROI types, threshold values were determined by the user. Bins (Fig. 6-12f,g) were formed by summing pixels over square regions of the desired size; only bins fully contained within the 'whole aliquot' boundary region were accepted for equivalent dose determination. In total, 1109 5x5 bins and 254 10x10 bins were analyzed. All growth

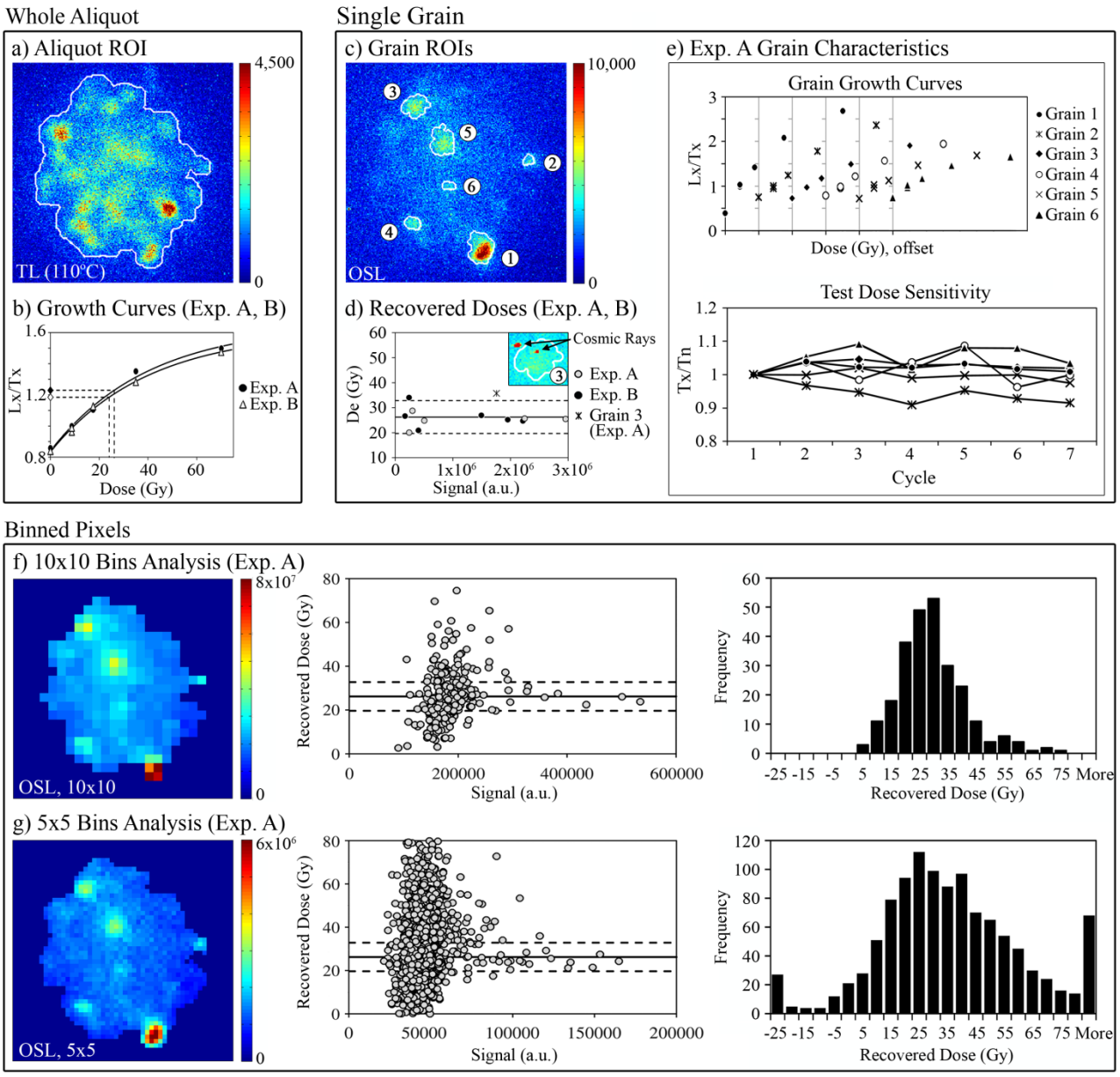


FIG. 6-12. Repeated dose recoveries (Exp. A, B) for Risø calibration quartz at various analysis levels. Whole Aliquot: a) TL (70.0 Gy) with white ROI boundary; b) Growth curves and recovered doses (Exp.A: black symbols, Exp. B: white symbols). Single Grain: c) OSL image (70.0 Gy) with ROI boundaries; d) Recovered dose vs. signal for Exp. A, B (given dose of 26.3 Gy: solid line, 25% boundaries: dashed lines); Inset view of natural OSL with cosmic rays that cause grain 3 overestimation. e) Test dose sensitivity changes and horizontally offset growth curves show individual grain behavior in Exp. A. Binned pixels: f) 10x10 bin analysis for Exp. A with OSL image of analyzed bins (70.0 Gy), recovered dose vs. signal (solid and dashed lines as before) and histograms of recovered dose; g) 5x5 bin analysis for Exp. A as f).

curves were fitted automatically with exponentially saturating curves, and equivalent doses were interpolated.

Both regenerated growth curves for the whole aliquot ROI are shown in Fig. 6-12b. Doses of 26.2 Gy and 24.1 Gy were recovered, 99.7% (Exp. A) and 91.7% (Exp. B) of the given doses, respectively. It should be noted that two cosmic rays present in the natural signal measurement during Exp. A (see Fig. 6-12d inset) have caused the recovered equivalent dose to be higher than for Exp. B, though closer to the given dose. This slight systematic underestimation at the whole aliquot analysis level may be due to the low signal to noise ratio of many included pixels. Similar fitting parameters were obtained for both growth curves. Previous aliquot measurements had resulted in sensitivity stability, and test doses fluctuated only by a few percent between cycles. The recycling ratios are consistent and small at 1.03, though this cannot be compared directly with the ten percent acceptance criterion often used as OSL background was not subtracted.

Single grain growth curve and test dose sensitivity comparisons show significant variation in grain behavior as expected (Fig. 6-12e). Recycling ratios and growth curve shapes are individual to each grain, as are sensitivity changes during the experiment. There seem to be no camera-related systematic offsets that are significant enough to affect data at this signal to noise ratio. Again, the effect of one cosmic ray is apparent in the obvious overestimate of equivalent dose for Grain 3 in Exp. A (Fig. 6-12d).

Smaller ROIs also produced good dose recovery when considered as aggregate populations. The usual statistical models used for OSL data analysis cannot be used here to calculate the recovered dose from these populations, as no error values have been produced for the measurements (due to the unknown noise characteristics of the equipment and the user-generated synchronization errors). Accuracy of dose recovery is significantly correlated with signal strength, however, as is evident with both bins and single grain ROIs, the effect disappears relatively quickly. If only the brightest 10% of 10x10 bins is considered, recovered doses range

from 0.83 to 1.65 times the given dose for one experiment, and over an even larger range for the other. The total range of the data depends on signal and noise levels. By contrast, analyzing frequencies of a larger population improves accuracy. Median values of the binned populations range from 0.97 to 1.18 times the given dose. Peaks in the frequency distribution may also be used for equivalent dose determination, but the precision and value will depend on the histogram bin width. It does not seem advisable at this time to suggest the use of mean values for equivalent doses, as noise spikes can adversely affect such values. This effect is apparent here in the standard deviation and positive skewness of the binned data in Exp. A (see particularly Fig. 6-12g) due to the recorded cosmic rays. Sources of uncertainty are as discussed in Section 6.1.3.

6.3 Further technique development

In order to improve system efficiency and accuracy, the author collaborated with Christian Bradley (Isis Instruments, Ltd., Oxford) to design a camera mount optimized for OSL detection. This mount has recently been manufactured (Fig. 6-13). It includes sample holders, a camera mount, optical stimulation (blue and green LED clusters) and heating capabilities, and the same optical system (lens and filters) as in the previous experiments. A triggering mechanism for the camera has also been integrated, in order to standardize and synchronize optical stimulation and imaging. Final electrical work is currently being carried out. It is expected that this mount will significantly improve the accuracy and sensitivity of the SR-OSL protocol, and further developmental work on this technique is planned.

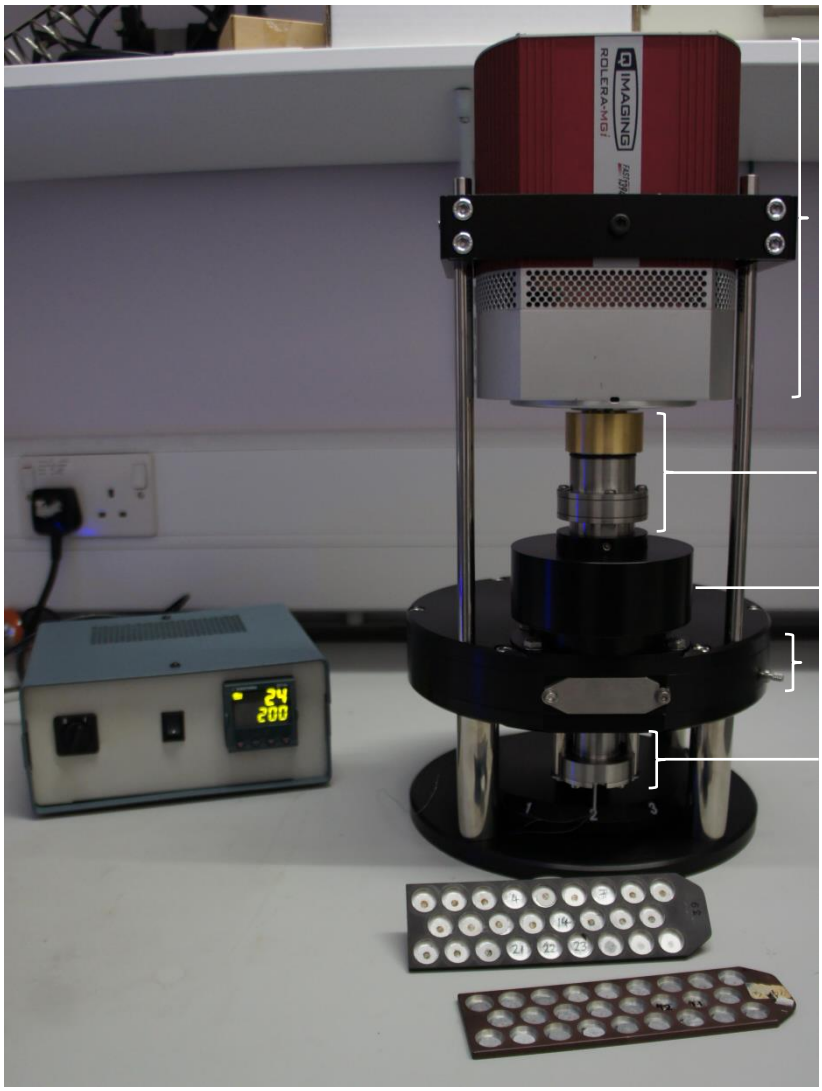


FIG. 6-13. Rolera MGi EMCCD camera, new mount, and thermal control box, with standard multigrain aliquots shown at bottom.

Chapter Seven

DISCUSSION

This chapter is organized into three major sections, which reflect the key themes in this project. In the first section, reliability of the OSL ages is considered in light of previous chronological work at each site, if available, and final site chronologies are proposed. The second section examines the success of various measures taken in this study to ensure the accuracy and precision of OSL ages, including the use of OSL quality control criteria, microsamples, Bayesian modeling, and SR-OSL. Finally, the third section integrates this study's age results with the available chronological data for the Aterian, and it discusses the implications of these ages for the study of modern *Homo sapiens*.

7.1 Chronologies by site

OSL age results are discussed for each site in turn. First, this study's OSL ages are compared to results from independent dating methods or prior OSL dating studies available for the site. All chronological evidence is then used to suggest the most likely archaeological framework for the site.

As standard practice, U-series ages are quoted with 2σ uncertainty, OSL ages with 1σ uncertainty, and calibrated radiocarbon dates as 95% probability ranges. Radiocarbon dates have been calibrated via OxCal (v4.1) using the IntCal09 calibration curve (Reimer et al., 2009). For purposes of comparison, all ages are given as thousands of years prior to A.D. 2012 (ka). Radiocarbon ages have also been rounded to the nearest hundred years for comparison with OSL and U-Series.

7.1.1 Taforalt

7.1.1.1 Previous chronological work

A primary goal of the recent excavations at Taforalt has been to create a comprehensive chronology for the cave sediments. Therefore OSL ages obtained during this project can be compared with radiocarbon dates in sediments younger than ~50 ka (Sectors 3 and 8) and U-series dates in older sediments (Sectors 1 and 6) (Clark-Balzan et al., 2012). A number of OSL ages obtained in a previous study are also available for comparison (Bouzouggar et al., 2007b).

Radiocarbon

Radiocarbon dates have been obtained for a large number of charcoal samples in the youngest cave sediments: the Upper Laminated Group (Sectors 3 and 8) and the Grey Series (Sector 8). Over 50 samples have been dated in Sector 8 alone (Fig. 7-1), and a Bayesian model was constructed for selected dates from this sector (S. Lee, pers. comm.). According to this model, Upper Laminated Group sediments were deposited mostly continuously, barring two hiatuses (~21-24 ka and ~15-17 ka). After a short period of Upper Laminated Group deposition, the Grey Series begins just after 15 ka with no appreciable hiatus. The whole Grey Series accumulated between 15 and 13 ka. This chronology is considered to be quite reliable, as it is based on a high number of samples and ages increase gradually with depth.

The agreement between OSL ages and radiocarbon dates is quite poor in the Grey Series. Two of four Grey Series samples yield OSL ages approximately 5,000 years too old; this is an age overestimate of more than 30%. One cause of age overestimation may be radioisotope

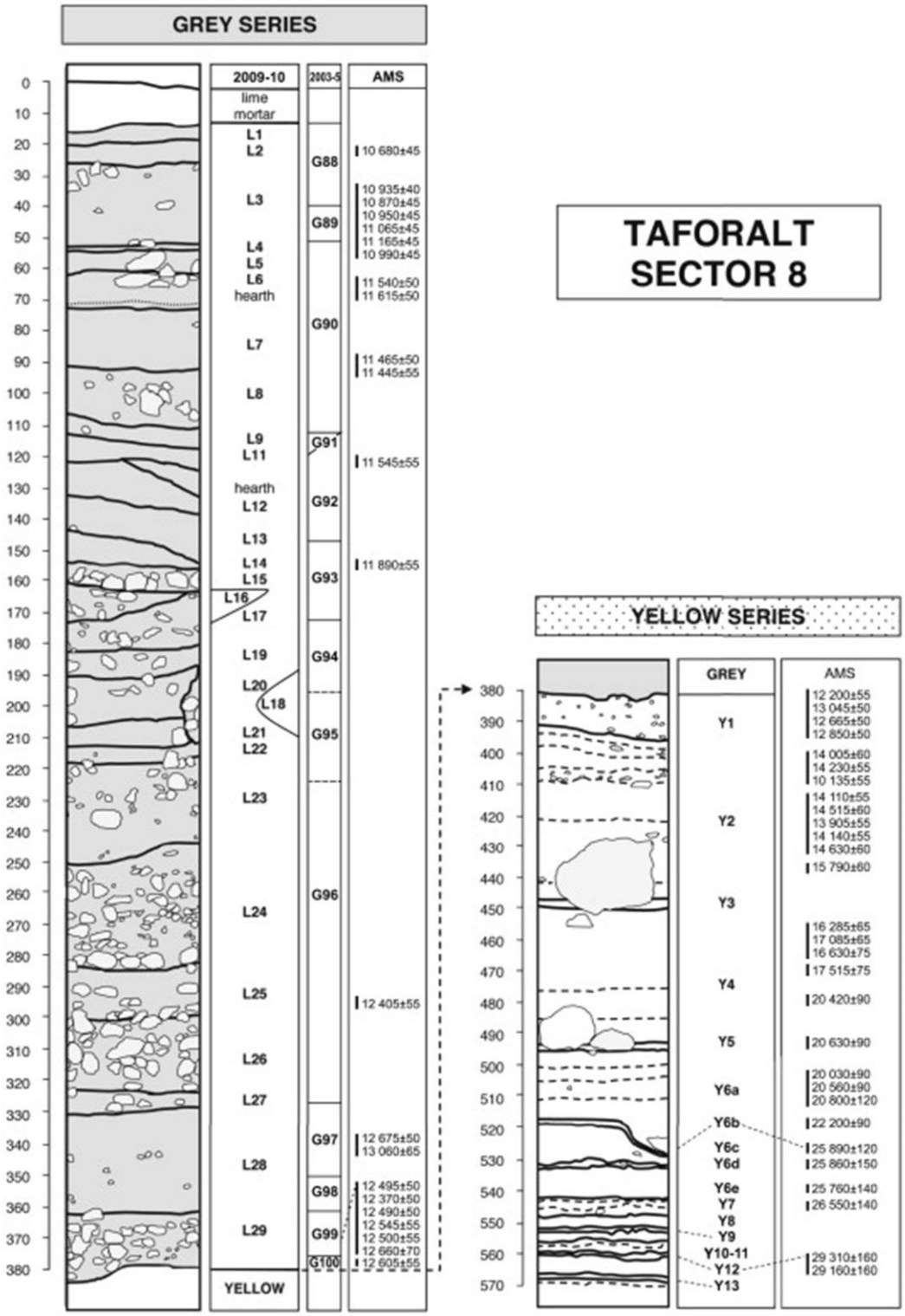


FIG. 7-1. Stratigraphy of Sector 8: Grey Series and Yellow Series (Upper Laminated Group) with AMS radiocarbon dates (BP, uncalibrated). Figure from (Barton et al., In Press: 6).

leaching, so that modern dose rate estimates are too low. Fresh wood ash commonly has between 5% and >10% potassium in the form of extremely soluble potassium salts (Etiégni and Campbell, 1991). The effect of ash diagenesis on OSL ages has been discussed for other cave sites (Mercier 1995; Schiegl et al. 1996; Weiner et al., 2002), and the unusual composition of the Grey Series and its young age is likely to exacerbate the effect. The range of measured equivalent doses is also unusually broad, which can be explained by the leaching hypothesis.

One simple scenario is as follows: if Grey Series sediments were deposited during an arid period, then subjected to increased water flow, most of the soluble potassium might have been lost in a nearly instantaneous event (relative to OSL timescales). Based on the radiocarbon dates and assuming a constant rate of deposition, burial ages for the Grey Series OSL samples TAF09-24 and TA09-25 can be calculated as 13.3 ka and 13.8 ka, respectively. It is possible for grains from TAF09-25 to have absorbed nearly 20 Gy, while those measured from TAF08-17 and TAF09-24 received only ~14-15 Gy, if the initial potassium concentration was 4.45% and 593 years elapsed before the potassium content decreased to modern day levels. This hypothesis, however, would require that the microsample TAF10-10 had been partially bleached during collection—otherwise the measured equivalent dose is much too low for its age and position in the sediment.

Excluding the unusual Grey Series, however, OSL ages are in fairly good agreement with nearby radiocarbon ages. The clearest stratigraphic link between the two techniques is a marker horizon, unit 'Y5,' which occurs ~1 m below the Upper Laminated/Grey Series Transition in Sector 8. Horizon Y5 can also be traced through Sector 3. Both radiocarbon and OSL samples were collected with specific reference to their stratigraphic relationship to this layer. Via radiocarbon dates on charcoal, this unit is dated to 24.4-25.0 ka (OxA-16274) in Sector 8, and bracketed by samples with ages 26.8-27.8 ka (OxA-26644) and 19.9-20.5 ka (OxA-26643) in Sector 3. OSL ages are generally consistent with this determination. The most accurate age seems to be microsample TAF10-14, which was collected 15 cm above Y5 in Sector 8 and yielded

an age of 24.4 ± 1.9 ka. Standard samples TAF08-14 and TAF08-15 should also be stratigraphically younger, but their ages (26.2 ± 2.1 ka and 29.7 ± 2.7 ka, respectively) are slightly too early. In Sector 3, Y5 is bracketed by standard samples TAF08-12 (above) and TAF08-11 (below), with calculated ages 23.0 ± 2.2 ka and 28.5 ± 2.8 ka, respectively. These ages are highly accurate. In contrast, microsamples bracketing Y5 in Sector 3 yield scattered and slightly younger ages.

More generally, the sedimentation schemes indicated by the two dating methods are also in agreement. The earliest unit dated by radiocarbon is Y12, for which an age of 33.4-34.6 ka (OxA-16277) has been obtained. The particular OSL samples that bracket this unit (TAF08-06 and TAF08-05) are reversed and younger than this age, but the OSL samples above and below this layer are in better agreement with the suggested radiocarbon age. Correlations for marker horizon Y5 have already been discussed. Higher in the section, the base of Y2 has been dated by OSL to 22.7 ± 1.90 ka (TAF08-16) and radiocarbon to 18.8-19.4 ka (OxA-16269). The Bayesian modeled Upper Laminated/Grey Series transition is also concordant (within 1σ error) between OSL and radiocarbon, though there are problems with OSL ages in the Grey Series as discussed previously.

U-series

U-series dates are available for the Calcareous Group deposits in Sectors 1 and 6 (Bouzouggar et al., 2007b; Clark-Balzan et al., 2012). Figures 7-2 and 7-3 display the sample locations and calculated ages for U-series ages published previously (Bouzouggar et al., 2007b; Clark-Balzan et al., 2012). The OSL samples in this study can only be related directly to the U-series sample locations published by Clark-Balzan et al. (2012). It should be noted that the OSL ages given in this document are not precisely the same as those published previously, though they are indistinguishable at 1σ. This difference is due to the different software used for equivalent dose and dose rate calculations. OSL ages obtained in Sector 1 are only comparable to the directly associated U-series dates when one discriminates between multigrain and single

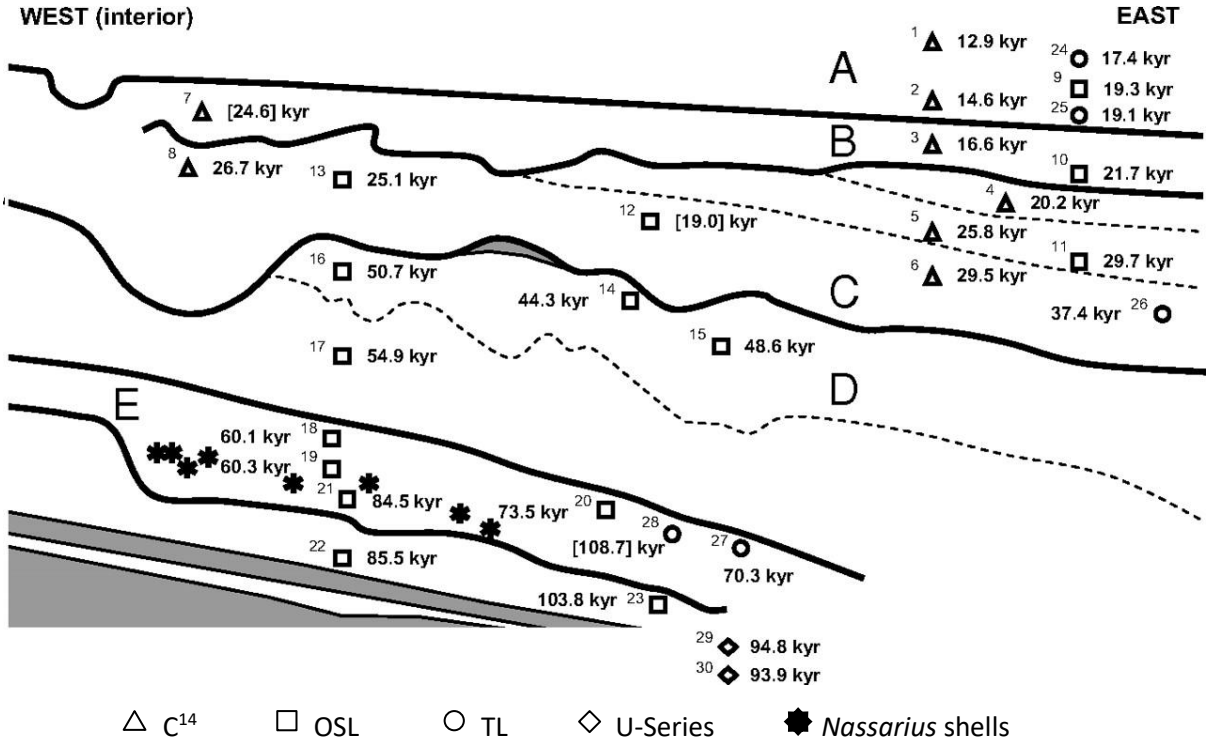


FIG. 7-2. Schematic of Taforalt stratigraphy and ages obtained by various dating methods: radiocarbon, OSL, TL, and U-Series. The positions of *Nassarius* shell beads are indicated. Stratigraphic groups are indicated with upper-case letters as follows: Grey Series (A), Upper Laminated Group (B,C), Pink Group (D), Lower Laminated Group (E), Calcareous Group (F). Figure from (Bouzouggar et al., 2007b: 9965).

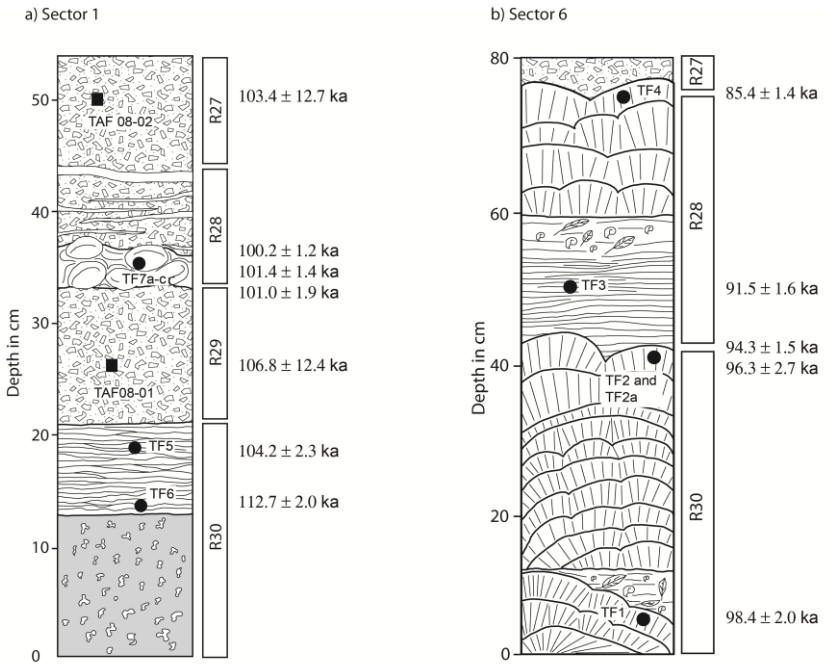


FIG. 7-3. Section drawings for Sectors 1 and 6 with U-series (●) and OSL ages (▄) indicated, redrawn from Clark-Balzan et al. (2012: 60). The single grain age is given for TAF08-02 and the multigrain age for TAF08-01; these ages are slightly different from those reported previously (see text for discussion).

grain ages. There are significant differences between the ages obtained via each analysis technique, and it has already been suggested that TAF08-02's single grain age (to circumvent super-saturation) and TAF08-01's multigrain age (dose recovery issues) are likely to be more reliable. The U-seriesages obtained previously for the basal flowstone in Sector 6 (Fig. 7-2), 94.8 ± 0.9 ka and 93.9 ± 0.8 ka (Bouzouggar et al., 2007b), are in good agreement with the recently published ages.

Based on these ages, it seems that several OSL ages in Sector 2 may underestimate the burial age of the sediment. The stratigraphy appears very similar in Sectors 1 and 2, so there is no reason to expect significant discrepancies in age. Yet the earliest Calcareous Group ages obtained in Sector 1 are ~100 ka (both OSL and U-series), while three samples in Sector 2 suggest that these sediments were deposited between ~66 ka and ~76 ka. The ~90 ka age obtained for TAF09-27 is more congruent with the Sector 1 ages. Due to the U-series data and the lack of gamma spectrometry data for the microsamples (see Section 7.2.2 for further discussion), it is felt that the older chronology is likely to be more accurate. This comprises samples TAF09-26 and -27 in Sector 2 and TAF08-01 and -02 in Sector 1.

Previous OSL analysis

Agreement between the current study and previous OSL dating work is not sufficient to suggest that dates are accurate, as the same assumptions and essentially the same methods of calculation have been used (Fig. 7-2). This is most obvious in the Grey Series age overestimation, which is shared by the current study and OSL/TL ages published by Bouzouggar et al. (2007b). However, there are some points of interest. In Sector 8, samples TAF08-16 (22.7 ± 1.9 ka) and TAF03-L13 (21.7 ± 1.3 ka) were collected at approximately the same stratigraphic level, and their ages agree within 1σ uncertainty. Below this, OSL and TL ages obtained in the previous study seem to overestimate sediment age by more than 5,000 years. Measured equivalent doses and dose rates for these samples are significantly different between the two studies, even though methodology for both equivalent dose estimation and dose rate calculation are similar. OSL and

TL ages for the Pink through Calcareous Groups also tend to be older in the previous work, though they agree with the Sector 1 and 2 ages from this study that are considered to be more reliable.

7.1.1.2 Final chronology

The following archaeological chronology incorporates lithic interpretations by R.N.E. Barton and J. Hogue. MSA populations occupy Taforalt by ~100 ka or soon thereafter, according to U-Series and OSL ages for the Calcareous Group. The earliest Aterian tools and *Nassarius* shell beads occur near the Lower Laminated/Calcareous Group transition, between approximately 80 and 90 ka and probably closer to the latter age. The youngest Aterian is represented by a bifacially knapped lithic, sidescraper, and Levallois debitage found in the Laminated Hearth deposits of Sector 9. The OSL age for this deposit gave 37.6 ±3.4 ka, which accords well with the stratigraphy. There is currently no data on potential occupation hiatuses during the Aterian phase.

Following the Aterian, the cave seems to have been unoccupied until the non-Levallois MSA flake industry first appears in unit Y11. It is difficult to give a precise date for the earliest appearance of this industry. Y11 should be bracketed by the reversed OSL ages TAF08-05 and TAF08-06, which give 30.8 ± 2.6 ka and 24.0 ± 2.0 ka, respectively. These ages are Bayesian modeled to ~ 28 ka. It is also bracketed by radiocarbon dates on units Y12 (OxA-16277: 33.4-34.6 ka) and Y7 (OxA-16276: 31.4-31.0 ka). This highest stratigraphic appearance of this industry is the top of unit Y6, which is essentially indistinguishable from the above marker horizon Y5 according to radiocarbon dates. Therefore, this industry probably appeared around 33 ka or soon thereafter and continued until ~24-25 ka.

A hiatus separates the latest MSA and earliest Iberomaurusian occupation. The earliest Iberomaurusian artifacts are found in the top of unit Y4, and are therefore stratigraphically younger than OSL samples TAF08-14 and TAF08-15. These samples produced ages that are several thousand years too old for their stratigraphic position, but Bayesian model results

suggest more likely ages of 25.6 ± 1.5 ka and 25.1 ± 1.3 ka. According to excavation and radiocarbon data, the earliest Iberomaurusian occupation occurs directly after a hiatus in the depositional record of approximately 3,000 years. By radiocarbon, the earliest extant Iberomaurusian industry is dated to 20.5–21.4 ka (OxA-16273). Because of the depositional hiatus, though, it is possible that occupation began several centuries earlier. Typological shifts in Iberomaurusian lithics occur around 17 ka and again at the Upper Laminated/Grey Transition ~15 ka. The youngest remaining Grey Series sediment and therefore evidence of Iberomaurusian occupation is approximately 13 ka. It is probable that the top of the Grey Series was removed by the French military in the mid-20th century, based on burn marks on the cave wall and the presence of a lime mortar floor capping the extant Grey Series. Therefore the youngest available date does not record the last occupation of the cave.

7.1.2 Dar es-Soltan I

The only independent age information comprises two infinite radiocarbon dates on samples from the upper and lower Aterian levels (Berger et al., 1965), which are clearly not useful for comparison to the OSL ages obtained in this project. There are, however, several OSL studies on sites in the Rabat and Casablanca areas with which these results can be compared.

This study dated the aeolianite containing Dar es-Soltan I to 147.8 ± 1 ka, which is younger than the previously published age, 209.2 ± 29.5 ka (Barton et al., 2009). This difference in age is due to the slightly different methodology used in this project, namely an increase in calculated dose rate (i.e. higher alpha and cosmic ray doses) and the use of more stringent rejection criteria for equivalent dose calculation (only three of 18 aliquots accepted). The altitude of this aeolianite has been surveyed at 13.52 m above the current mean beach level (exposed at low tide and covered at high tide), which is thought to be a reasonable approximation for mean sea level (Barton et al., 2009). Both age and altitude are in accordance with the regional beach ridge chronology. A similar age of 163 ± 33 ka was obtained by Rhodes et al. (2006) for a lithified dune deposit of the Bir Feghloul Member near Casablanca, about 100

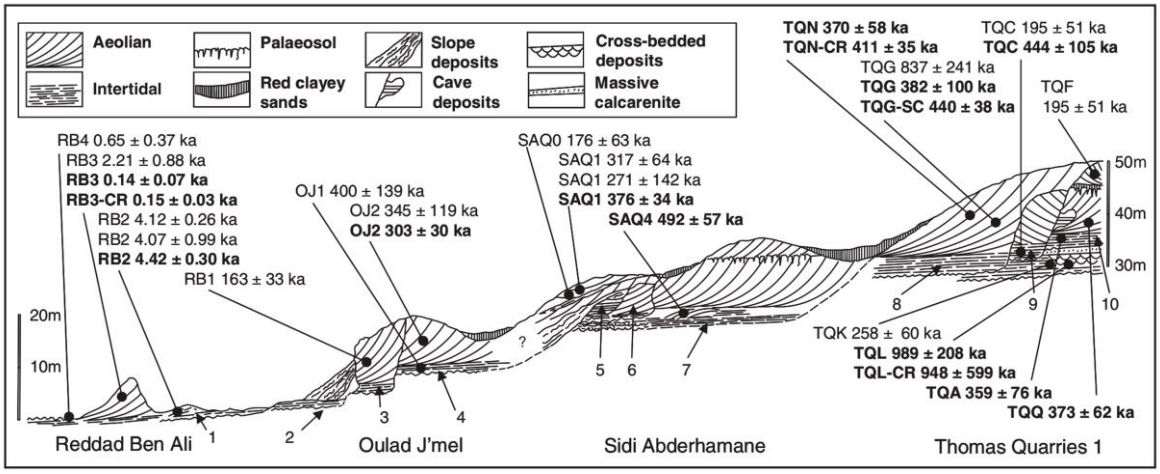


FIG. 7-4. Beach ridge stratigraphy in the Casablanca area and OSL ages. This study suggests that the Dar es-Soltan I aeolianite can be identified with the lithified dune deposit (Bir Feghloul Member, Oulad J'mel Group) dated to 163 ± 33 ka (Rhodes et al., 2006: 2570).

km south of Rabat (Fig 7-4). The base of this aeolianite lies upon a foreshore sand at ~7-8 m asl, and rises to a height of ~15 m asl (Texier et al., 2002). It is reasonable to suppose that these aeolianites are related to the same deposition and lithification events.

Turning to the interior of the cave, Group 1 sediments are likely to have been deposited during MIS 5.5. This attribution is based on a detailed analysis of local beach ridge topography, consideration of regional uplift rates, and sea level data (Barton et al., 2009). The basal, well-bedded shell sands at Dar es-Soltan I have been firmly identified as intertidal deposits (Schwenninger et al., 2010). In this project, these sands are represented by samples SOL1-05-01/DES08-21, SOL1-05-17/DES08-22, and DES08-24, collected from Units 1.4, 1.3, and 1.2, respectively. The resulting multigrain ages range from 96.6 ± 17.7 ka (DES-08-24) to 135.4 ± 20.5 ka (SOL1-05-01), while two single grain analyses on replicate samples SOL1-05-01 and DES08-21 yielded 112.1 ± 17.4 ka and 88.0 ± 12.6 ka, respectively. Ages from the rest of Group 1 support the hypothesis of rapid sedimentary deposition at around this time, as no overall age-depth

trend is apparent. Though the obtained ages are rather widely distributed, they certainly do not exclude the possibility of this group being associated with MIS 5.5. Given the suggested date for dune deposition (~150 ka), lithification and karstification prior to ~125 ka is quite possible (Barton et al., 2009). Schwenninger et al. (2010) find that similar basal sands are present in the nearby caves Dar es-Soltan II, Contrebandiers, and El Mnasra, and they probably also appear at the base of the deposits in El Harhoura 2 (Jacobs et al., 2012). OSL ages from these sites also support an MIS 5.5 attribution.

Younger sediments are more problematic. Based on a careful analysis of the results, it seems that calculated OSL ages for Dar es-Soltan I may underestimate the true burial age for samples obtained from 3 to 7 m depth (Group 4 through Group 2). To recap, elemental biplots indicated an anomalous K/Th relationship for samples with thorium concentrations >3.7 ppm (see Section 5.2.3.1). Calculated dose rates also increase sharply at ~ 7 m depth, due primarily to these high elemental concentrations, while measured equivalent doses increase smoothly through this level. This offset suggests that the current elemental concentrations may be higher than average concentrations during the samples' burial history. Therefore some of the ages may be too young. The source of such a radioisotope input is unknown, but fertilizer is one possibility. Indeed, Jacobs et al. (2011) note that artificial irrigation in the area above Contrebandiers has probably increased present day water content of the cave sediments; unfortunately, they do not publish their elemental concentration data. Disequilibrium measurements and isotopic analysis of Dar es-Soltan I sediments should allow this theory to be proved or disproved (Martínez-Aguirre et al., 1994; Zielinski et al., 1997; Martin and McCulloch, 1999). Alternately, radioisotopes may be enriched by post-depositional clay translocation (Scarciglia et al. 2009), which could be investigated with a micromorphological study. If either hypothesis is correct, such anomalous elemental concentrations may also affect other caves in the region.

By Group 5, comprising midden material and fine sand, the elemental concentrations follow standard biplot trends again. The base of Group 5 (5.1) seems to have been deposited around 29.6 ± 3.1 ka (SOL1-05-14), followed by a significant depositional hiatus. Subgroup 5.2 was then rapidly deposited, with samples yielding OSL ages of 7.7 ± 0.8 ka (SOL1-05-15) and 6.2 ± 0.9 ka (SOL1-05-16). Schwenninger et al. (2010) identify the base of Subgroup 5.1 with MIS 3, and correlate it with Layer 3b2 at Dar es-Soltan II (31.1 ± 2.1 ka) but cannot trace this unit to either Contrebandiers or El Mnasra. Subgroup 5.2 should have been deposited in MIS 1, but no similar unit is evident in the area except possibly Layers 1-3 in El Mnasra. The ages found for these units are therefore difficult to support with other data, but there is no reason to believe they are inaccurate.

Dar es-Soltan I was occupied both more frequently and earlier than suggested in Ruhlmann's excavation stratigraphy. Though a thorough excavation will be necessary to fully reevaluate the archaeological record of the cave, the presence of charcoal and lithics from subunit 1.7 indicate early human occupation. SOL-05-02, a sample obtained from the same subunit, has an OSL age of 103.4 ± 11.8 ka, but based on surrounding ages and the sedimentological analysis, it seems likely that this occupation is probably older. In fact, this unit is likely to be around 125 ka, as it occurs immediately above the basal, intertidal sands.

All known Aterian levels unfortunately occur within Groups 2 through 4, for which some of the calculated dose rates may be inaccurate. The *Atérien inférieur*, which is found in Ruhlmann's Niveau I and subunits 2.2-2.6 in the current scheme, is associated with samples SOL-05-06 and DES08-33. Both samples were collected from subunit 2.6, and yielded ages of 115.7 ± 11.7 ka and 71.4 ± 7.8 ka, respectively. Considering all factors, it is likely that the older age is more accurate. The younger age (DES08-33) conflicts with the stratigraphy and overall chronological framework, while the older age, in fact, is the only sample from Groups 2 through 4 that has thorium values <3.7 ppm. Conversely, an age of 115.7 ± 11.7 ka is significantly older than the next five oldest dates in Groups 2 and 3, which all overlap ~100 ka. Therefore, a strict

interpretation of the evidence confirms that the earliest Aterian is at least 100,000 years old, and possibly significantly older.

The *Atérien supérieur* and *Mousterien decadent* both occur within Group 4. The *Atérien supérieur* (Ruhlmann's C2), is correlated with subunit 4.4 and bracketed by OSL samples SOL1-05-12 below and SOL1-05-13 above. Therefore, this level should be between 51.7 ± 5.4 ka and 58.3 ± 5.4 ka. However, both samples have relatively high potassium and thorium levels, so the calculated ages may be too young. If so, the latest Aterian could be older than 50 ka. The *Mousterien decadent* (C1) occurs at the top of Group 4 (above SOL1-05-13) and below the lowest OSL sample in Group 5: SOL-05-14, with a calculated age of 29.6 ± 3.1 ka. Therefore, it may date from any time between 30 and 50 ka.

7.1.3 Rhafas

Dating of Rhafas Cave has focused primarily on the Mousterian and Aterian levels, which are too early to account for the age of last burial of the Rhafas femur fragment (Mercier et al., 2007; Dörschner et al., 2012). Unit I includes Neolithic remains, for which one radiocarbon date has been obtained: 5.8-6.3 ka (GIF-6185). Mercier et al. (2007) give no information about this sample, therefore it is difficult to evaluate its reliability. However, a significantly older date would be unexpected in light of the presence of pottery at the site (Linstädter, 2008).

The burial age obtained for the Rhafas femur, ~ 8.5 ka, does not coincide with any of the major occupation periods of the cave as they are now understood. As noted, however, the gamma and beta dose rate uncertainties are high. If the bone had accumulated slightly more than 7 ppm of uranium by the time it was buried or soon thereafter, the OSL age would be in agreement with the Neolithic radiocarbon date. It seems most likely that the last burial of the bone fragment occurred either during the Neolithic period, or that the bone was filled with sediment of this age during excavation. The age of the bone itself is still an open question, and both morphological analysis and further dating studies are required.

7.1.4 Chaperon Rouge II

The equivalent dose analysis conducted during this study has already been compared to Rhodes' (1990) OSL dating of the sample. This date cannot be further interpreted with any site specific information, as Chaperon Rouge II has not been studied since. The likelihood of the date with regards to the Aterian as a whole, though, will be discussed in the next section.

7.2 Improving the accuracy and precision of OSL ages

It should be apparent from the introductory chapters that assessing the reliability of obtained ages is a vital step in chronological analysis. Without this step, time, energy, and money can be wasted either by re-applying an inappropriate dating methodology or by basing hypotheses on the mistaken results. In this section, several methods for improving the accuracy and precision of OSL ages will be evaluated.

7.2.1 Intrinsic OSL quality control

A number of quality control procedures are routinely applied to the calculation of equivalent dose in OSL dating studies, including dose recovery and preheat plateau experiments, the application of SAR rejection criteria, and examination of values such as overdispersion and saturation. Nevertheless, even a sample that passes these tests may not yield a laboratory-measured equivalent dose that is equal to the palaeodose received during burial. The simplest example is that of supersaturation. Though supersaturation can be detected in equivalent dose measurements of natural sediments, a sample with numerous supersaturating grains can pass a dose recovery experiment which is intended to test the suitability of the SAR protocol for that sample. Additionally, these tests do not address the accuracy of the calculated dose rates, therefore the accuracy of the final ages. Each of these issues has been demonstrated in these research results.

Both the Grey Series of Taforalt and the dates obtained at Dar es-Soltan I demonstrate the difficulty of assessing OSL age accuracy in complex environments via intrinsic luminescence criteria. As noted in the previous section, numerous radiocarbon results indicate that calculated

OSL ages severely overestimate the age of the Grey Series. It has been suggested that this is due to isotope mobility in the sediment. Based on the luminescence characteristics, including accurate dose recovery, minimal overdispersion, and high sensitivity, though, the Grey Series ages should have been among the most reliable at Taforalt. Without radiocarbon dates, these ages would not have been questioned or investigated further. In contrast, stratigraphic analysis of the numerous OSL ages obtained at Dar es-Soltan I indicate significant problems with OSL dating samples. Though rejection criteria have been applied and dose recovery experiments performed, luminescence characteristics offer no suggestions as to which ages are more accurate. Like the Grey Series, some of these samples may be subject to radioisotope mobility issues, either via recent deposition or leaching, as suggested by the unusual K-Th concentration biplots. These cases underscore a significant obstacle for OSL age accuracy, namely the difficulty of accurately assessing the average dose rate received by mineral grains over the burial history of the samples.

Dar es-Soltan I results also demonstrate the significant differences in OSL ages possible due to age model choice or equivalent dose analysis type. Current analytical methods offer no conclusive evidence for which age model is more appropriate in a particular environment. Nor do standard error calculations incorporate the potential error introduced by application of the wrong age model. The inclusion of such alternatives would dramatically increase the error ranges of OSL ages, likely to an unrealistic level. Nevertheless, the effect of age model choice should always be considered carefully, particularly when a single component has been extracted from a complex equivalent dose distribution. In most environments, use of the central age model is likely to be the most parsimonious choice for age calculation. Interpretation of ages due to stratigraphic information should be conducted separately and explicitly, via techniques such as Bayesian modeling (see below). Otherwise, it is likely that with the multitude and spread of data collected during an OSL study, one can find a subset that corresponds to the *desired* age.

OSL age interpretation can also be prone to circularity when investigators must choose between using multigrain and single grain equivalent doses. It should be evident from the results of this study that equivalent doses obtained via these two types of analysis can be variable. This is not uncommon (S.Burrough, R. Bailey, pers. comm.), but as it is difficult to explain, these results are usually not published. External data is often used to choose the most appropriate value (Olley et al., 1999; Prescott et al., 2007), but this can be problematic. In the case of Dar es-Soltan I, the sheer volume and spread of data would ensure that a stratigraphically coherent age-depth model could be produced from the OSL measurements. Nevertheless, the site information that is available does not support this winnowing. In a simpler case, this same dilemma occurs with the dating for Sector 1 of Taforalt. Having examined the site, noted the stratigraphic reversal of the OSL ages, and compared the OSL and adjacent U-series ages, there are valid OSL reasons for calculating the OSL ages based on the single grain equivalent dose for TAF08-02 and multigrain for TAF08-01 (see Section 7.1.1.1). Without the U-series information, however, the OSL ages might have been interpreted differently.

7.2.2 Microsamples

Microsample collection was tested at Taforalt as a means of obtaining high precision OSL chronologies via sample clustering and the bracketing of visible sedimentary boundaries. Practical considerations are important, as this type of sample is more difficult to collect and analyze due to the small sample volume. Additionally, such samples require slightly altered age calculation procedures, including the use of VSAs for equivalent dose measurement and planar boundary modeling for gamma dose rate calculations. Such non-standard techniques must be evaluated for accuracy. Each of these issues will be discussed below.

Obtaining and working with microsamples of the type used in this study (small diameter cylinders) was more difficult than the same processes with standard samples. The most common problem during sampling was that of encountering rock fragments in the sediment.

While fragments up to several centimeters in diameter may be contained within a standard sample, fine to medium gravels were large enough to adversely effect microsample collection. Additionally, friction between the sediment and sample collection tubes (particularly for those 1 cm in diameter) could be problematic during collection. Sample preparation, i.e. removal of bleached sediment from the sample ends, was also time-consuming. Due to the small diameter of the sample containers, it was more difficult to successfully remove all bleached material.

The use of VSAs for equivalent dose measurements prohibits interpretation of the resulting equivalent dose distribution as though it were measured from single grains. The measurement of more than one grain at a time creates 'phantom' dose components due to grain averaging effects, therefore the finite mixture model cannot be used (Arnold and Roberts, 2009; Arnold et al., 2012). In addition, beta source calibration in this study has suggested that a small correction (on the order of a few percent) to the Risø dose rate is necessary when VSAs are measured (Section 4.2.1.2). This is likely due to the differing geometry of the sample grains in the single grain disc. It may be that the required calibration factor will depend on the grain size used to create the VSAs, but this has not been tested as a single grain size was used for all VSA analysis during this project. With both of these caveats, however, VSAs are highly efficient for obtaining a large amount of equivalent dose information from a small sample volume. There is no reason to believe that the central age equivalent dose measured is systematically offset by this procedure.

As noted in the results, it was necessary for gamma dose rates to be calculated from elemental concentrations for some microsample locations. These calculations included planar variation approximations for those microsamples that were collected within several centimeters of a sedimentary boundary. Gamma dose rates were calculated from ICP for samples TAF10-14, TAF10-10, and all samples in Sector 2 excluding TAF09-26, -27, and -38, while planar variation models were created for samples TAF09-35/36, TAF09-39/40, and TAF10-18. Due to the complexity of the site, evidence for the success of this strategy is mixed. Both Sector 2

microsample pairs that bracket Group transitions are in good stratigraphic order, and the ages obtained suggest believable hiatuses of perhaps several thousand years. When compared to more sophisticated MCNP models, the planar variation approximations did not produce identical results but were much more similar than gamma dose rates calculated for homogeneous sediment. However, there may be a systematic underestimation of age when Sector 2 microsample ages are compared to standard OSL samples and U-series dates from Sector 1. This is likely to be due to overestimation of the gamma dose rate.

Overall, microsampling appears to be most useful in archaeologically dense regions for which high precision ages are required with as little sampling damage as possible. It should be noted that the precision of all microsample ages is as good as or better than those from standard samples. This may be due to the fact that microsamples collect and average less sediment vertically, therefore they are more temporally precise. Two important modifications should be considered, however, for future use of this technique. First, use of sampling containers such as Kubiena tins may be more effective. These would be used to collect a block of sediment, which could then be subsampled in a safe-light environment. Second, synthetic dosimeters, such as aluminum oxide pellets, should be used to obtain high precision records of gamma dose rates via on-site measurement (Aznar et al., 2003; Richter et al., 2010). Such pellets are ideal, as the gamma dose rate can be measured precisely at the sample location. The effect of the previously-excavated sediment would still have to be approximated.

7.2.3 Bayesian modeling

Bayesian modeling is a useful technique for interpreting OSL dates, which tend to have relatively large errors of 5-10%. For studies that seek to link, for example, human adaptation and climate change, uncertainties at this level can prohibit useful site comparisons. If enough OSL samples are collected so that their errors overlap, the incorporation of stratigraphic information into a Bayesian model will increase the precision of these dates. Perhaps even more

importantly, Bayesian modeling allows the incorporation of multiple kinds of information and makes explicit the accompanying assumptions.

Two Bayesian models were created for this project, one each for the sites Taforalt and Dar es-Soltan I. Both models incorporated parameterization of OSL age information, so that independent and dependent variables could be allocated appropriately. Due to differing site characteristics and OSL results, of course, the models were dissimilar.

Taforalt is a complex site, with each sample being related to other sampling locations via a hierarchy of stratigraphic associations. A number of samples also had multiple possible ages due to various scales of equivalent dose analysis. Analyzing these data via a Bayesian model yielded two key benefits. First, all age information and assumptions regarding the reliability of certain parameters were explicitly incorporated into the model via priors. This is preferable to statistically removing components from equivalent dose data in order to get high precision but potentially inaccurate OSL ages. Second, the model was used to extract posterior likelihoods for the age of particular archaeological and geographic events. Horizon 'Y5' was one such event modeled in this way, and the suggested age was within 1 σ uncertainty of the best radiocarbon estimate.

Conversely, Bayesian modeling of Dar es-Soltan I was made difficult by the numerous age reversals. Only a general phase model, rather than a more restrictive sequential model, could be run. Moreover, if a high number of the input ages are inaccurate, the model as a whole will be of little use. However, the final model is at least a statistically simplified framework for investigating a large and complicated chronological database.

7.2.4 SR-OSL

The ultimate goal of SR-OSL is to measure the equivalent dose of specific regions within a sample so that these can be integrated with models or measurements of the radiation field specific to that grain (Nathan et al., 2003). It seems likely that this approach could significantly increase the accuracy and precision of final OSL ages for sediment and other geological

materials. This project has focused on the necessary first step for a functional SR-OSL quartz dating technique, namely, to identify and test imaging equipment for purposes of equivalent dose calculation.

The results presented in Chapter 6 indicate that UV-sensitive (back-thinned, back-illuminated) EMCCD cameras are a viable option for UV SR-OSL measurements of quartz and feldspar. Theoretical considerations and discussions with numerous experts suggest that EMCCDs are more likely to image OSL emissions from quartz grains than a standard CCD. Qualitative experiments conducted with a Rolera-MGi EMCCD demonstrated that a significant number of quartz grains emit detectable OSL emissions when natural, unbleached sediment is stimulated. Though no experiments were conducted solely on feldspar, feldspar grains included in several images emit UV signals at least several orders of magnitude stronger than those emitted by quartz. Individual grain boundaries are apparent, though emitting grains are more discrete for chips of consolidated material than for multigrain aliquot measurements. This is due to the reflective surface of the aluminum discs used to measure standard quartz extracts. Grains can be tracked between measurement cycles, so that emissions can be compared after various treatments.

Quantitative experiments show that reasonably accurate equivalent dose data can be obtained from EMCCD-recorded image sequences. Laboratory doses given to quartz aliquots were recovered within 10%, and multiple irradiation and measurement cycles for aluminum oxide grains show the expected linear increase of signal with dose and good measurement repeatability. Useable equivalent dose information could be extracted via ROI selection of various types, including sample specific single grain masks and simple pixel bins (5x5 or 10x10). The accuracy of these experiments was dependent primarily upon instrument control and image processing techniques that accounted for dark noise, bias drift, and non-uniformities across the sensor. It is likely that most of the measurement error was due to user initiation of the imaging and stimulation steps. This lack of consistent synchronization between EMCCD operation and

stimulation activation will affect the decay curve shapes extracted from image sequences, and therefore the equivalent dose.

Much further development is required. With regards to the current Oxford equipment, the work is currently proceeding on three fronts: optimization of light collection efficiency, synchronization of imaging and stimulation, and characterization of system uncertainty and stability. More sophisticated data processing techniques are also being developed, including automated single grain ROI creation and equivalent dose estimation. Without too much further development, EMCCDs could be (and are starting to be) developed into a faster and simpler single grain measurement system. The true potential of SR-OSL, though, relies on future integration of SR-OSL results with beta microdosimetry measurements. Only then can physical measurements be made that will validate (or invalidate) currently hypothetical age models.

7.3 A new chronology for the Aterian

7.3.1 Review of recent chronological publications

Several publications have been released since the inception of this project. A total of nine Aterian or Middle Palaeolithic sites have now been dated via isotopic or trapped charge methods. These sites can be split into three geographical regions: the Atlantic Coast (near Rabat), the Strait of Gibraltar, and the Atlas Mountains (northeastern Morocco). Results from each region are discussed in turn. The site of Chaperon Rouge II will be excluded from this discussion, as this study has shown that the published OSL ages are likely to be inaccurate but a revised age could not be determined.

7.3.1.1 Atlantic Coast

Including this study, OSL ages have been obtained for five Aterian or Middle Palaeolithic sites on the Atlantic Coast: Dar es-Soltan I and II, El Harhoura II, Contrebandiers, and El Mnasra (Fig. 7-5). The earliest extant sediment in this series of caves is attributable to the marine high-stand at MIS 5.5, ~125 ka (Schwenninger et al., 2010; Jacobs et al., 2012), and the earliest traces of human occupation occur within or immediately above these sands. These early deposits have

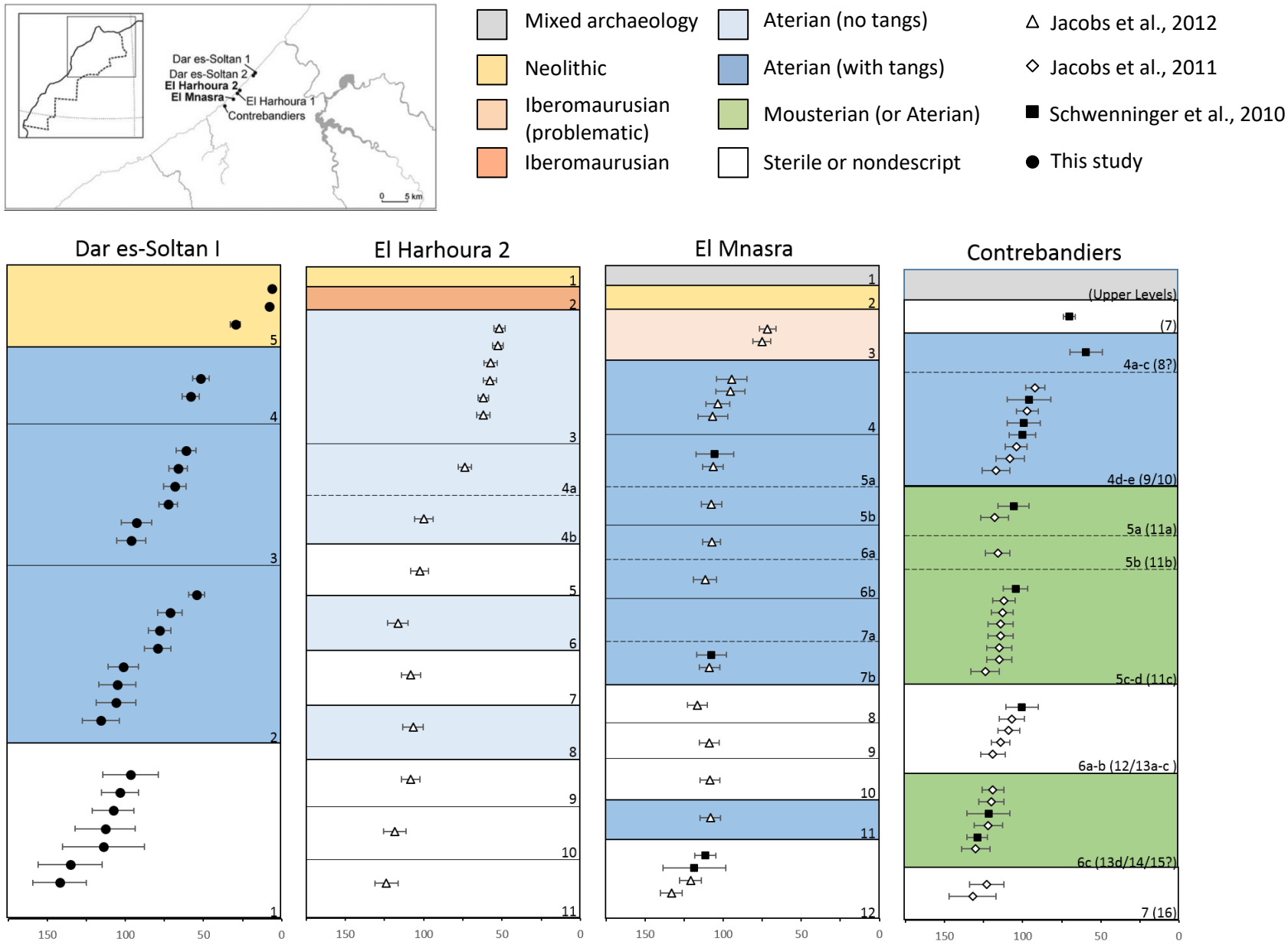


FIG. 7-5. Schematic stratigraphies of OSL-dated MSA cave sites on the Atlantic Coast of Morocco: Archaeological attribution and OSL ages (in rank order within each sedimentological group/layer) are shown. The map in the upper left hand corner is from Jacobs et al., 2012: 378, and the correlations between the Roche and Nespoulet stratigraphies at Contrebandiers are given in Jacobs et al., 2011 and Dibble et al., 2012. See text for discussion of Aterian chronology.

sparse lithic remains, which are typically considered generalized MSA (Schwenninger et al. 2010, Nespoulet et al., 2008b). At Contrebandiers, Jacobs et al. (2012) have attributed this early occupation to a 'Moroccan Mousterian.' The implications of this will be discussed further below.

Human fossils have been found within the top of the basal beach sand at Dar es-Soltan II, dated to 121.7 ± 8.2 ka (Schwenninger et al., 2010), and more recently, a child's skull and partial skeletal remains were excavated from 'Mousterian' levels at Contrebandiers (Balter, 2011). Balter (2011) states that the Contrebandiers fossil is 108,000 years old, but no stratigraphic information is given and this age does not match any of the published ages for the Moroccan Mousterian at this site (Jacobs et al., 2011).

The earliest Aterian at each of these sites is older than 100 ka and may be as old as ~120 ka (Fig. 7-5). The Aterian record for Dar es-Soltan II has not been well published, therefore this site is excluded from the following discussion. The evidence for Dar es-Soltan I has already been described, and a parsimonious age of >100 ka assigned to the first Aterian. The earliest Aterian at El Mnasra was thought to occur in Layer 7 (Nespoulet et al., 2008b), which has been dated to 107.6 ± 9.6 ka (ELM-05-03) by Schwenninger et al. (2010) and 108.8 ± 6.6 ka (EM08-7) by Jacobs et al. (2012). It seems that further excavations have identified a lower Aterian level (Level 11). However, this level is indistinguishable in age from Layer 7: 108.3 ± 6.6 ka (EM08-3) (Jacobs et al., 2012). Similarly, Level 8 at El Harhoura II has an age of 106.7 ± 6.6 ka (EH08-4) (Jacobs et al., 2012). The identification of the archaeology as specifically Aterian is not completely clear, as the authors note 'No stemmed artefacts associated with the Aterian have been found in these assemblages, but all other attributes of the Aterian are represented' (379).

Identification of the earliest Aterian at Contrebandiers is contentious. Schwenninger et al. (2010) identify the earliest Aterian industry at Contrebandiers within Level 14, which overlies the basal sandy layers 15 and 16. This level is bracketed by two OSL samples, which yield ages of 121.8 ± 13.8 ka (CON-05-02) and 129.0 ± 6.6 ka (CON-05-01). Conversely, Jacobs et al. (2011) identify this earliest archaeology as a Moroccan Mousterian, but they obtain similar ages for

these deposits, between 116.3 ± 3.0 ka (SC17) and 127.7 ± 6.3 ka (SC11). Five samples have been collected from the overlying Aterian in the central excavation section. Four of these had OSL ages between 103 ± 6 ka (SC 21) and 108 ± 9 ka (SC8), and one was slightly older at 117 ± 9 ka (SC7). Jacobs et al. (2011) correlated three of these samples (SC20, SC8, and SC7) with Schwenninger et al.'s (2010) Layer 9 samples: 100.1 ± 8.4 ka (CON-05-06) and 99.3 ± 10.6 ka (CON-5-08). It should be clear that the OSL ages tend to agree, though the authors use quite different statistical and dose rate calculation approaches: Jacobs et al. (2011) use the finite mixture model to extract components from the data and apply weighted beta dose rates to calculate final ages. However, the archaeological interpretation is apparently not straightforward and needs to be resolved. In either interpretation, however, the Aterian appears prior to 100 ka.

The youngest Aterian levels seem to occur in the sites El Harhoura II and Dar es-Soltan I (Fig. 7-5). At El Harhoura II, six samples have been collected from the latest Aterian (Level 3), and these range from 51.6 ± 3.6 ka (EH09-2) to 61.9 ± 4.1 ka (EH09-1) (Jacobs et al., 2012). Age results for Dar es-Soltan I (this study) are more ambiguous, due both to archaeological uncertainty and dose rate issues, but it seems likely that the latest Aterian is older than 50 ka at this site. Unfortunately, deposits from this period seem to have been lost at the nearby site, Dar es-Soltan II, at least in the sampled location (Schwenninger et al., 2010). A significant age gap of approximately 70,000 years was found between adjacent sediment layers, bypassing the period of interest.

The evidence from Contrebandiers is again mixed, but it seems that the last stages of the Aterian may not be represented in the excavated sediments. Schwenninger et al. (2010) report the following ages for the relevant stratigraphy:

Layer 9/10 (underlying): 100.1 ± 8.4 ka (CON-05-06) and 99.3 ± 10.6 ka (CON-05-08),

Layer 8 (final Aterian): 59.4 ± 10.2 ka (CON-05-07),

Layer 7 (overlying): 70.1 ± 3.8 ka (CON-05-10).

This stratigraphic reversal may be due to the use of ICP-MS results for calculation of the external gamma dose rate for sample CON-05-07. Therefore, it is most parsimonious to suggest that the final Aterian occurs some time during the interval 70-100 ka, an age range earlier than that found at the previously discussed sites.

The results published by Jacobs et al. (2011) unfortunately do not clarify this scenario. These authors sampled Aterian levels in three unconnected areas of Contrebandiers: the Central Excavation, Sector IV, and Sector V. Sector V can be disregarded, as samples have not been collected from the highest Aterian level here and OSL ages are within the chronological range of the other two areas. In Sector IV, a single OSL age of 96 ± 8 ka (SC 39) was obtained for an Aterian layer directly underlying Iberomaurusian occupation. The extant Aterian sediments in the Central Area have slightly younger ages, 92 ± 6 ka (SC 31) and 97 ± 7 ka (SC 32), but there are no overlying deposits. Jacobs et al. (2011) do not report correlations for any of their samples with Schwenninger et al.'s (2010) final Aterian Layer 8 or younger sediments. Therefore, it is possible that they have not sampled the latest extant Aterian occupation layers.

Finally, current OSL results from El Mnasra are not applicable due to a seemingly erroneous archaeological stratigraphy. At the top of the stratigraphy were three levels overlying the Aterian. Level 3 was attributed either to the Neolithic (Schwenninger et al. 2010) or to the Iberomaurusian (Jacobs et al. 2012), and the youngest Aterian was found in Level 4. Schwenninger et al. (2010) did not sample either Layers 3 or 4, but obtained an age of 105.5 ± 12.0 ka (ELM-05-04) for the underlying Layer 5a. Jacobs et al. (2012) report ages for the Aterian Layer 4 that range from 94.6 ± 9.7 ka (EM10-3) to 106.7 ± 9.6 ka (EM10-6), but find that the supposedly Iberomaurusian Layer 3 yields ages of 71.6 ± 5.3 ka (EM10-2) and 75.3 ± 5.6 ka (EM10-1). These Layer 3 ages are more than three times older than any dated Iberomaurusian deposit. Further excavations will be necessary to clarify the archaeological progression in the cave, after which it should be possible to relate the sediment ages to the Aterian technocomplex

in a more precise manner. Overall, though, current evidence for the latest Aterian in this region suggests that it ends between 50 ka and 60 ka (Fig. 7-5), although further work is necessary.

7.3.1.2 Strait of Gibraltar

Evidence is sparse from this region. The ESR results from El Aliya, discussed in Section 2.1.9.2, are necessarily imprecise due to uptake estimates and the use of museum samples for which burial locations were unknown (Wrinn and Rink, 2003). Wrinn and Rink's suggested age range for the Aterian (35-60 ka) is possible when compared to other sites, but the site would benefit from further research on the small amount of remaining sediment. The nearby Benzú rockshelter seems to contain only Mousterian archaeology within deposits that have been dated via U-series and OSL ages to between 70 ka and 254 ± 17 ka (Ramos et al., 2008). It is possible, though, that the bulk of the sediments are much older than the 70 ka capping flowstone (Level 10), as the next reported age, 168 ± 11 ka (Shfd020136), is from much lower in the sequence (Level 5).

7.3.1.3 Atlas Mountains

OSL and TL studies have now been published for Taforalt, Rhafas, and Ifri n'Ammar. Based on the previously discussed chronology for Taforalt, the classic Aterian probably existed from 90-100 ka until 37.6 ±3.4 ka. Results from Rhafas indicate a slightly later 'proto-Aterian,' identified as a Mousterian with the addition of tanged lithics (Mercier et al., 2007). Heated lithics from this earliest Aterian level (Level 3a) have been dated via TL to between 60 ± 5 ka (GR73) and 76 ± 8 ka (GR74) (Mercier et al., 2007), while an OSL sample for this layer yielded a concordant age of 74 ± 3.6 ka (Dörschner et al., 2012). Ages for the latest Aterian at this site have not yet been published. The nearby site, Ifri n'Ammar, is more difficult to interpret. Archaeological layers including pedunculates and foliates indicative of the Aterian are interspersed with layers missing these diagnostic lithics. Weighted means of TL dates indicate that the earliest MSA appears around 171 ± 12 ka, followed by a layer including pedunculates and foliates at 145 ± 9 ka. The Aterian markers disappear from the next level (130 ± 8 ka) but

appear again around 83 ± 6 ka (Richter et al., 2010; Richter et al., 2012). So far there is no other site in the region that evinces this progression.

7.3.2 Implications for human evolution

It is clear, based on the dates obtained in this study and other recent OSL publications, that at least the early stages of the Aterian technocomplex are sufficiently old to be relevant to discussions concerning modern *Homo sapiens* in North Africa. Though it is still not entirely clear how the earliest Aterian and Atlantic Coast human fossils relate, the suggested ages of MIS 5.5 or soon after have made these fossil remains a valuable addition to studies of early modern *Homo sapiens*. It is also evident that the modern behaviors which appear during the Aterian are much earlier than had been supposed. Shell beads appear in secure contexts at Taforalt between 80,000 and 90,000 years old, ~75 ka at Rhafas (Dörschner et al., 2012), and in a level with tanged lithics dated to 83 ± 6 ka at Ifri n'Ammar (D'Errico et al., 2009; Richter et al., 2010). El Mnasra has perhaps the most remarkable record, with the previous dating discussion indicating the creation of stone features and pigment use more than 100,000 years ago (Layer 7).

The apparent time depth of this industry, which seems to range from ~37 ka at Taforalt to ~145 ka at Ifri n'Ammar, begs the question of how useful it is to consider this as a single technocomplex. There is also mounting evidence that there are facies of this technocomplex both with and without the characteristic pedunculates. These differences may be diachronic, e.g. Ifri n'Ammar, or synchronic, as suggested by the unusual lack of pedunculates from El Harhoura II during Aterian occupation of the Rabat area (Jacobs et al., 2012). Further work is also necessary to illuminate the emergence and spread of lithic developments. Currently, the sites in the Rabat area have the most consistently early ages for the Aterian, though the age of ~145 ka for the lowest tanged industry at Ifri n'Ammar in northeastern Morocco provides the earliest date. Conversely, the latest Aterian may be evident in the Strait of Gibraltar and northeastern Morocco.

The geographic location of the development of the earliest Aterian and the timing of its spread across Africa have special significance. First, the fossil sequence in Morocco has often been argued to show in situ, local hominin evolution from the more archaic Jebel Irhoud specimens to the Aterian associated fossils, and thence to the Iberomaurusian remains of the upper Palaeolithic (Hublin, 1992; Lahr and Foley, 1994). Based on the dating of the Irhoud fossils to approximately 160 ± 16 ka (Smith et al., 2007), and the earlier supposition that the Aterian fossils might be as much as 100,000 years younger, this in situ evolution seemed to be an appropriately gradual process. It is clear now that the timescales involved have been significantly compressed, and that morphologically distinct individuals existed nearly simultaneously. The implications of this for the evolutionary processes involved depend upon the acceptance of these dates and reevaluation of potential relationships between these fossil remains.

The timing of the earliest Aterian also has profound implications for the interaction of early humans with their environment. In northern Africa, climatic cycles of hyper-aridity and more humid, savannah-like conditions within the area of the present day Sahara desert may have cyclically driven human migration, alternately opening and closing routes north from subsaharan Africa. Environments that remained amenable to hominin occupation, including perhaps the Maghreb (Bouzouggar et al., 2002) and Nile Valley may have received a periodic population influx that was then isolated for tens of millennia in a relatively small geographic area during climatic downturns. And in fact, the relationship of the Mousterian and Aterian seems to fit this pattern, with Mousterian sites rarely if ever found in the Sahara but frequent occurrences of Aterian lithics throughout. Chronologically, the Saharan humid period around 120-125 ka dated by palaeolake and spring sediments in Egypt (Szabo et al., 1995; Smith et al., 2007) and Libya (Armitage et al., 2007), and chemical evidence of running water in “radar rivers” (Osborne et al., 2008) would have been the first opportunity for a locally derived Aterian in either Morocco or Egypt to move across the interior of Northern Africa. Therefore, even with some

regional differences in the timing of maximum humidity, one might logically expect the majority of the Aterian occupation in the Sahara to occur around this time.

Yet while Aterians certainly exploited the periodically available palaeolakes in the Western desert of Egypt (Wendorf et al., 1987), the earliest dated Aterian in the central Sahara is post 90 ka (Cremaschi et al., 1998). Furthermore, Aterian occupation in southern Libya occurs stratigraphically adjacent to large accumulations of aeolian sand that suggest increasing aridity by the time they begin to utilize this environment (Cremaschi and Di Lernia, 1999). Similarly, Aterian artifact scatters show no suggestive concentrations near the "radar rivers" in Egypt (Wendorf et al, 1987), though this may be due to a lack of running water in these channels. Problematically, then, the Aterian appears in both Egypt and Morocco by soon after 125 ka, but there is no evidence for a migration from one point to the other by this time, at least across the Sahara. Garcea (2004) used this circumstance to argue against environmental determinism in archaeology, but it seems necessary to explain this discrepancy.

Chapter Eight

CONCLUSIONS

This project has enlarged the already rapidly expanding Aterian chronological database, as well as provided insights into the successful application of OSL dating in complex environments. A number of techniques for increasing accuracy and precision have also been applied and/or developed during this project, including intrinsic OSL quality control criteria (Section 7.2.1), microsampling (Sections 3.1.2.2, 7.2.2), Bayesian modelling (Sections 4.4, 7.2.3), and spatially-resolved OSL measurement (Chapter 6, Section 7.2.4). Concluding remarks are presented here for each of these aspects.

OSL ages obtained for two sites (Taforalt and Dar es-Soltan I) indicate that the earliest Aterian presence definitely dates back to MIS 5. According to OSL results, the cave of Dar es-Soltan I formed in an aeolianite that was deposited 154.1 ± 20.7 ka. The earliest cave deposit (Group 1) is predominantly marine derived, and likely attributable to MIS 5e, as is the earliest undiagnostic MSA. The earliest Aterian occurs in the next higher deposit (Group 2), from which OSL ages are highly scattered. Radioisotope correlations, and the comparison of dose rate and equivalent dose trends with depth suggest that a number of the calculated ages may be too

young. It seems likely that this Group was deposited ~100 ka or slightly earlier, with a concomitantly early age for the earliest Aterian. The same dosimetric issues occur higher in the sequence, so the latest Aterian, which has been dated via OSL to ~50 ka, may in fact be older than this. Further research on dose rate issues in this cave would be desireable. The situation is clearer at Taforalt, as OSL ages from this project, U-Series dates (Clark-Balzan et al., 2012), and radiocarbon data (N. Barton, pers. comm.) have been used to create an internally consistent chronology. MSA populations appear by ~100 ka, with a classic Aterian facies occurring in sediments that are between 80,000 and 90,000 years old. The latest Aterian at the site has been dated by OSL to 37.6 ±3.4 ka, which may be relatively late in this part of the Maghreb.

Conversely, dating of the Rhafas femur fragment and the re-measurement of the Chaperon Rouge sample are not so clearly related to an early Aterian presence. OSL dating of the sediment from the Rhafas femur fragment yielded an age of 8.43 ± 0.64 ka, which is likely to be an upper limit for the date of last sediment bleaching. Nevertheless, the femur itself may be considerably older, perhaps an Aterian-related fossil. The final interpretation of the femur's age will depend on future excavation data and anatomical investigation of the fragment. Similarly, further investigations are necessary for the site of Chaperon Rouge. Though the sediments underlying the Aterian were dated to 41.1 ± 6.1 ka by Rhodes (1990) via multigrain techniques, this age can no longer be accepted. Instead, this sample is likely to be significantly older but subject to intensive bioturbation. The exact nature and position of the lithic industry, which is scattered within the overlying sands, also requires reappraisal.

Standard OSL dating measures intended to ensure accuracy of final dates met with mixed success during this project. This is because most such measures, which include single grain analysis, dose recoveries, preheat plateau experiments, and aliquot/grain rejection criteria, have been developed in order to test various aspects of equivalent dose measurement. By contrast, relatively little study has been concerned with dose rate change through burial history, e.g. radioisotope mobility. The OSL ages for the Grey Series at Taforalt, which would not have

been questioned except that they were systematically significantly older than the concomitant radiocarbon dates, are likely to be overestimates. This study has suggested that the most likely explanation for this effect is potassium leaching, but there is very little literature with which to compare these results. Similarly, evidence for possible radioisotope scavenging at Dar es-Soltan I was only discovered via elemental correlation analysis, though it is possible that it might have been found via disequilibrium measurements. It is, of course, difficult to generalize OSL results between sites due to the highly individual nature of sedimentary processes. Nevertheless, in complex depositional environments such as caves, it seems that the potential error induced by radioisotope mobility may be significantly greater than usually considered. Techniques such as interpretation of single grain data may lead to a false sense of accuracy, when in fact only analytical precision has been increased.

Microsampling and high density sampling strategies were also tested at Taforalt. Microsamples generally led to higher precision OSL ages, and the use of microsamples to closely bracket sedimentary boundaries seems viable. Calibration and measurement of VSA's led to high data collection efficiency, even with limited sample material available. Yet samples were difficult to work with due to the small amount of sediment collected. There was also some evidence, based on comparison of microsample and standard sample ages, that bleaching during sample collection may be an issue for microsamples in particularly fine or very coarse sediments. Further work with microsamples may be useful in particularly valuable archaeological sections, but different sampling strategies should be investigated (i.e. the use of Kubiena tins and laboratory subsampling of the collected sediment column) and more use should be made of synthetic dosimeters in order to measure in situ gamma doses.

Bayesian models constructed for the OSL results from Dar es-Soltan I and Taforalt were particularly useful for interpreting complex results via a standardized statistical framework. At Taforalt, Bayesian statistics were instrumental in combining results from a large database of samples, which were related via a hierarchy of complex stratigraphic relationships. Via OxCal,

posterior probabilities could be calculated for marker horizons that had not been directly dated with OSL, and these age distributions compared with results from independent dating methods. On the other hand, the scattered results at Dar es-Soltan I made interpretation difficult. In this case, Bayesian modeling provided a framework for understanding the most likely depositional sequence for the major sedimentary groups given the current data.

Finally, this project has demonstrated that SR-OSL measurements are feasible by imaging UV emissions with an EMCCD camera. Low intensity emissions were detected above background levels from both synthetic dosimeters and natural quartz. These emissions could be identified with individual grains and tracked between stimulation cycles, a necessary requirement for an SR-OSL technique. Once software had been developed to account for dark current and unstable background values, quantitative dose recoveries were undertaken. Though recovered doses were within 10% of the given irradiation, error due to user-controlled stimulation/imaging synchronization was significant. To account for this and increase the light collection efficiency of the system, a custom stimulation and imaging mount was designed and built in collaboration with an Oxford instrument designer. Though the system has now been constructed, it was finished too late to include measurement of equivalent doses in this thesis. Further development of the SR-OSL technique is planned, including refinement of the analysis software and integration of equivalent dose measurement with spatially-resolved dose rate measurements. It is hoped that future development of this technique will allow sedimentary microdosimetry to be evaluated in more detail and its effect on equivalent dose overdispersion to be calculated.

OSL age results from Taforalt, Dar es-Soltan I, and possibly Chaperon Rouge support the increasingly early Aterian chronology in Morocco suggested by several other recent publications (see Chapter 7 for details). It is clear that the Aterian technocomplex, which includes early modern behavioural traits and associated human fossils, must be integrated into models of modern *Homo sapiens* development in Africa. As part of this process, correlations between

archaeological excavations and environmental data will require ever increasing levels of precision and accuracy in OSL dating. It is felt that the methods used in this thesis, including Bayesian modeling of complex associations, microsampling, and—in future—the use of SR-OSL and dose rate mapping, may be useful in this undertaking.

References

Adamiec, G., Aitken, M.J. (1998). Dose-rate conversion factors: update. *Ancient TL*, 16(2): 37-50.

Adamiec, G., Heer, A.J., Bluszcz, A. (2012). Statistics of count numbers from a photomultiplier tube and its implications for error estimation. *Radiation Measurements*, 47(9): 746-751.

Aitken, M.J. (1985). *Thermoluminescence Dating*. London: Academic Press.

Aitken, M.J. (1998). *An Introduction to Optical Dating*. Oxford: Oxford University Press.

Aitken, M.J., Xie, J. (1990). Moisture correction for annual gamma dose. *Ancient TL*, 8(2): 6-9.

Aitken, M.J., Clark, P.A., Gaffney, C.F. (1985). Beta and gamma gradients. *Nucl. Tracks Rad. Meas.*, 10(4-6): 647-653.

Alimen, H., Beucher, F., Conrad, G. (1966). Chronologie du dernier cycle pluvial-aride au Sahara nord-occidental. *C.R. Acad. Sci. Paris*., 263: 5-8.

Amani, F., Geraads, D. (1993). Le gisement moustérien du Djebel Irhoud, Maroc: précisions sur la faune et la biochronologie, et description d'un nouveau reste humain. *C.R. Acad. Sci. Paris*, 316: 847-852.

Almond, P.C., Shanhun, F.L., Rieser, U., Shulmeister, J. (2007). 'An OSL, radiocarbon and tephra isochron-based chronology for Birdings Flat loess at Ahuriri Quarry, Banks Peninsula, Canterbury, New Zealand.' *Quaternary Geochronology*, 2(1-4): 4-8.

Andor Technology. (2012). *CCD, EMCCD, and ICCD comparisons.* Retreived November 20, 2012, from http://www.andor.com/learning-academy/ccd,-emccd-and-iccd-comparisons-difference-between-the-sensors.

Ankjærgaard, C., Jain, M. Thomsen, K.J., Murray, A.S. (2010). Optimising the separation of quartz and feldspar optically stimulated luminescence using pulsed excitation. *Radiation Measurements*, 45(7): 778-785.

Antoine, M. (1938). Notes de préhistoire marocaine: XIV--Un cône de résurgence du Paléolithique moyen à Tit Mellil, près de Casablanca. *Bulletin de la Société Préhistorique du Maroc*, 12: 3-95.

Aouadi-Abdeljaouad, N., Belhouchet, L. (2012). Middle Stone Age in Tunisia: Present status of knowledge and recent advances. In: Hublin, J.-J., McPherron, S.P. (Eds.), *Modern Origins: A North African Perspective*. Leipzig, Germany: Springer, pp. 143-156.

Arambourg, C. (1965). Le gisement moustérien et l'Homme du Jebel Irhoud (Maroc). *Quaternaria*, 7: 1-8.

Armitage, S.A., Duller, G.A.T., Wintle, A.G. (2000). Quartz from southern Africa: sensitivity changes as a result of thermal pretreatment. *Radiation Measurements*, 32(5-6): 571-577.

Armitage, S.J., Drake, N.A., Stokes, S., El-Hawat, A., Salem, M.J., White, K., Turner, P., McLaren, S.J. (2007). Multiple phases of North African humidity recorded in lacustrine sediments from the Fazzan Basin, Libyan Sahara. *Quaternary Geochronology*, 2(1-4): 181-186.

Arnold, L.J., Roberts, R.G. (2009). Stochastic modelling of multi-grain equivalent dose (D_e) distributions: Implications for OSL dating of sediment mixtures. *Quaternary Geochronology*, 4(3): 204-230.

Arnold, L.J., Bailey, R.M., Tucker, G.E. (2007). Statistical treatment of fluvial dose distributions from southern Colorado arroyo deposits. *Quaternary Geochronology*, 4(3): 204-230.

Arnold, L.J., Demuro, M., Ruiz, M.N. (2012). Empirical insights into multi-grain averaging effects from "pseudo" single-grain OSL measurements. *Radiation Measurements*, 47(9): 652-658.

Attix, F.H., Roesch, W.C. (1968). *Radiation Dosimetry*. Volume 1. London: Academic Press.

Aznar, M.C., Nathan, R., Murray, A.S., Bøtter-Jensen, L. (2003). Determination of differential dose rates in a mixed beta and gamma field using shielded Al_2O_3: C: Results of Monte Carlo modelling. *Radiation Measurements*, 37(4-5): 329-334.

Bailey, R.M., Arnold, L.J. (2006). Statistical modelling of single grain quartz De distributions and an assessment of procedures for estimating burial dose. *Quaternary Science Reviews*, 25(19-20): 2475-2502.

Bailiff, I.K. (2006). Development of single grain OSL dating of ceramic materials: Spatially resolved measurement of absorbed dose. *Radiation Measurements*, 41(7-8): 744 - 749.

Bailiff, I.K., Mikhailik, V.B. (2003). Spatially-resolved measurement of optically stimulated luminescence and time-resolved luminescence. *Radiation Measurements*, 37(2): 151 - 159.

Ballarini, M., Wallinga, J., Wintle, A. G., Bos, A. J. J. (2007). Analysis of equivalent-dose distributions for single grains of quartz from modern deposits. *Quaternary Geochronology*, 2(1-4): 77-82.

Balout, L. (1965). Le Moustérien du Maghreb. *Quaternaria*, 7: 43-58.

Balter, M. (2011). News Focus: Was North Africa the Launch Pad for Modern Human Migrations? *Science*, 331(6013): 20-23.

Banerjee, D., Murray, A.S., Bøtter-Jensen, L., Lang, A. (2001). Equivalent dose estimation using a single aliquot of polymineral fine grains. *Radiation Measurements*, 33(1): 73-93.

Barbouti, A., Rastin, B. (1983). A study of the absolute intensity of muons at sea level and under various thicknesses of absorber. *J. Phys. G: Nucl. Phys.*, 9: 1577-1595.

Barich, B.E., Garcea, E.A.A., Giraudi, C. (2006). Between the Mediterranean and the Sahara: geoarchaeological reconnaissance in the Jebel Gharbi, Libya. *Antiquity*, 80: 567-582.

Baril, M. (2004). CCD imaging of the infra-red stimulated luminescence of feldspars. *Radiation Measurements,* 38: 81-86.

Barton, R.N.E., Bouzouggar, A., Collcutt, S.N., Schwenninger, J.-L., Clark-Balzan, L. (2009). OSL dating of the Aterian levels at Dar es-Soltan I (Rabat, Morocco) and implications for the dispersal of modern Homo sapiens. *Quaternary Science Reviews*, 28(19-20): 1914-1931.

Barton, R.N.E., Bouzouggar, A., Hogue, J.T., Lee, S., Collcutt, S.N., Ditchfield, P. (In Press). Origins of the Iberomaurusian in NW Africa: New AMS radiocarbon dating of the Middle and Later Stone Age deposits at Taforalt Cave, Morocco. *Journal of Human Evolution*, 10.1016/j.jhevol.2013.06.003: 1-16.

Bateman, M.D., Boulter, C.H., Carr, A.S., Frederick, C.D., Peter, D., Wilder, M. (2007a). Preserving the palaeoenvironmental record in drylands: bioturbation and its significance for luminescence-derived chronologies. *Sedimentary Geology*, 195(1-2): 5-19.

Bateman, M.D., Boulter, C.H., Carr, A.S., Frederick, C.D., Peter, D., Wilder, M. (2007b). Detecting post-depositional sediment disturbance in sandy deposits using optical luminescence. *Quaternary Geochronology*, 2(1-4): 57-64.

Bell, W.T., Zimmerman, D.W. (1978). The effect of HF acid etching on the morphology of quartz inclusions for thermoluminescence dating. *Archaeometry*, 20(1): 63-65.

Berger, R., Fergusson, G.J., Libby, W.F. (1965). UCLA radiocarbon dates IV. *Radiocarbon*, 7: 336-371.

Berland, K., Jacobson, K., French, T., Rajfur, Z. (2003). Electronic cameras for low-light microscopy. *Methods in Cell Biology*, 72: 103-132.

Beyin, A. (2006). The Bab al Mandab vs. the Nile-Levant: An appraisal of the two dispersal routes for early modern humans out of Africa. *African Archaeological Review*, 23(1-2): 5-30.

Biberson, P. (1961). *Le Paléolithique inférieur du Maroc atlantique.* Rabat: Publications du Service des Antiquités Marocaines.

Blackwell, B.A.B., Blickstein, J.I.B. (2000). Considering sedimentary U uptake in external dose rate determinations for ESR and luminescent dating. *Quaternary International*, 68-71: 329-343.

Blondel, J., Aronson, J. (1999). *Biology and Wildlife of the Mediterranean Region*. Oxford: Oxford University Press.

Blouke, M.M., Cowens, M.W., Hall, J.E., Westphal, J.A, Christensen, A.B. (1980). Ultraviolet downconverting phosphor for use with silicon CCD imagers. *Applied Optics*, 19(19): 3318-21.

Bogdanova, L.N., Gavrilov, M.G., Kornoukhov, V.N., Starostin, A.S. (2006). Cosmic muon flux at shallow depths underground. *Physics of Atomic Nuclei*, 69(8): 1293-1298.

Bordes, F. (1976-1977). Moustérien et Atérien. *Quaternaria*, 19: 19-34.

Bortolot, V.J. (2000). A new modular high capacity OSL reader system. *Radiation Measurements,* 32(5-6): 751-757.

Bøtter-Jensen, L., Duller, G.A.T. (1992). A new system for measuring optically stimulated luminescence from quartz samples. *Nucl. Tracks Rad. Meas.*, 20(4): 549-553.

Bøtter-Jensen, L., Duller, G.A.T., Poolton, N.R.J. (1994). Excitation and emission spectrometry of stimulated luminescence from quartz and feldspars. *Radiation Measurements*, 23(2-3): 613-616.

Bøtter-Jensen, L., Bulur, E., Duller, G.A.T., Murray, A.S. (2000). Advances in luminescence instrument systems. *Radiation Measurements*, 32(5-6): 523-528.

Bøtter-Jensen, L., Andersen, C.E., Duller, G.A.T., Murray, A.S. (2003). Developments in radiation, stimulation and observation facilities in luminescence measurements. *Radiation Measurements*, 37(4-5): 535-541.

Bouchra, O., Zouari, K., Ouezdou, H.B., Chkir, N., Causse, C. (1998). Nouvelles données paléoenvironnementales pour le Quaternaire récent en Tunisie centrale (Bassin de Maknassy). *C.R. Acad. Sci. Paris*, 326: 855-861.

Bouzouggar, A., Barton, R.N.E. (2012). The identity and timing of the Aterian in Morocco. In: Hublin, J.-J., McPherron, S.P. (Eds.), *Modern Origins: A North African Perspective*. Leipzig, Germany: Springer, pp. 93-106.

Bouzouggar, A., Kozłowski, J.K., Otte, M. (2002). Étude des ensembles lithiques atériens de la grotte d'El Aliya à Tanger (Maroc). *L'Anthropologie*, 106(2): 207-248.

Bouzouggar, A., Barton, R.N.E., De Araujo Igreja, M. (2007a). A brief overview of recent research into the Aterian and Upper Palaeolithic of Northern and Eastern Morocco. In: Barich, B. (Ed.), *Tra il Sahara e il Mediterraneo: il Jebel Gharbi (Libia) e l'Archeologia del Maghreb* Edizioni Quasar. Scienze dell'Antichità, Storia Archeologia Antopologia 12 (2004-5), pp. 473-488.

Bouzouggar, A., Barton, N., Vanhaeren, M., d'Errico, F., Collcutt, S., Higham, T., Hodge, E., Parfitt, S., Rhodes, E., Schwenninger, J.-L., Stringer, C., Turner, E., Ward, S., Moutmir, A., Stambouli, A. (2007b). 82,000-year-old shell beads from North Africa and implications for the origins of modern human behavior. *P. Natl. Acad. Sci. USA*, 104(24): 9964-9969.

Bouzouggar, A., Barton, R.N.E., Blockley, S., Bronk Ramsey, C., Collcutt, S.N., Gale, R., Higham, T. F. G., Humphrey, L.T., Parfitt, S., Turner, E., Ward, S. (2008). Reevaluating the Age of the Iberomaurusian in Morocco. *African Archaeological Review*, 25(1-2): 3-19.

Bray, H., Bailey, R., Stokes, S. (2002). Quantification of cross-irradiation and cross-illumination using a Risø TL/OSL DA-15 reader. *Radiation Measurements*, 35(3): 275-280.

Brennan, B.J., Lyons, R.G. (1989). Ranges of alpha particles in various media. *Ancient TL*, 7(2): 32-37.

Brennan, B.J., Lyons, R.G., Phillips, S.W. (1991). Attenuation of alpha particle track dose for spherical grains. *Nucl. Tracks Rad. Meas.*, 18(1-2): 249-253.

Brill, D., Klasen, N., Brückner, H., Jankaew, K., Scheffers, A., Kelletat, D., Scheffers, S. (2012). OSL dating of tsunami deposits from Phra Thong Island, Thailand. *Quaternary Geochronology*, 10: 224-229.

Bronk Ramsey, C. (2009a). Bayesian analysis of radiocarbon dates. *Radiocarbon*, 51(1): 337-360.

Bronk Ramsey, C. (2009b). Dealing with outliers and offsets in radiocarbon dating. *Radiocarbon,* 51(3): 1023-1045.

Bronk Ramsey, C., Dee, M., Lee, S., Nakagawa, T., Staff, R. (2010). Developments in the calibration and modelling of radiocarbon dates. *Radiocarbon, 52*(3): 953-961.

Burggraaf, D., Haskell, E.H. (1994). A software package for TL/OSL spectrometry and extraction of glow curves from individual grains. *Radiation Measurements,* 23(2-3): 537.

Camps, G. (1974). Tableau chronologique de la Préhistoire récente du Nord de l'Afrique. Deuxième synthèse des datations obtenues par le carbone 14. *Bull. Soc. Préhist. Fr.*, 71(1): 261-278.

Camps, G. (1975). The prehistoric cultures of North Africa: Radiocarbon chronology. In: Wendorf, F., Marks, A.E. (Eds.), *Problems in prehistory: North Africa and the Levant.* Dallas: SMU Press, pp. 181-192.

Caton-Thompson, G. (1946). The Aterian industry : Its place and significance in the Palaeolithic world. *J. R. Anthropol. Inst.G.*, 76(2): 87-130.

Caton-Thompson, G. (1952). *Kharga Oasis in prehistory*. London: University of London, Athlone Press.

Choubert, G., Faure-Muret, A., Maarleveld, G.C. (1967). Nouvelles dates isotopiques du Quaternaire marocain et leur signification. *C.R. Acad. Sci. Paris*, 264: 434-437.

Clark, J.D. (1964). The prehistoric origins of African culture. *Journal of African History*, 5(2): 161-183.

Clark, J.D. (1971). An archaeological survey of northern Aïr and Tenere. *Geographical Journal*, 137(4): 455-457.

Clark, J.D. (1982). The cultures of the Middle Palaeolithic/Middle Stone Age. In: Clark, J.D. (Ed.), *The Cambridge History of Africa: From the Earliest Times to c. 500 B.C.* Cambridge: Cambridge University Press, pp. 248-341.

Clark, J.D. (1993). The Aterian of the central Sahara. In: Krzyzaniak, L., Kobusiewicz, M., Alexander, J. (Eds.), *Environmental change and human culture in the Nile Basin and Northern Africa until the second millennium B.C.* Poznań: Poznań Archaeological Museum, pp. 49-67.

Clark-Balzan, L. (2007). *A comparative study of single and multigrain luminescence measurements of cave sediments from Morocco.* MSc Thesis. University of Oxford: United Kingdom.

Clark-Balzan, L., Schwenninger, J.-L. (2012). First steps toward spatially resolved OSL dating with electron multiplying charge-coupled devices (EMCCDs): System design and image analysis. *Radiation Measurements*, 47(9): 797-802.

Clark-Balzan, L., Candy, I., Schwenninger, J.-L., Bouzouggar, A., Blockley, S., Nathan, R., and Barton, R. N. E. (2012). Coupled U-series and OSL dating of a Late Pleistocene cave sediment sequence, Morocco, North Africa: Significance for constructing Palaeolithic chronologies. *Quaternary Geochronology*, 12: 53-64.

Close, A.E. (1980). Current research and recent radiocarbon dates from northern Africa. *The Journal of African History*, 21(2): 145-167.

Close, A.E. (1984). Current research and recent radiocarbon dates from northern Africa, II. *The Journal of African History*, 25(1): 1-24.

Courty, M.-A., Vallverdu, J. (2001). The microstratigraphic record of abrupt climate changes in cave sediments of the western Mediterranean. *Geoarchaeology*, 16(5): 467- 500.

Courty, M.-A., Goldberg, P., Macphail, R. (1989). Soils and micromorphology in archaeology. Cambridge: Cambridge University Press.

Cremaschi, M. (1996). Current research on the prehistory of the Tadrart Acacus (Libyan Sahara): Survey and excavations 1991 -1995. *Nyame Akuma*, 45: 50-59.

Cremaschi, M., Di Lernia, S. (1999). The 1993 and 1994 excavations: Geomorphology, stratigraphic context and dates. In: Di Lernia, S. (Ed.), *The Uan Afuda Cave: Hunter-gatherer societies of central Sahara*. Rome: All'Insegna del Giglio, pp. 9-26.

Cremaschi, M., Di Lernia, S., Garcea, E.A.A. (1998). Some insights on the Aterian in the Libyan Sahara: Chronology, environment, and archaeology. *African Archaeological Review*, 15(4): 261-286.

Debénath, A. (1972). Nouvelles fouilles à Dar Es-Soltane, note préliminaire. *Bull. Soc. Préhist. Fr.*, 69(6): 178-179.

Debénath, A., Raynal, J.-P., Texier, J.-P. (1982). Position stratigraphique des restes humains paléolithiques marocains sur la base des travaux récents. *C.R. Acad. Sci. Paris*, 294: 1247-1250.

Debénath, A., Raynal, J.-P., Roche, J., Texier, J.-P., Ferembach, D. (1986). Stratigraphie, habitat, typologie et devenir de l'Atérien Marocain: Données récentes. *L'Anthropologie*, 90(2): 233-246.

Debenham, N.C., Driver, H.S.T., Walton, A.J. (1982). Anomalies in the TL of young calcites. *PACT*, 6: 555-562.

Delibrias, G., Guillier, M.-T., Labeyrie, J. (1974). GIF natural radiocarbon measurements VIII. *Radiocarbon*, 16(1): 15-94.

Delibrias, G., Guillier, M.-T., Labeyrie, J. (1982). GIF Natural Radiocarbon Measurments IX. *Radiocarbon*, 24(3): 291-343.

d'Errico, F., Vanhaeren, M., Barton, N., Bouzouggar, A., Mienis, H., Richter, D., Hublin, J.-J., McPherron, S.P., Lozouet, P. (2009). Additional evidence on the use of personal ornaments in the Middle Paleolithic of North Africa. *P. Natl. Acad. Sci. USA*, 106(38): 16051-16056.

DeWitt, R., Klein, D.M. (2009). LuCIDD: A luminescence instrument with confocal and imaging units for dating and dosimetry. Conference on Micro-Raman Spectroscopy and Luminescence Studies in the Earth and Planetary Sciences. April 2-4. Mainz, Germany.

Dibble, H.L., Aldeias, V., Alvarez-Fernández, Blackwell, B.A.B., Hallett-Desguez, E., Jacobs, Z., Goldberg, P., Lin, S.C., Morala, A., Meyer, M.C., Olszewski, D.I., Reed, K., Reed, D., Rezek, Z., Richter, D., Roberts, R.G., Sandgathe, D., Schurmans, U., Skinner, A.R., Steele, T.E., El-Hajraoui, M. (2012). New excavations at the site of Contrebandiers Cave, Morocco. *Paleoanthropology*, 145-201.

Dörschner, N., Fitzsimmons, K.E., Ditchfield, P.D., McPherron, S.P., Bouzouggar, A., Hublin, J.-J. (2012). *Single grain OSL-dating of palaeolithic sediments from the Rhafas Cave site (NE Morocco).* Poster presented at the ESHE 2nd Annual Meeting. September 21-22. Bordeaux, France.

Duller, G.A.T. (1994). Luminescence dating of sediments using single aliquots: New procedures. *Quaternary Science Reviews*, 13(2): 149-156.

Duller, G.A.T. (2003). Distinguishing quartz and feldspar in single grain luminescence measurements. *Radiation Measurements*, 37(2): 161-165.

Duller, G.A.T. (2007). Analyst Version 3.24. Aberystwyth: University of Wales.

Duller, G.A.T. (2012a). Cross-talk during single grain optically stimulated luminescence measurements of quartz and feldspar. *Radiation Measurements*, 47(3): 219-224.

Duller, G.A.T. (2012b). Improving the accuracy and precision of equivalent doses determined using the optically stimulated luminescence signal from single grains of quartz. *Radiation Measurements*, 47(9): 770-777.

Duller, G.A.T., Bøtter-Jensen, L., Markey, B.G. (1997). A luminescence imaging system based on a CCD camera. *Radiation Measurements*, 27(2): 91-99.

Duller, G.A.T., Bøtter-Jensen, L., Murray, A.S., Truscott, A.J. (1999). Single grain laser luminescence (SGLL) measurements using a novel automated reader. *Nucl. Instrum. Meth. B*, 155(4): 506-514.

El Hajraoui, M.A. (1993). Nouvelles découvertes néolithiques et atériennes dans la région de Rabat (Grotte d'El Mnasra). *Mediterraneô*, 2: 105-121.

Ennouchi, É. (1962). Un crâne d'Homme ancien au Jebel Irhoud (Maroc). *C.R. Acad. Sci. Paris*, 254: 4330-4332.

Erlandson, J.M. (2001). The archaeology of aquatic adaptations: Paradigms for a new millennium. *Journal of Archaeological Research*, 9(4): 287-350.

Etiégni, L., Campbell, A.G. (1991). Physical and chemical characteristics of wood ash. *Bioresource Technology*, 37(2): 173-178.

Feathers, J.K. (1996). Luminescence dating and modern human origins. *Evolutionary Anthropology*. 5(1): 25-36.

Feathers, J.K. (2003). Single-grain OSL dating of sediments from the Southern High Plains, USA. *Quaternary Science Reviews*, 22(10-13): 1035-1042.

Ferembach, D. (1959). Les restes humains épipaléolithiques de la grotte de Taforalt (Maroc oriental). *C. R. Hebd. Acad. Sci.*, 248: 3465-3467.

Ferembach, D. (1976). Les restes humains de la Grotte de Dar-es-Soltane 2 (Maroc) Campagne 1975. *Bull. et Mém. de la Soc. d'Anthrop. de Paris*, 3: 183-193.

Ferring, C.R. (1975). The Aterian in North African prehistory. In: Wendorf, F., Marks, A.E. (Eds.), *Problems in Prehistory: North Africa and the Levant.* Dallas: SMU Press, pp. 113-126.

Fiebig, M., Preusser, F. (2007). Investigating the amount of zeroing in modern sediments of River Danube, Austria. *Quaternary Geochronology*, 2(1-4): 143-149.

Fleming, S. (1979). *Thermoluminscence techniques in archaeology*. Oxford: Clarendon Press.

Forrest, B., Rink, W.J., Bicho, N., Ferring, C.R. (2003). OSL ages and possible bioturbation signals at the Upper Paleolithic site of Lagoa do Bordoal, Algarve, Portugal. *Quaternary Science Reviews*, 22: 1279-1285.

Gaillard, F. (2009). *Anterior view of the femur—annotated.* Retrieved November 29, 2012 from http://en.wikipedia.org/wiki/File:Fumur_Anterior_annoted.png.

Galbraith, R.F. (2002). A note on the variance of a background-corrected OSL count. *Ancient TL*, 20: 49-51.

Galbraith, R.F. (2003). A simple homogeneity test for estimates of dose obtained using OSL. *Ancient TL*, 21(2): 75-77.

Galbraith, R.F., Green, P.F. (1990). Estimating the component ages in a finite mixture. *Nucl. Tracks Rad. Meas.*, 17(3): 197-206.

Galbraith, R.F., Roberts, R.G. (2012). Statistical aspects of equivalent dose and error calculation and display in OSL dating: An overview and some recommendations. *Quaternary Geochronology*, 11: 1-27.

Galbraith, R.F., Roberts, R.G., Laslett, G.M., Yoshida, H., Olley, J.M. (1999). Optical dating of single and multiple grains of quartz from Jinmium rock shelter, Northern Australia: Part I, Experimental design and statistical models. *Archaeometry*, 41(2): 339-364.

Garcea, E.A.A. (2004). Crossing deserts and avoiding seas: Aterian North African-European relations. *Journal of Anthropological Research*, 60(1): 27-53.

Garcea, E.A.A. (2012). Modern human desert adaptations: A Libyan perspective on the Aterian complex. In: Hublin, J.-J., McPherron, S.P. (Eds.), *Modern Origins: A North African Perspective*. Leipzig, Germany: Springer, pp. 127-142.

Garcea, E.A.A., Giraudi, C. (2006). Late Quaternary human settlement patterning in the Jebel Gharbi. *Journal of Human Evolution*, 51: 411-421.

Gaza, R., Bulur, E., McKeever, S.W.S., Soares, C.G. (2006). Experimental determination of the dose deposition profile of a ^{90}Sr beta source. *Radiation Protection* Dosimetry, 120(1): 33-37.

Geraads, D. (2012). The faunal context of human evolution in the Late Middle/Late Pleistocene of Northwestern Africa. In: Hublin, J.-J., McPherron, S.P. (Eds.), *Modern Origins: A North African Perspective*. Leipzig, Germany: Springer, pp. 49-60.

Gliganic, L.A., Jacobs, Z., Roberts, R.G., Domínguez-Rodrigo, M., Mabulla, A.Z.P. (2012). New ages for Middle and Later Stone Age deposits at Mumba rockshelter, Tanzania: Optically stimulated luminescence dating of quartz and feldspar grains. *Journal of Human Evolution*, 62(4): 533-547.

Greilich, S., (2004). *Uber die Datierung von Gesteinsoberflächen mittels optisch stimulierter Lumineszenz*. Ph.D. Thesis. Ruprecht-Karls-Universität Heidelberg: Germany.

Greilich, S., Wagner, G.A. (2006). Development of a spatially resolved dating technique using HR-OSL. *Radiation Measurements*, 41(7-8): 738-743.

Greilich, S., Glasmacher, U.A., Wagner, G.A. (2002). Spatially resolved detection of luminescence: A unique tool for archaeochronometry. *Naturwissenschaften*, 89(8): 371-5.

Greilich, S., Glasmacher, U.A., Wagner, G.A. (2005). Optical dating of granitic stone surfaces. *Archaeometry*, 47(3): 645- 665.

Gruet, M. (1950). Note préliminaire sur le gisement moustérien d'El Guettar. *Bull. Soc. Préhist. Fr.*, 47(5): 232-241.

Gruet, M., Zelle, M. (1955). Découverte de sphères a Windhoeck (South West Africa). In: Balout, L. (Ed.), *Actes du IIéme Congrès Panafricain de Préhistoire d'Alger 1952.* Casablanca, Morocco: Edita, pp. 457-460.

Grün, R. (1986). Beta dose attenuation in thin layers. *Ancient TL*, 4(1): 1-8.

Grün, R., Stringer, C., McDermott, F., Nathan, R., Porat, N., Robertson, S., Taylor, L., Mortimer, G., Eggins, S., McCulloch, M. (2005). U-series and ESR analyses of bones and teeth relating to the human burials from Skhul. *Journal of Human Evolution*, 49(3): 316-34.

Guérin, G., Mercier, N. (2012). Field gamma spectrometry, Monte Carlo simulations and potential of non-invasive measurements. *Geochronometria*, 39(1): 40-47.

Guérin, G., Mercier, N., Nathan, R., Adamiec, G., Lefrais, Y. (2012). On the use of the infinite matrix assumption and associated concepts: A critical review. *Radiation Measurements*, 47(9): 778-785.

Guibert, P., Lahaye, C., Bechtel, F. (2009). The importance of U-series disequilibrium of sediments in luminescence dating: A case study at the Roc de Marsal Cave (Dordogne, France). *Radiation Measurements*, 44(3): 223-231.

Harrison, D.J. (1993). *Industrial Minerals Laboratory Manual: Limestone*. Technical Report WG/92/29. Keyworth, UK: British Geological Survey.

Hashimoto, T., Koyanagi, A., Yokosaka, K., Hayashi, Y., Sotobayashi, T. (1986). Thermoluminescence color images from quartzs of beach sands. *Geochemical Journal*, 20(3): 111-118.

Hashimoto, T., Yokosaka, K., Habuki, H., (1987). Emission properties of thermoluminescence from natural quartz-blue and red TL response to absorbed dose. *Int. J. Rad. Appl. Instrum. D.*, 13(1): 57-66.

Hashimoto, T., Usuda, H., Yawata, T. (2002). Color images of infrared stimulated luminescence (IRSL) from granite slices exposed to radiations. *Ancient TL*, 20(1): 19-23.

Hassko, B., Guillet, B., Jaegy, R., Coppens, R. (1974). Nancy natural radiocarbon measurements III. *Radiocarbon*, 16(1): 118-130.

Hawkins, A.L. (2001). *Getting a handle on tangs: Defining the Dakleh Unit of the Aterian Technocomplex-A study in surface archaeology from Dakleh Oasis, Western Desert, Egypt.* Ph.D. Thesis. University of Toronto: Canada.

Hawkins, A.L. (2012). The Aterian of the oases of the Western Desert of Egypt: Adaptation to changing climatic conditions? In: Hublin, J.-J., McPherron, S.P. (Eds.), *Modern Origins: A North African Perspective*. Leipzig, Germany: Springer, pp. 157-175.

Hawkins, A.L., Kleindienst, M.R. (2002). Lithic raw material usages during the Middle Stone Age at Dakhleh Oasis, Egypt. *Geoarchaeology*, 17(6): 601-624.

Haynes, V., Haas, H. (1974). Southern Methodist University Radiocarbon Date List II. *Radiocarbon*, 16(3): 368-380.

Heath, R.L. (1997). *Scintillation spectrometry.* Revised edition of Report IDO-16880-1 for the Idaho National Engineering and Environmental Laboratory. Retrieved July 25, 2013, from http://www.inl.gov/gammaray/catalogs/pdf/naicat.pdf.

Henshilwood, C.S., d'Errico, F., Yates, R., Jacobs, Z., Tribolo, C., Duller, G.A.T., Mercier, N., Sealy, J.C., Valladas, H., Watts, I., Wintle, A.G. (2002). Emergence of modern human behavior: Middle Stone Age engravings from South Africa. *Science*, 295(5558): 1278-1280.

Hong Kong Observatory. (2012). *Climatological Information for Africa*. Retrieved September 15, 2012, from http://www.hko.gov.hk/wxinfo/climat/world/eng/africa/africa_e.htm.

Howe, B. (1967). *The palaeolithic of Tangier, Morocco: Excavations at Cape Ashakar, 1939-1947*. Cambridge: Peabody Museum.

Hublin, J.J. (1992). Recent human evolution in northwestern Africa. *Philos. T. Roy. Soc. B*, 337(1280): 185-91.

Hublin, J.-J., Verna, C., Bailey, S., Smith, T., Olejniczak, A., Sbihi-Alaoui, F.Z., Zouak, M. (2012). Dental evidence from the Aterian human populations of Morocco. In: Hublin, J.-J., McPherron, S.P. (Eds.), *Modern Origins: A North African Perspective*. Leipzig, Germany: Springer, pp. 189-204.

Humphrey, L., Bello, S.M., Turner, E., Bouzouggar, A., Barton, N. (2012). Iberomaurusian funerary behaviour: evidence from Grotte des Pigeons, Taforalt, Morocco. *Journal of Human Evolution*, 62(2): 261-73.

Huntley, D.J., Godfrey-Smith, D.I., Thewalt, M.L.W. (1985). Optical dating of sediments. *Nature*. 313: 105-107.

Huntley, D.J., Godfrey-Smith, D.I., Haskell, E.H. (1991). Light-induced emission spectra from some quartz and feldspars. *Int. J. Rad. Appl. Instrum. D.*, 18(1-2): 127-131.

Ibach, H., Lüth, H. (2009). *Solid-state physics: An introduction to Principles of Materials Science.* Berlin: Springer-Verlag.

Ingley, R., Smith, D.R., Holland, A.D. (2009). Life testing of EMCCD gain characteristics. *Nucl. Instrum. Meth. A.*, 600(2): 460-465.

Iovita, R. (2011). Shape variation in Aterian tanged tools and the origins of projectile technology: A morphometric perspective on stone tool function. *PLOS One*, 6(12): p. E29029.

Jacobs, Z., Duller, G.A.T., Wintle, A.G. (2003). Optical dating of dune sand from Blombos Cave, South Africa: II-single grain data. *Journal of Human Evolution*, 44: 613-625.

Jacobs, Z., Duller, G.A.T., Wintle, A.G., Henshilwood, C.S. (2006). Extending the chronology of deposits at Blombos Cave, South Africa, back to 140 ka using optical dating of single and multiple grains of quartz. *Journal of Human Evolution*, 51: 255-273.

Jacobs, Z., Roberts, R.G., Galbraith, R.F., Deacon, H.J., Grün, R., Mackay, A., Mitchell, P., Vogelsang, R., Wadley, L. (2008a). Ages for the Middle Stone Age of Southern Africa: Implications for human behavior and dispersal. *Science*, 322(5902): 733-735.

Jacobs, Z., Wintle, A.G., Roberts, R.G., Duller, G.A.T. (2008b). Equivalent dose distributions from single grains of quartz at Sibudu, South Africa: context, causes and consequences for optical dating of archaeological deposits. *Journal of Archaeological Science*, 35(7): 1808-1820.

Jacobs, Z., Meyer, M.C., Roberts, R.G., Aldeias, V., Dibble, H., El Hajraoui, M.A. (2011). Single-grain OSL dating at La Grotte des Contrebandiers ("Smugglers" Cave'), Morocco: improved age constraints for the Middle Paleolithic levels. *Journal of Archaeological Science*, 38(12): 3631-3643.

Jacobs, Z., Roberts, R.G., Nespoulet, R., El Hajraoui, M.A., Debénath, A. (2012). Single-grain OSL chronologies for Middle Palaeolithic deposits at El Mnasra and El Harhoura 2, Morocco: implications for Late Pleistocene human-environment interactions along the Atlantic coast of northwest Africa. *Journal of Human Evolution*, 62(3): 377-94.

Jacobs, Z., Hayes, E.H., Roberts, R.G., Galbraith, R.F., Henshilwood, C.S. (2013). An improved OSL chronology for the Still Bay layers at Blombos Cave, South Africa: Further tests of single-grain dating procedures and a re-evaluation of the timing of the Still Bay industry across southern Africa. *Journal of Archaeological Science*, 40(1): 579-594.

Jain, M., Singhvi, A.K. (2001). Limits to depletion of blue-green light stimulated luminescence in feldspars: implications for quartz dating. *Radiation Measurements*, 33(6): 883-892.

Jain, M., Murray, A.S., Bøtter-Jensen, L., Wintle, A.G. (2005). A single-aliquot regenerative-dose method based on IR (1.49 eV) bleaching of the fast OSL component in quartz. *Radiation Measurements*, 39(3): 309-318.

Kalchgruber, R., Fuchs, M., Murray, A.S., Wagner, G.A. (2003). Evaluating dose-rate distributions in natural sediments using α-Al_2O_3:C grains. *Radiation Measurements*, 37(4-5): 293-297.

Krbetschek, M.R., Rieser, U. (1995). Luminescence spectra of alkalifeldspars and plagioclases. *Radiation Measurements*, 24(4): 473-477.

Krbetschek, M., Rieser, U., Zoller, L., Heinicke, J. (1994). Radioactive disequilibria in palaeodosimetric dating of sediments. *Radiation Measurements*, 23(2-3): 485-489.

Krbetschek, M., Götze, J., Dietrich, A., Trautmann, T. (1997). Spectral information from minerals relevant for luminescence dating. *Radiation Measurements*, 27(5-6): 695-748.

Kuhn, R., Trautmann, T., Singhvi, A.K., Krbetschek, M.R., Wagner, G.A., Stolz, W. (2000). A study of thermoluminescence emission spectra and optical stimulation spectra of quartz from different provenances. *Radiation Measurements*, 32(5-6): 653-657.

Lacombe, J.P., Daugas, J.P., Sbihi-Alaoui, F.Z. (1990). Etude anthropologique préliminaire des sépultures néolithiques de la grotte d'El Mnasra (Témara, Maroc). *Bulletin de la Société d'Anthropologie du Sud-Ouest*, 26: 163-176.

Lahr, M.M., Foley, R.A. (1994). Multiple Dispersals and Modern Human Origins. *Evolutionary Anthropology*, 3(2): 48-60.

Lecointre, G. (1916). Quelques résultats d'une mission dans le Ghrab (Maroc occidental), en 1914. *C.R. Acad. Sci. Paris*, 162: 719.

Lefèvre, D., Raynal, J.P. (2002). Les formations plio-pléistocènes de Casablanca et la chronostratigraphie du Quaternaire marin du Maroc revisitées. *Quaternaire*, 13(1): 9-21.

Linstädter, J. (2008). The Epipalaeolithic-Neolithic transition in the Mediterranean region of Northwest Africa. *Quartär*, 55: 41-62.

Lomax, J., Hilgers, A., Twidale, C.R., Bourne, J.A., Radtke, U. (2007). Treatment of broad palaeodose distributions in OSL dating of dune sands from the western Murray Basin, South Australia. *Quaternary Geochronology*, 2(1-4): 51-56.

Lowick, S.E., Preusser, F., Pini, R., Ravazzi, C. (2010). Underestimation of fine grain quartz OSL dating towards the Eemian: Comparison with palynostratigraphy from Azzano Decimo, northeastern Italy. *Quaternary Geochronology*, 5(5): 583-590.

Magee, J.W., Miller, G.H., Spooner, N.A., Questiaux, D.G., McCulloch, M.T., Clark, P.A. (2009). Evaluating Quaternary dating methods: Radiocarbon, U-seres, luminescence, and amino acid racemization dates of a late Pleistocene emu egg. *Quaternary Geochronology*, 4(2): 84-92.

Magnan, P. (2003). Detection of visible photons in CCD and CMOS: A comparative view. *Nucl. Instrum. Meth. A*, 504: 199-212.

Malik, S.R., Durrani, S.A., Fremlin, J.H. (1973). A comparative study of the spatial distribution of uranium and of TL-producing minerals in archaeological materials. *Archaeometry,* 15(2): 249-253.

Mariotti, V., Bonfiglioli, B., Facchini, F., Condemi, S., Belcastro, M.G. (2009). Funerary practices of the Iberomaurusian population of Taforalt (Tafoughalt; Morocco, 11-12,000BP): New hypotheses based on a grave by grave skeletal inventory and evidence of deliberate human modification of the remains. *Journal of Human Evolution*, 56(4): 340-54.

Markey, B.G., Bøtter-Jensen, L., Duller, G.A.T. (1997). A new flexible system for measuring thermally and optically stimulated luminescence. *Radiation Measurements*, 27(2): 83-89.

Martin, C.E., McCulloch, M.T. (1999). Nd-Sr isotopic and trace element geochemistry of river sediments and soils in a fertilized catchment, New South Wales, Australia. *Geochimica et Cosmochimica Acta*, 63(2): 287-305.

Martínez-Aguirre, A., García-León, M., Ivanovich, M. (1994). The distribution of U, Th and ^{226}Ra derived from the phosphate fertilizer industries on an estuarine system in Southwest Spain. *Journal of Environmental Radioactivity*, 22(2): 155-177.

Martini, M., Fasoli, M., Galli, A. (2009). Quartz OSL emission spectra and the role of $[AlO_4]^\circ$ recombination centres. *Radiation Measurements*, 44(5-6): 458-461.

Mayya, Y.S., Morthekai, P., Murari, M.K., Singhvi, A.K. (2006). Towards quantifying beta microdosimetric effects in single-grain quartz dose distribution. *Radiation Measurements*, 41(7-8): 1032-1039.

McBrearty, S., Brooks, A.S. (2000). The revolution that wasn't: A new interpretation of the origin of modern human behavior. *Journal of Human Evolution*, 39(5): 453-563.

McClure, H.A. (1994). A new Arabian stone tool assemblage and notes on the Aterian industry of North Africa. *Arabian Archaeology and Epigraphy*, 5: 1-16.

McCulloch, I., Spooner, N.A., Jones, D. (2011). A high-sensitivity photon counting imaging system (PCIS) for luminescence analysis. *Radiation Measurements*, 46(12): 1566-1570.

McFee, C. J. (1995). The use of an imaging photon detector for luminescence dating. D.Phil. Thesis. University of Oxford: United Kingdom.

Mejdahl, V. (1979). Thermoluminescence dating: Beta-dose attenuation in quartz grains. *Archaeometry*, 21(1): 61-72.

Mejdahl, V., Bøtter-Jensen, L. (1997). Experience with the SARA OSL method. *Radiation Measurements*, 27(2): 291-294.

Mercier, N. (1995). TL Dates of Burnt Flints from Jelinek's Excavations at Tabun and their implications. *Journal of Archaeological Science*, 22(4): 495-509.

Mercier, N, Wengler, L., Valladas, H., Joron, J., Froget, L., Reyss, J. (2007). The Rhafas Cave (Morocco): Chronology of the Mousterian and Aterian archaeological occupations and their implications for Quaternary geochronology based on luminescence (TL/OSL) age determinations. *Quaternary Geochronology*, 2(1-4): 309-313.

Michel, P., Campmas, É., Stoetzel, E., Nespoulet, R., El Hajraoui, M.A., Amani, F. (2009). La macrofaune du Pléistocène supérieur d'El Harhoura 2 (Témara, Maroc): Données préliminaires. *L'Anthropologie*, 113(2): 283-312.

Mikdad, A., Moser, J., Nami, M., Eiwanger, J. (2004). La stratigraphie du site d'Ifri n'Ammar (Rif Oriental, Maroc): Premiers résultats sur les dépôts du Paléolithique moyen. *Beitr. Allgem. Vergleich. Archäol.*, 24: 125-137.

Millard, A.R., Hedges, R.E.M. (1995). The role of the environment in uranium uptake by buried bone. *Journal of Archaeological Science*, 22(2): 239-250. doi:10.1006/jasc.1995.0025

Minugh-Purvis, N. (1993). Reexamination of the immature hominid maxilla from Tangier, Morocco. *Am. J. Phys. Anthropol.*, 92(449-461).

Mitterer, R.M. (1974). Pleistocene stratigraphy in southern Florida based on amino acid diagenesis in fossil Mercenaria. *Geology*, 2: 425-428.

Moomaw, B. (2007). Camera technologies for low light imaging: Overview and relative advantages. *Methods in Cell Biology*, 81: 251-283.

Morel, J. (1974). Nouvelles datations absolues de formations littorales et de gisements préhistoriques de l'Est algérien. *Bull. Soc. Préhist. Fr.*, 71(4): 103-105.

Moyer, C.C. (2003). *The organisation of lithic technology in the Middle and Early Upper Palaeolithic industries at the Haua Fteah, Libya*. D.Phil. Thesis. University of Cambridge: United Kingdom.

Murray, A.S., Olley, J.M. (2002). Precision and accuracy in the optically stimulated luminescence dating of sedimentary quartz: A status review. *Geochronometria*, 21: 1-16.

Murray, A.S., Roberts, R.G. (1997). Determining the burial time of single grains of quartz using optically stimulated luminescence. *Earth Planet. Sc. Lett.*, 152(1-4): 163-180.

Murray, A.S., Roberts, R.G. (1998). Measurement of the equivalent dose in quartz using a regenerative-dose single-aliquot protocol. *Radiation Measurements*, 29(5): 503-515.

Murray, A.S., Wintle, A.G. (2000). Luminescence dating of quartz using an improved single-aliquot regenerative-dose protocol. *Radiation Measurements*, 32: 57-73.

Murray, A.S., Funder, S. (2003). Optically stimulated luminescence dating of a Danish Eemian coastal marine deposit: a test of accuracy. *Quaternary Science Reviews*, 22: 1177-1183.

Murray, A.S., Wintle, A.G. (2003). The single aliquot regenerative dose protocol: potential for improvements in reliability. *Radiation Measurements*, 37(4-5): 377-381.

Nathan, R., Grün, R. (2003). Gamma dosing and shielding of a human tooth by a mandible and skull cap: Monte Carlo simulations and implications for the accuracy of ESR dating of tooth enamel. *Ancient TL*, 21(2): 79-84.

Nathan, R.P., Mauz, B. (2008). On the dose-rate estimate of carbonate-rich sediments for trapped charge dating. *Radiation Measurements,* 43: 14 - 25.

Nathan, R.P., Thomas, P.J., Jain, M., Murray, A.S., Rhodes, E.J. (2003). Environmental dose rate heterogeneity of beta radiation and its implications for luminescence dating: Monte Carlo modelling and experimental validation. *Radiation Measurements*, 37: 305-13.

Natural Stone Council. (2010). *Material Fact Sheet: Sandstone*. New Hampshire, US. http://isse.utk.edu/ccp/projects/naturalstone/pdfs/MFS_sandstone.pdf.

Nespoulet, R., Debénath, A., El Hajraoui, A., Michel, P., Campmas, E., Oujaa, A., Ben-Ncer, A., Lacombe, P., Amani, F., Stoetzel, E., Boudad, L. (2008a). Le context archéologique des restes humains Atériens de la région de Rabat-Témara (Maroc): Apport des fouilles des grottes d'El Mnasra et d'El Harhoura 2. In: Aouraghe, H., Haddoumi, H., El Hammouti, K.

(Eds.). *Actes du 4ème Colloque des Quaternaristes Marocains, Oujda 2007.* Oujda, Morocco: Publications de la Faculté des Sciences d'Oujda, pp. 356-375.

Nespoulet, R., El Hajraoui, M.A., Amani, F., Ben-Ncer, A., Debénath, A., El Idrissi, A., Lacombe, J.-P., Michel, P., Oujaa, A., Stoetzel, E. (2008b). Palaeolithic and Neolithic Occupations in the Témara Region (Rabat, Morocco): Recent Data on Hominin Contexts and Behavior. *African Archaeological Review*, 25: 21-39.

Neuville, R., Ruhlmann, A. (1941). *La place du Paleolithique Ancien dans le Quaternaire Marocain*. Casablanca: Librairie Farairre.

Obara, B. (2007). Identification of transcrystalline microcracks observed in microscope images of a dolomite structure using image analysis methods based on linear structuring element processing. *Computers and Geosciences*, 33(2): 151-158.

Occhietti, S., Raynal, J.-P., Pichet, P., Texier, J.-P. (1993). Aminostratigraphie du dernier cycle climatique au Maroc atlantique, de Casablanca à Tanger. *C.R. Acad. Sci. Paris*, 317: 1625-1632.

Oh, Y.A. (2012). *A multi-proxy approach to examining palaeoenvironmental signals and tephrochronology during the Middle Palaeolithic and Epipalaeolithic phases at Grotte des Pigeons, Taforalt, Morocco.* D.Phil. Thesis. University of Oxford: United Kingdom.

Olley, J., Murray, A.S., Roberts, R.G. (1996). The effects of disequilibria in the uranium and thorium decay chains on burial dose rates in fluvial sediments. *Quaternary Science Reviews*, 15(7): 751-760.

Olley, J.M., Roberts, R.G., Murray, A.S. (1997). Disequilibria in the uranium decay series in sedimentary deposits at Allen's cave, Nullarbor Plain, Australia: Implications for dose rate determinations. *Radiation Measurements*, 27(2): 433-443.

Olley, J.M., Caitcheon, G.G., Roberts, R.G. (1999). The origin of dose distributions in fluvial sediments, and the prospect of dating single grains from fluvial deposits using optically stimulated luminescence. *Radiation Measurements*, 30: 207-217.

Olley, J.M., De Deckker, P., Roberts, R.G., Fifield, L.K., Yoshida, H., Hancock, G. (2004a). Optical dating of deep-sea sediments using single grains of quartz: a comparison with radiocarbon. *Sedimentary Geology*, 169: 175-189.

Olley, J.M., Pietsch, T., Roberts, R.G. (2004b). Optical dating of Holocene sediments from a variety of geomorphic settings using single grains of quartz. *Geomorphology*, 60: 337-358.

Olko, P., Czopyk, Ł., Kłosowski, M., Waligórski, M.P.R. (2008). Thermoluminescence dosimetry using TL-readers equipped with CCD cameras. *Radiation Measurements*, 43(2-6): 864-869.

Osborne, A.H., Vance, D., Rohling, E.J., Barton, N., Rogerson, M., Fello, N. (2008). A humid corridor across the Sahara for the migration of early modern humans out of Africa 120,000 years ago. *P. Natl. Acad. Sci. USA*, 105(43): 16444-16447.

Owen, L.A., Bright, J., Finkel, R.C., Jaiswal, M.K., Kaufman, D.S., Mahan, S., Radtke, U., Schneider, J.S., Sharp, W., Singhvi, A.K., Warren, C.N. (2007). Numerical dating of a Late Quaternary

spit-shoreline complex at the northern end of Silver Lake playa, Mojave Desert, California: A comparison of the applicability of radiocarbon, luminescence, terrestrial cosmogenic nuclide, electron spin resonance, U-series and amino acid racemization methods. *Quaternary International*, 166(1): 87-110.

Pericot, G.L. (1942). *La Cueva del Parpalló (Gandia)*. Madrid: Consejo Superior de Investigaciones Científicas.

Pfeifer, S.S., Krbetschek, M.R. (2009). Radioluminescence investigations on alumosilicates for age determination. Verhandlungen der Deutschen Physikalischen Gesellschaft. March 22-27. Dresden, Germany.

Pietsch, T.J., Olley, J.M., Nanson, G.C. (2008). Fluvial transport as a natural luminescence sensitiser of quartz. *Quaternary Geochronology*, 3(4): 365-376.

Polymeris, G.S., Afouxenidis, D., Tsirliganis, N.C., Kitis, G. (2009). The TL and room temperature OSL properties of the glow peak at 110˚C in natural milky quartz: A case study. *Radiation Measurements*, 44(1): 23-31.

Poolton, N.R.J., Bøtter-Jensen, Ypma, P.J.M., Johnsen, O. (1994). Influence of crystal structure on the optically stimulated luminescence propterties of feldspars. *Radiation Measurements*, 23(2-3): 551-554.

Prescott, J.R., Stephan, L.G. (1982). The contribution of cosmic radiation to the environmental dose for thermoluminescent dating: Latitude, altitude, and depth dependences. *PACT*, 6: 17-25.

Prescott, J.R., Hutton, J.T. (1988). Cosmic ray and gamma ray dosimetry for TL and ESR. *Nucl. Tracks Rad. Meas.*, 14(1-2): 223-227.

Prescott, J.R., Hutton, J.T. (1994). Cosmic ray contributions and ESR dating: Large depths and long-term time variations. *Radiation Measurements*, 23(2-3): 497-500.

Prescott, J.R., Williams, F.M., Hunt, C.D. (2007). Comparison of TL multiple aliquot, single grain GLSL SAR and C-14 ages for the Puritjarra, Australia, rock shelter. *Quaternary Geochronology*, 2(1-4): 344-349.

Preusser, F., Chithambo, M.L., Götte, T., Martini, M., Ramseyer, K., Sendezera, E.J., Susino, G.J., Wintle, A.G. (2009). Quartz as a natural luminescence dosimeter. *Earth-Science Reviews*, 97(1-4): 184-214.

Ramos, J., Bernal, D., Domínguez-Bella, S., Calado, D., Ruiz, B., Gil, M.J., Clemente, I., Durán, J.J., Vijande, E., Chamorro, S. (2008). The Benzú rockshelter: a Middle Palaeolithic site on the North African coast. *Quaternary Science Reviews*, 27(23-24): 2210-2218.

Raynal, J.-P. (1980). Taforalt. Mission Préhistorique et paléontologique française au Maroc: Rapport d'activité pour l'année. *Bulletin d'Archeologie Marocaine*, 12: 69-71.

Raynal, J.-P., Occhietti, S. (2012). Amino chronology and an earlier age for the Moroccan Aterian. In: Hublin, J.-J., McPherron, S.P. (Eds.), *Modern Origins: A North African Perspective*. Leipzig, Germany: Springer, pp. 79-90.

Raynal, J.-P., Lefèvre, D., Geraads, D., El Graoui, M. (1999). Contribution du site paléontologique de Lissasfa (Casablanca, Maroc) à une nouvelle interprétation du Mio-Pliocène de la Méseta. *C.R. Acad. Sci. II A*, 329: 617-622.

Raynal, J.-P., Alaoui, F.Z.S., Magoga, L., Mohib, A., Zouak, M. (2004). The Lower Palaeolithic sequence of Atlantic Morocco revisited after recent excavations at Casablanca. *Bulletin d'Archéologie Marocaine*, 20: 44-76.

Reimann, T., Lindhorst, S., Thomsen, K.J., Murray, A.S., Frechen, M. (2012). OSL dating of mixed coastal sediment (Sylt, German Bight, North Sea). *Quaternary Geochronology*, 11: 52-67.

Reimer, P.J., Baillie, M.G.L., Bard, E., Bayliss, A., Beck, J.W., Blackwell, P.G., Bronk Ramsey, C., Buck, C.E., Burr, G.S., Edwards, R.L., Friedrich, M., Grootes, P.M., Guilderson, T.P., Hajdas, I., Heaton, T.J., Hogg, A.G., Hughen, K.A., Kaiser, K.F., Kromer, B., McCormac, F.G., Manning, S.W., Reimer, R.W., Richards, D.A., Southon, J.R., Talamo, S., Turney, C.S.M., van der Plicht, J., Weyhenmeyer, C.E. (2009). INTCAL09 and MARINE09 radiocarbon age calibration curves, 0-50,000 years CAL BP. *Radiocarbon*, 51(4): 1111-1150.

Reygasse, M. (1921). *Nouvelles études de Palethnologie Maghrébine*. Constantine: Vve D. Braham.

Rhodes, E.J. (1990). *Optical dating of quartz*. D.Phil. Thesis. University of Oxford, United Kingdom.

Rhodes, E.J. (2011). Optically stimulated luminescence dating of sediments over the past 200,000 years. *Annu. Earth Planet. Sci. Rev.*, 39: 461-488.

Rhodes, E.J., Schwenninger, J.-L. (2007). Dose rates and radioisotope concentrations in the concrete calibration blocks at Oxford. *Ancient TL*, 25(1): 5-8.

Rhodes, E.J., Singarayer, J.S., Raynal, J.-P., Westaway, K.E., Sbihi-Alaoui, F.Z. (2006). New age estimates for the Palaeolithic assemblages and Pleistocene succession of Casablanca, Morocco. *Quaternary Science Reviews*, 25(19-20): 2569-2585.

Rhodes, E.J., Fanning, P.C., Holdaway, S.J. (2010). Developments in optically stimulated luminescence age control for geoarchaeological sediments and hearths in western New South Wales, Australia. *Quaternary Geochronology*, 5(2-3): 348-352.

Richter, D., Moser, J., Nami, M., Eiwanger, J., Mikdad, A. (2010). New chronometric data from Ifri n'Ammar (Morocco) and the chronostratigraphy of the Middle Palaeolithic in the Western Maghreb. *Journal of Human Evolution*, 59(6): 672-679.

Richter, D., Moser, J., Nami, M. (2012). New data from the site of Ifri n'Ammar (Morocco) and some remarks on the chronometric status of the Middle Paleolithic in the Maghreb. In: Hublin, J.-J., McPherron, S.P. (Eds.), *Modern Origins: A North African Perspective*. Leipzig, Germany: Springer, pp.61-78.

Risø DTU. (2008). Guide to the Risø TL / OSL reader. Roskilde, Denmark.

Risø DTU. (2009). Guide to the Risø single grain laser OSL system. Roskilde, Denmark.

Roberts, R.G., Galbraith, R.F., Olley, J.M., Yoshida, H., Laslett, G.M. (1999). Optical dating of single and multiple grains of quartz from Jinmium rock shelter, Northern Australia: Part II, Results and implications. *Archaeometry*, 41(2): 365-395.

Roberts, R.G., Galbraith, R.F., Yoshida, H., Laslett, G.M., Olley, J.M. (2000). Distinguishing dose populations in sediment mixtures: a test of single-grain optical dating procedures using mixtures of laboratory-dosed quartz. *Radiation Measurements*, 32: 459-465.

Robbins, M.S., Hadwen, B.J. (2003). The noise performance of electron multiplying charge-coupled devices. *IEEE Transactions on Electron Devices*, 50(5): 1227-1232.

Roche, J. (1953). La grotte de Taforalt. *Anthropologie*, 57: 375-380.

Roche, J. (1956). Etude sur l'industrie de la grotte de Dar-es-Soltane (Rabat). *Bulletin d'Archéologie Marocaine*, 1: 93-118.

Roche, J. (1963). *L'Épipaléolithique Marocain.* Lisbon: Fondation Calouste Gulbenkian.

Roche, J. (1967). L'Atérien de la grotte de Taforalt (Maroc oriental). *Bulletin d'Archéologie Marocaine*, 7: 11-56.

Roche, J. (1969). Les industries paléolithiques de la grotte de Taforalt (Maroc oriental). *Quaternaria*, 11: 89-100.

Roche, J. (1971). La grotte de Taforalt. *Bulletin de la Société d'histoire du Maroc*, 3: 7-14.

Roche, J. (1972). Les Industries paléolithiques de la Grotte de Taforalt (Maroc oriental). In: Hugo, H. (Ed.), *Actes du VIème Congrès panafricain de Préhistoire et de l'Etude du Quaternaire*, *Dakar 1967.* Chambéry: Les Imprimeries Réunies de Chambéry, pp. 102-108.

Roubet, F.-E. (1972). Recherches récentes sur la stratigraphie du littoral, a l'ouest d'Alger (L'Atérien et les formations de la cote, entre Bérard et Tipasa). In: Hugo, H. (Ed.), *Actes du VIème Congrès panafricain de Préhistoire et de l'Etude du Quaternaire*, *Dakar 1967.* Chambéry: Les Imprimeries Réunies de Chambéry, pp. 144-145.

Ruhlmann, A. (1936). *Les Grottes préhistoriques d' "El Khenzira" (Région de Mazagan): Contribution à l'étude du Paléolithique marocain (moyen et supérieur).* Ph.D. Thesis. Université Strasbourg: France.

Ruhlmann, A. (1951). *La grotte préhistorique de Dar es-Soltan*. Paris: Larose.

Scarciglia, F., Barca, D., De Rosa, R., Pulice, I. (2009) Application of laser ablation ICP-MS and traditional micromorphological techniques to the study of an Alfisol (Sardinia, Italy) in thin sections: Insights into trace element distribution. *Geoderma*, 152(1-2): 113-126.

Scerri, E.M.L. (2012). A new stone tool assemblage revisited: Reconsidering the "Aterian" in Arabia. In: Starkey, J.C.M. (Ed.), *Proceedings of the Seminar for Arabian Studies, July 2011.* London: Archaeopress.

Schiegl, S., Goldberg, P., Bar-Yosef, O., Weiner, S. (1996). Ash deposits in Hayonim and Kebara Caves, Israel: Macroscopic, microscopic and mineralogical observations, and their archaeological implications. *Journal of Archaeological Science*, 23(5): 763-781.

Schmidt, C., Rufer, D., Pettke, T., Preusser, F., Krbetschek, M., Dornich, K., Mittelstrass, D., Hilgers, A. (2010). Determining dose rate distribution patterns in siliceous rocks using LA-ICP-MS and spatially resolved luminescence measurements. UK TL/OSL/ESR Meeting 2010. September 8-10. Oxford, UK.

Schwenninger, J.-L., Collcutt, S.N., Barton, N., Bouzouggar, A., Clark-Balzan, L., El Hajraoui, M.A., Nespoulet, R., Débenath, A. (2010). A new luminescence chronology for Aterian cave sites on the Atlantic Coast of Morocco. In: Garcea, E.A.A. (Ed.), *South-eastern Mediterranean peoples between 130,000 and 10,000 years ago.* Oxford: Oxbow Books.

Shea, J.J. (2006). The origins of lithic projectile point technology: Evidence from Africa, the Levant, and Europe. *Journal of Archaeological Science*, 33(6): 823-846.

Shea, J.J. (2010). Neanderthals and early Homo sapiens in the Levant. In: Garcea, E.A.A. (Ed.), *South-Eastern Mediterranean Peoples between 130,000 and 10,000 years ago*. Oxford: Oxbow Books: 127-143.

Singarayer, J.S., Bailey, R.M., Ward, S., Stokes, S. (2005). Assessing the completeness of optical resetting of quartz OSL in the natural environment. *Radiation Measurements*, 40: 13-25.

Smith, E.W. (1935). Africa: What Do We Know of It? *J. R. Anthropol. Inst. G.*, 65: 1-81.

Smith, J.R., Giegengack, R., Schwarcz, H.P., McDonald, M.M.A., Kleindienst, M.R., Hawkins, A.L., Churcher, C.S. (2004). A reconstruction of Quaternary pluvial environments and human occupations using stratigraphy and geochronology of fossil-spring tufas, Kharga Oasis, Egypt. *Geoarchaeology*, 19(5): 407-439.

Smith, J.R., Hawkins, A.L., Asmerom, Y., Polyak, V., Giegengack, R. (2007). New age constraints on the Middle Stone Age occupations of Kharga Oasis, Western Desert, Egypt. *Journal of Human Evolution*, 52: 690-701.

Smith, T.M., Tafforeau, P., Reid, D., Grün, R., Eggins, S., Boutakiout, M., Hublin, J.-J. (2007). Earliest evidence of modern human life history in North African early Homo sapiens. *P. Natl. Acad. Sci. USA*, 104(15): 6128-6133.

Spooner, N A. (1994). On the optical dating signal from quartz. *Radiation Measurements*, 23(2-3): 593-600.

Spooner, N A. (2000). A photon-counting imaging system (PCIS) for luminescence applications. *Radiation Measurements*, 32: 513-521.

Stearns, C.E., Thurber, D.L. (1965). Th230/U234 dates of Late Pleistocene marine fossils from the Mediterranean and Moroccan littorals. *Quaternaria*, 7: 29-42.

Steele, T.E. (2012). Late Pleistocence human subsistence in Northern Africa: The state of our knowledge and placement in a continental context. In: Hublin, J.-J., McPherron, S.P. (Eds.), *Modern Origins: A North African Perspective*. Leipzig, Germany: Springer, pp. 107-125.

Stoetzel, E., Marion, L., Nespoulet, R., El Hajraoui, M.A., Denys, C. (2011). Taphonomy and palaeoecology of the late Pleistocene to middle Holocene small mammal succession of El Harhoura 2 cave (Rabat-Témara, Morocco). *Journal of Human Evolution*, 60(1): 1-33.

Stone, A.E.C., Bailey, R.M. (2012). The effect of single grain luminescence characteristics on single aliquot equivalent dose estimates. *Quaternary Geochronology*, 11: 68-78.

Stoneham, D., Stokes, S. (1991). An investiagion of the relationship between the 110°C TL peak and optically stimulated luminescence in sedimentary quartz. *Nucl. Tracks Rad. Meas.*, 18(1/2): 119-123.

Szabo, B., Haynes, C., Maxwell, T. (1995). Ages of Quaternary pluvial episodes determined by uranium-series and radiocarbon dating of lacustrine deposits of Eastern Sahara. *Palaeogeogr. Palaeocl.*, 113(2): 227-242.

Taylor, V.K., Barton, R.N.E., Bell, M., Bouzouggar, A., Collcutt, S., Black, S., Hogue, J.T. (2011). The Epipalaeolithic (Iberomaurusian) at Grotte des Pigeons (Taforalt), Morocco: A preliminary study of the land Mollusca. *Quaternary International*, 244(1): 5-14.

Teeuwisse, W., Geleijns, J., Veldkamp, W. (2007). An inter-hospital comparison of patient dose based on clinical indications. *European Radiology*, 17(7): 1795-1805.

Telfer, M.W., Bateman, M.D., Carr, A.S., Chase, B.M. (2008). Testing the applicability of a standardized growth curve (SGC) for quartz OSL dating: Kalahari dunes, South African coastal dunes and Florida dune cordons. *Quaternary Geochronology*, 3(1-2): 137-142.

Templer, R.H. (1986). Thermoluminescence techniques for dating zircon inclusions. D.Phil. Thesis. University of Oxford: United Kingdom.

Texier, J.-P., Huxtable, J., Rhodes, E., Miallier, D., Ousmoi, M. (1988). Nouvelles données sur la situation chronologique de l'Atérien du Maroc et leurs implications. *C.R. Acad. Sci. Paris.*, 307: 827-832.

Texier, J.-P., Lefévre, D., Raynal, J.-P., El Graoui, M. (2002). Lithostratigraphy of the littoral deposits of the last one million years in the Casablanca region (Morocco). *Quaternaire*, 13(1): 23-41.

Thomas, P.J., Nagabhushanam, P., Reddy, D.V. (2008). Optically stimulated luminescence dating of heated materials using single-aliquot regenerative–dose procedure: A feasibility study using archaeological artefacts from India. *Journal of Archaeological Science*, 35(3): 781-790.

Thomsen, K.J., Murray, A.S., Bøtter-Jensen, L. (2005). Sources of variability in OSL dose measurements using single grains of quartz. *Radiation Measurements*, 39(1): 47-61.

Thomsen, K.J., Murray, A.S., Bøtter-Jensen, L., Kinahan, J. (2007). Determination of burial dose in incompletely bleached fluvial samples using single grains of quartz. *Radiation Measurements*, 42(3): 370-379.

Thomsen, K.J., Murray, A., Jain, M. (2012). The dose dependency of the over-dispersion of quartz OSL single grain dose distributions. *Radiation Measurements*, 47(9): 732-739.

Tillet, T. (1985). The Palaeolithic and its environment in the northern part of the Chad basin. *The African Archaeological Review*, 3(1): 163-177.

Tribolo, C., Stokes, S. (2006). Underestimation of SAR equivalent doses for quartz from West Africa: A dose recovery study. *Radiation Measurements,* 41(7-8): 930-935.

Tribolo, C., Mercier, N., Douville, E., Joron, J.-L., Reyss, J.-L., Rufer, D., Cantin, N., Lefrais, Y., Miller, C.E., Porraz, G., Parkington, J., Rigaud, J.-P., Texier, P.-J. (2013). OSL and TL dating of the Middle Stone Age sequence at Diepkloof Rock Shelter (South Africa): A clarification. *Journal of Archaeological Science*, 40(9): 3401-3411.

Trinkaus, E. (2005). Early Modern Humans. *Annual Review of Anthropology*, 34: 207-230.

Trinkaus, E. (2007). European early modern humans and the fate of the Neandertals. *P. Natl. Acad. Sci. USA*, 104(18): 7367-7372.

Vandenberghe, D., Hossain, S.M., Corte, F.D. (2003). Investigations on the origin of the equivalent dose distribution in a Dutch coversand. *Geochronometria*, 37: 433 - 439.

Vandenberghe, D., De Corte, F., Buylaert, J.-P., Kučera, J., Van den haute, P. (2008). On the internal radioactivity in quartz. *Radiation Measurements*, 43(2-6): 771-775.

van Mourik, J.M., Nierop, K.G.J., Vandenberghe, D.A.G. (2010). Radiocarbon and optically stimulated luminescence dating based chronology of a polycyclic driftsand sequence at Weerterbergen (SE Netherlands). *Catena*, 80(3): 170-181.

van Peer, P. (1991). Interassemblage Variability and Levallois Styles: The Case of the Northern African Middle Palaeolithic. *Journal of Anthropological Archaeology*, 10: 107-151.

van Peer, P., Demidenko, Y.E., Garcea, E.A.A., Otte, M., Rolland, N., Ronen, A., Schild, R. (1998). The Nile corridor and the out-of-africa model: An examination of the archaeological record. *Current Anthropology*, 39(S1): S115-S140.

Vaufrey, R. (1955). *Prehistoire de l'Afrique*. Paris: Masson.

Veronese, I., Shved, V., Shishkina, E.A., Giussani, A., Göksu, H.Y. (2007). Study of dose rate profile at sample disks in a Risø OSL single-grain attachment system. *Radiation Measurements*, 42(2): 138-143.

Walton, A.J., Debenham, N.C. (1980). Spatial distribution studies of thermoluminescence using a high-gain image intensifier. *Nature*, 284: 42-44.

Walton, A.J., Debenham, N.C. (1982). Dating of paleolithic calcite by TL: observation of spatial inhomogeneity. PACT, 6: 202-208.

Weiner, S., Goldberg, P., Bar-Yosef, O. (2002). Three-dimensional distribution of minerals in the sediments of Hayonim Cave, Israel: Diagenetic processes and archaeological implications. *Journal of Archaeological Science*, 29(11): 1289-1308.

Wendorf, F., Schild, R. (1980). *Prehistory of the Eastern Sahara*. New York: Academic Press.

Wendorf, F., Close, A.E., Schild, R. (1987). Recent work on the Middle Palaeolithic of the Eastern Sahara. *The African Archaeological Review*, 5: 49-63.

Wengler, L. (1990). Économie des matières premières et territoire dans le Moustérien et l'Atérien maghrébins exemples du Maroc Oriental. *L'Anthropologie*, 94(2): 335-360.

Wengler, L. (1993). Relations entre le milieu naturel et les modifications culturelles au Paléolithique moyen, le cas des Monts d Oujda (Maroc oriental). *B. Mém. Soc. Anthro. Par.*, 5(3-4): 355-378.

Wengler, L. (1997). La transition du Moustérien à l'Atérien. *L'Anthropologie*, 101: 448-481.

Williams, M. A. J. (1976). Upper Quaternary stratigraphy of Adrar Bous, Republic of Niger, south central Sahara. In: Abebe, B., Chavaillon, J., Sutton, J.E.G. (Eds.), *Actes du Congrès panafricain de préhistoire et des études du quaternaire, Addis Ababa 1971*. Addis Ababa: Provisional Military Government of Socialist Ethiopia, Ministry of Culture, pp. 435-441.

Wintle, A.G. (1973). Anomalous fading of thermo-luminescence in mineral samples. *Nature*, 245: 143-144.

Wintle, A.G., Aitken, M.J. (1977). Thermoluminescence dating of burnt flint: Application to a Lower Palaeolithic site, Terra Amata. *Archaeometry*, 19(2): 111-130.

Wintle, A.G., Huntley, D.J. (1979). Thermoluminescence dating of a deep-sea sediment core. *Nature*, 279: 710-712.

Wintle, A.G., Huntley, D.J. (1980). Thermoluminescence dating of ocean sediments. Can. J.Earth Sci. 17(3): 348-360.

Woda, C., Fuchs, M. (2008). On the applicability of the leading edge method to obtain equivalent doses in OSL dating and dosimetry. *Radiation Measurements*, 43(1): 26-37.

Wrinn, P.J., Rink, W.J. (2003). ESR Dating of Tooth Enamel From Aterian Levels at Mugharet el 'Aliya (Tangier, Morocco). *Journal of Archaeological Science*, 30(1): 123-133.

Yoshida, H., Roberts, R.G., Olley, J.M., Laslett, G.M., Galbraith, R.F. (2000). Extending the age range of optical dating using single 'supergrains' of quartz. *Radiation Measurements*, 32(5-6): 439-446.

Zacharias, N., Schwedt, A., Buxeda i Garrigós, J., Michael, C.T., Mommsen, H., Kilikoglou, V. (2007). A contribution to the study of post-depositional alterations of pottery using TL dating analysis. *Journal of Archaeological Science*, 34: 1804-1809.

Zander, A., Degering, D., Preusser, F., Kasper, H.U., Bruckner, H. (2007). Optically stimulated luminescence dating of sublittoral and intertidal sediments from Dubai, UAE: Radioactive disequilibria in the uranium decay series. *Quaternary Geochronology*, 2(1-4): 123-128.

Zielinski, R.A., Asher-Bolinder, S., Meier, A.L., Johnson, C.A., Szabo, B.J. (1997). Natural or fertilizer-derived uranium in irrigation drainage: a case study in southeastern Colorado, U.S.A. *Applied Geochemistry*, 12(1): 9-21.

Zimmerman, D.W. (1967). Thermoluminescence from fine grains from ancient pottery. *Archaeometry*, 10(1): 26-28.

Zimmerman, D.W. (1971). Thermoluminescent dating using fine grains from pottery. *Archaeometry*, 13(1): 29-52.

Appendix A: MATLAB equivalent dose analysis code

This appendix provides the MATLAB code written for automated equivalent dose analysis (multigrain and single grain) by the author. Three scripts are presented in the order they are described here, separated by solid black lines and headed with a descriptive title in bold text (not part of the code). Text prefaced with a (%) indicates code commentary. The first section is a script that reads and stores luminescence measurements and run parameters from each selected '.bin' file. Once each '.bin' file has been stored, this code calls the function 'minimal_calc_rejection,' which calculates rejection criteria for each grain or aliquot and then fits the data. Curve fitting is performed by calling the function 'fit_curve_no_gui,' which returns the fitted data and weighted residuals as outputs.

Data Input and Storage

```
%select files to analyse
[FileName,PathName,FilterIndex] = uigetfile( 'C:\...\Bin files for matlab\*.*', 'MultiSelect', 'on');
num_files=size(FileName);

for q=1:num_files(2)
   sg_start_signal=6;
   sg_end_signal=8;
   sg_start_bg=45;
   sg_end_bg=55;
   mg_start_signal=1;
   mg_end_signal=2;
   mg_start_bg=225;
   mg_end_bg= 250;
   osl_cycle_counter=zeros(50, 1);
   ir_cycle_counter=zeros(50, 1);
   sar_type=0;
   OSL_data=struct('position', struct('grain', struct('cycle', struct('timeseries', [], 'signal', [], 'error', []))));
   IR_data=struct('position', struct('grain', struct('cycle', struct('timeseries', [], 'signal', [], 'error', []))));
   all_dose_matrix=struct('position', struct('dose',[]));
   dose_matrix=struct('position', struct('dose',[]));
   fid=fopen(strcat(PathName, FileName{q}));
   %get size of file in bytes
   fseek(fid, 0, 'eof');
   filesize = ftell(fid);
   %read in OSL record information
   fseek(fid, 0, 'bof');
   current=1;
   while current<filesize
```

```
      fseek(fid, 2, 'cof');
      this_length=fread(fid, 1, 'int16');
      prev_length=fread(fid, 1, 'int16');
      npoints=fread(fid, 1, 'int16');
      ltype=fread(fid, 1, 'int8');
      hh=waitbar(current/filesize)
      if ltype==6   %continue reading to get info and put into array but also add info into sg pos var matrix
        sar_type=1;
        fseek(fid, 24, 'cof');
        pos=fread(fid, 1, 'int8');
        fseek(fid, 34, 'cof');
        irrad_time=fread(fid, 1, 'single');
        fseek(fid, 1, 'cof');
        irrad_unit=fread(fid, 1, 'int8');
        fseek(fid, 136, 'cof');
        grain_no=fread(fid, 1, 'int16');
        if grain_no==1
          %cycle counter plus one for this pos
          osl_cycle_counter(pos, 1)=osl_cycle_counter(pos, 1)+1;
          all_dose_matrix.position(pos).dose(osl_cycle_counter(pos,1))=irrad_time;
        end
        %read osl info for this run, set, grain
        fseek(fid, 60, 'cof');
        if npoints==0
          timeseries=ones(60,1);
          signal=0;
          background=0;
          osl_cycle_counter(pos,1)=0;
        else
          timeseries=[];
          timeseries=fread(fid, npoints, 'int32');
          %enter info into structure array
          signal=sum(timeseries(sg_start_signal:sg_end_signal));
          %background is average over integ. limits times number signal channels
          background=(sg_end_signal-sg_start_signal +1)*mean(timeseries(sg_start_bg:sg_end_bg));
          OSL_data.position(pos).grain(grain_no).cycle(osl_cycle_counter(pos, 1)).timeseries=timeseries;
          OSL_data.position(pos).grain(grain_no).cycle(osl_cycle_counter(pos, 1)).signal=signal-
background;
          if signal-background==0
            OSL_data.position(pos).grain(grain_no).cycle(osl_cycle_counter(pos, 1)).error=0;
          else OSL_data.position(pos).grain(grain_no).cycle(osl_cycle_counter(pos,
1)).error=((signal+background/2)/(signal-background))^.5;
          end
        end
      elseif ltype==1
        timeseries=zeros(250,1);
        fseek(fid, 24, 'cof');
        pos=fread(fid, 1, 'int8');
        fseek(fid, 34, 'cof');
        irrad_time=fread(fid, 1, 'single');
        fseek(fid, 1, 'cof');
        irrad_unit=fread(fid, 1, 'int8');
        fseek(fid, 133, 'cof');
        light_source=fread(fid, 1, 'int8');
        fseek(fid, 2, 'cof');
        grain_no=fread(fid, 1, 'int16');
        grain_no=1;
```

```
        if light_source==1||light_source==4
           sar_type=2;
           osl_cycle_counter(pos, 1)=osl_cycle_counter(pos, 1)+1;
           all_dose_matrix.position(pos).dose(osl_cycle_counter(pos,1))=irrad_time;
           fseek(fid, 60, 'cof');
           timeseries=fread(fid, npoints, 'int32');
           signal=sum(timeseries(mg_start_signal:mg_end_signal));
           background=(mg_end_signal-mg_start_signal +1)*mean(timeseries(mg_start_bg:mg_end_bg));
           OSL_data.position(pos).grain(grain_no).cycle(osl_cycle_counter(pos, 1)).timeseries=timeseries;
           OSL_data.position(pos).grain(grain_no).cycle(osl_cycle_counter(pos, 1)).signal=signal-
background;
           if signal-background==0
              OSL_data.position(pos).grain(grain_no).cycle(osl_cycle_counter(pos, 1)).error=0;
           else OSL_data.position(pos).grain(grain_no).cycle(osl_cycle_counter(pos,
1)).error=((signal+background/2)/(signal-background))^.5;
           end
        elseif light_source==2
           timeseries=zeros(250,1);

           ir_cycle_counter(pos, 1)=ir_cycle_counter(pos, 1)+1;
           fseek(fid, 60, 'cof');
           timeseries=fread(fid, npoints, 'int32');
           signal=sum(timeseries(mg_start_signal:mg_end_signal));  %total signal sum over channels
           background=(mg_end_signal-mg_start_signal +1)*mean(timeseries(mg_start_bg:mg_end_bg));
%mean over bg channels mult by number signal channels
           IR_data.position(pos).grain(grain_no).cycle(ir_cycle_counter(pos, 1)).timeseries=timeseries;
           IR_data.position(pos).grain(grain_no).cycle(ir_cycle_counter(pos, 1)).signal=signal-background;
           if signal-background==0
              IR_data.position(pos).grain(grain_no).cycle(ir_cycle_counter(pos, 1)).error=0;
           else IR_data.position(pos).grain(grain_no).cycle(ir_cycle_counter(pos,
1)).error=((signal+background/2)/(signal-background))^.5;
           end
        end
        hh=waitbar(current/filesize);
     elseif ltype==2
        timeseries=zeros(250,1);
        sar_type=2;
        fseek(fid, 24, 'cof');
        pos=fread(fid, 1, 'int8');
        fseek(fid, 34, 'cof');
        irrad_time=fread(fid, 1, 'single');
        fseek(fid, 1, 'cof');
        irrad_unit=fread(fid, 1, 'int8');
        fseek(fid, 136, 'cof');
        grain_no=fread(fid, 1, 'int16');
        grain_no=1;
        ir_cycle_counter(pos, 1)=ir_cycle_counter(pos, 1)+1;
        fseek(fid, 60, 'cof');
        timeseries=fread(fid, npoints, 'int32');
        signal=sum(timeseries(mg_start_signal:mg_end_signal));  %total signal sum over channels
        background=(mg_end_signal-mg_start_signal +1)*mean(timeseries(mg_start_bg:mg_end_bg));
        IR_data.position(pos).grain(grain_no).cycle(ir_cycle_counter(pos, 1)).timeseries=timeseries;
        IR_data.position(pos).grain(grain_no).cycle(ir_cycle_counter(pos, 1)).signal=signal-background;
        if signal-background==0
           IR_data.position(pos).grain(grain_no).cycle(ir_cycle_counter(pos, 1)).error=0;
        else IR_data.position(pos).grain(grain_no).cycle(ir_cycle_counter(pos,
1)).error=((signal+background/2)/(signal-background))^.5;
```

```
        end
        hh=waitbar(current/filesize);
    else fseek(fid, this_length-9, 'cof');
    end
    current = ftell(fid);
  end
  k=1;
  max=1;
  while osl_cycle_counter(k,1)==0
    k=k+1;
  end
  pos_size=size(all_dose_matrix.position);
  for i=1:pos_size(2)
    no_doses=size(all_dose_matrix.position(i).dose);
    for j=1:(no_doses(2)/2-1)
      dose_matrix.position(i).dose(j)=all_dose_matrix.position(i).dose(2*j+1);
    end
  end
  close(hh)
  grain_no=1;
  current_pos = 1;
  rr_lim=10;
  zero_lim=5;
  tx_err=20;
  de_err=20;
  fit_type= 1;
  mc=0;
  monte_rounds=2000;
  stable=0;
  meas_error=2;
  if sar_type==1
    signal_start=sg_start_signal;
    signal_end=sg_end_signal;
    bg_start=sg_start_bg;
    bg_end=sg_end_bg;
  else
    signal_start=mg_start_signal;
    signal_end=mg_end_signal;
    bg_start=mg_start_bg;
    bg_end=mg_end_bg;
  end
  current_file=FileName{q};
  [auto_fit_eq,rejection_values, accepted_grains,
report]=minimal_calc_rejection(current_file,dose_matrix, osl_cycle_counter, ir_cycle_counter, sar_type,
OSL_data,IR_data,  signal_start, signal_end, bg_start,bg_end, meas_error, zero_lim, rr_lim, tx_err,
current_pos, monte_rounds, mc, stable);
save( strcat('C:\Documents and Settings\Laine\Desktop\', Names{q}, '.mat'), 'report');
  fclose('all')
end
clear all  %clear workspace
```

Rejection Criteria and Equivalent dose Calculation

```
function [auto_fit_eq,rejection_values, accepted_grains, report]=minimal_calc_rejection(current_file,
dose_matrix, osl_cycle_counter, ir_cycle_counter, sar_type, OSL_data,IR_data,  signal_start, signal_end,
bg_start,bg_end, meas_error, zero_lim, rr_lim, tx_err, current_pos, monte_rounds, mc, stable)
%record recycling ratio value and error and zero value and err
%record if pass (0) or not pass (1) in pass for 0, rr, tx, sigma
rejection_values=struct('position', struct('grain', struct('values', [], 'zero_pass', [], 'rr_pass', [], 'tx_pass', [],
'sigma_pass', [], 'ir_sigma_pass', [] )));
report=[];
report=struct('total_data', struct('osl_data', [], 'ir_data', [], 'osl_cycle_counter', [], 'ir_cycle_counter', [],
'dose_matrix', []), 'position', struct('grain', struct('params', struct('signal_lim', [], 'bg_lim', [], 'meas_error',
[], 'mc_repeats', []), 'rej_criteria', struct('r_ratio', [], 'zero_ratio', [], 'tx_err', [], 'sigma', [], 'ir_sigma', []),
'growth_data', struct('y_points', [], 'y_error', [], 'doses', [], 'nat_y', [], 'nat_error', [], 'raw_data', []),
'auto_fit', struct('weighted_resid', [], 'chosen_fit', [], 'central_De', [], 'chosen_fit_params', [], 'monte_info',
struct('monte_nat', [], 'monte_growth', [], 'monte_fit_params', [], 'De', [], 'all_fit_De', [], 'std_De_err', [],
'fail_counter', [])))));
accepted_grains=[0];
report.total_data.osl_data=OSL_data;
report.total_data.ir_data=IR_data;
report.total_data.osl_cycle_counter=osl_cycle_counter;
report.total_data.ir_cycle_counter=ir_cycle_counter;
report.total_data.dose_matrix=dose_matrix;
index=1;
p=1;
 all_grain_rejection=zeros(100, 4);
for pos=1:50
   doses=[];
   sorted_doses=[];
   combined_matrix=[];
   monte_growth=[];
   De=[];
   y_points=[];
   y_error=[];
   params=[];
   params2=[];
   estimates=[];
   if osl_cycle_counter(pos, 1)>0
      doses=dose_matrix.position(pos).dose;
      if sar_type==1
         for grain=1:100
            report.position(pos).grain(grain).params.signal_lim=[signal_start signal_end];
            report.position(pos).grain(grain).params.bg_lim=[bg_start bg_end];
            report.position(pos).grain(grain).params.meas_error=meas_error;
            report.position(pos).grain(grain).params.mc_repeats=monte_rounds;
            report.position(pos).grain(grain).rej_criteria.zero_ratio(1)=zero_lim;
            report.position(pos).grain(grain).rej_criteria.r_ratio(1)=rr_lim;
            report.position(pos).grain(grain).rej_criteria.tx_err(1)=tx_err;
            %calculate Lx, Tx and errors over user defined integration
            %limits
            current_pos=pos;
            grain_no=grain;
            %error includes meas_error added in quad
            [y_points, y_error, nat_x, nat_y, nat_error, signal, background, all_y_points,
nat_tx_error]=get_y_points( dose_matrix, osl_cycle_counter, ir_cycle_counter, sar_type, current_pos,
OSL_data, IR_data, grain_no, signal_start, signal_end, bg_start,bg_end, meas_error)
```

```
            report.position(pos).grain(grain).growth_data.y_points=y_points;
            report.position(pos).grain(grain).growth_data.y_error=y_error;
            report.position(pos).grain(grain).growth_data.doses=doses;
            report.position(pos).grain(grain).growth_data.nat_y=nat_y;
            report.position(pos).grain(grain).growth_data.nat_error=nat_error;
            report.position(pos).grain(grain).growth_data.raw_data(1,:)=all_y_points(:);
            report.position(pos).grain(grain).growth_data.raw_data(2,:)=signal(:);
            report.position(pos).grain(grain).growth_data.raw_data(3,:)=background(:);
            combined_matrix=[];
            combined_matrix(1,:)=doses(1,:);
            combined_matrix(2,:)=y_points(1,:);
            combined_matrix(3,:)=y_error(1,:);
            %sort matrix by first row (doses), ascending
            combined_matrix=combined_matrix';
            combined_matrix=sortrows(combined_matrix, 1);
            sorted_doses=combined_matrix';
            %calc zero ratio
            %if disc has 0 dose then calc zero-ratio
            if sorted_doses(1, 1)==0
               if nat_y==0
                  zero_ratio=1;
               else zero_ratio=sorted_doses(2,1)/nat_y;
               end
               if sorted_doses(2,1)==0 || nat_y==0
                  zero_ratio_err=0;
               else
zero_ratio_err=zero_ratio*((sorted_doses(3,1)/sorted_doses(2,1))^2+(nat_error/nat_y)^2)^.5;
               end
               if abs(zero_ratio)<=(zero_lim/100)|| [((zero_ratio+2*zero_ratio_err)>0) &&((zero_ratio-
2*zero_ratio_err)<0)]
                  %if abs(zero_ratio)<=(zero_lim/100)
                  zero_pass=0; %0 means passes
               else zero_pass=1;
               end
               report.position(pos).grain(grain).rej_criteria.zero_ratio(2)=zero_pass;
               report.position(pos).grain(grain).rej_criteria.zero_ratio(3)=zero_ratio;
               report.position(pos).grain(grain).rej_criteria.zero_ratio(4)=zero_ratio_err;
               has_rej_values(1,1)=1; %has zero ratio value
               has_rej_values(2,1)=zero_pass;
            else has_rej_values(1,1)=0; %has no zero dose
               has_rej_values(2,1)=0;
               report.position(pos).grain(grain).rej_criteria.zero_ratio(2)=-1;
            end
            %calc r-ratio if available
            [b1, m1, n1] = unique(sorted_doses(1,:), 'first');
            [b2, m2, n2] = unique(sorted_doses(1,:), 'last');
            [c,indices]=setdiff(m1,m2);
            if isempty(c)==0 % if there is a repeat dose
               repeat_dose=sorted_doses(1,m1(indices(1)));  %use first one only
               first_y=sorted_doses(2,m1(indices(1)));
               first_y_err=sorted_doses(3,m1(indices(1)));
               second_y=sorted_doses(2,m2(indices(1)));
               second_y_err=sorted_doses(3,m2(indices(1)));
               if first_y==0
                  r_ratio=0;
               else r_ratio=second_y/first_y;
               end
```

```
            if first_y==0 || second_y==0
               r_ratio_err=0;
            else r_ratio_err=r_ratio*((first_y_err/first_y)^2+(second_y_err/second_y)^2)^.5;
            end
            if abs(r_ratio-1)<=(rr_lim/100)|| [((r_ratio+2*r_ratio_err)>1) &&((r_ratio-2*r_ratio_err)<1)]
               %if abs(r_ratio-1)<=(rr_lim/100)
               rr_pass=0; %it passes
            else rr_pass=1;
            end
            report.position(pos).grain(grain).rej_criteria.r_ratio(2)=rr_pass;
            report.position(pos).grain(grain).rej_criteria.r_ratio(3)=r_ratio;
            report.position(pos).grain(grain).rej_criteria.r_ratio(4)=r_ratio_err;
            has_rej_values(1,2)=1;
            has_rej_values(2,2)=rr_pass;
         else has_rej_values(1,2)=0;  %no rejection value
            has_rej_values(2,2)=0;
            report.position(pos).grain(grain).rej_criteria.r_ratio(2)=-1;
         end
         %compare tx error % for first test dose (after natural)
         if (nat_tx_error/all_y_points(2))>(tx_err/100)
            tx_pass=1;  %fails
         else tx_pass=0;    %passes
         end
         report.position(pos).grain(grain).rej_criteria.tx_err(2)=tx_pass;
         report.position(pos).grain(grain).rej_criteria.tx_err(3)=nat_tx_error;
         %rejection_values.position(pos).grain(grain).tx_pass=tx_pass;
         %check signal >3 sigma ABOVE bg
         std_dev=std(OSL_data.position(pos).grain(grain).cycle(1).timeseries(bg_start:bg_end));
         %all_y_points is difference of signal and avg background*signal
         %integ channels
         if (all_y_points(1)/(signal_end-signal_start +1))<(3*std_dev)
            sigma_pass=1; %fails
         else sigma_pass=0;
         end
         %rejection_values.position(pos).grain(grain).sigma_pass=sigma_pass;
         report.position(pos).grain(grain).rej_criteria.sigma=sigma_pass;
         %if pass tx err and sigma then fit
         if tx_pass==0 && sigma_pass==0
            accepted_grains(index, 1)=pos;
            accepted_grains(index, 2)=grain;
            %now fit grain
            chi_array=cell(3,3);
            fit_type=1;
            [x_data, y_data, De, De_error, monte_results, weighted_resid, exit_flag,
fit_params]=fit_curve_no_gui(monte_rounds, mc, stable, fit_type, nat_y, nat_x, y_error, dose_matrix,
y_points, nat_error, osl_cycle_counter, ir_cycle_counter, current_pos)
            chi_array(1,1)={weighted_resid};
            chi_array(2,1)={De};
            chi_array(3,1)={fit_params};
            report.position(pos).grain(grain).auto_fit.weighted_resid=[];              %
            fit_type=2;
            [x_data, y_data, De, De_error, monte_results, weighted_resid, exit_flag,
fit_params]=fit_curve_no_gui(monte_rounds, mc, stable, fit_type, nat_y, nat_x, y_error, dose_matrix,
y_points, nat_error, osl_cycle_counter, ir_cycle_counter, current_pos)
            chi_array(1,2)={weighted_resid};
            chi_array(2,2)={De};
            chi_array(3,2)={fit_params};
```

```
            report.position(pos).grain(grain).auto_fit.weighted_resid(2)=weighted_resid;
            fit_type=3;
            [x_data, y_data, De, De_error, monte_results, weighted_resid, exit_flag,
fit_params]=fit_curve_no_gui(monte_rounds, mc, stable, fit_type, nat_y, nat_x, y_error, dose_matrix,
y_points, nat_error, osl_cycle_counter, ir_cycle_counter, current_pos)
            chi_array(2,3)={De};
            chi_array(1,3)={weighted_resid};
            chi_array(3,3)={fit_params};
            report.position(pos).grain(grain).auto_fit.weighted_resid(3)=weighted_resid;
            %need progress bar
            index=index+1;
            %choose which fit type to use
            for array_val=1:3
              if isfinite(chi_array{1, array_val})==1
                chi_matrix(array_val)=chi_array{1, array_val};
              else chi_matrix(array_val)=Inf;
              end
            end
            [min_val, chosen_fit]=min(chi_matrix(1,:));
            report.position(pos).grain(grain).auto_fit.chosen_fit=chosen_fit;
            report.position(pos).grain(grain).auto_fit.central_De=chi_array{2,chosen_fit};
            report.position(pos).grain(grain).auto_fit.chosen_fit_params=chi_array{3,chosen_fit};
            %%%%%%%%%%%%getmonte carlo De error
            %choose points
            monte_rounds=2000;
            fail_counter=0; %use m as index
            accept=1;
            h = waitbar(0,horzcat(current_file, ' Disc ', num2str(pos), ' Grain ', num2str(grain)));
            De=[];
            for i=1:monte_rounds
              monte_nat=nat_y + nat_error*randn(1);
              auto_fit_eq.position(pos).grain(grain_no).monte_nat(i)=monte_nat;
              report.position(pos).grain(grain).auto_fit.monte_info.monte_nat(i)=monte_nat;
              for j=1:length(y_points)
                monte_growth(j)=y_points(j) + y_error(j)*randn(1);
              end
              report.position(pos).grain(grain).auto_fit.monte_info.monte_growth(i, :)=monte_growth;
              if chosen_fit==1  %fit exponential
                options=optimset('Algorithm', 'levenberg-marquardt');
                start_point = [4 0.01 0];
                estimates=[];
                [estimates,resnorm,residual,exitflag] = lsqcurvefit(@(params, doses) params(1) -
params(1)* exp(-doses*params(2))+params(3), start_point, doses, monte_growth, [], [], options )
                if exitflag>=0 && monte_nat>= (estimates(1)+estimates(3)) %fit converges but De never
intersects (don't need to worry about sigma here)
                  De(accept, 1)=Inf; %to signify sat
                  accept=accept+1;
                  report.position(pos).grain(grain).auto_fit.monte_info.monte_fit_params(i,:)=estimates;
                  report.position(pos).grain(grain).auto_fit.monte_info.De(i,1)=1;
                  report.position(pos).grain(grain).auto_fit.monte_info.De(i,2)=0;
                  report.position(pos).grain(grain).auto_fit.monte_info.De(i,3)=Inf;
                  report.position(pos).grain(grain).auto_fit.monte_info.De(i,4)=-(1/estimates(2))*log((-
(.95*(estimates(1)+estimates(3)))+estimates(1)+estimates(3))/estimates(1)); %after which point within
95% of infinite response
                elseif exitflag<0 %fitting does not converge or terminated;
                  fail_counter=fail_counter+1;
                  report.position(pos).grain(grain).auto_fit.monte_info.monte_fit_params(i,:)=[Inf Inf Inf];
```

```
                    report.position(pos).grain(grain).auto_fit.monte_info.De(i,1)=-1;
                    report.position(pos).grain(grain).auto_fit.monte_info.De(i,2)=1;
                    report.position(pos).grain(grain).auto_fit.monte_info.De(i,3)=-(10^30);
                    report.position(pos).grain(grain).auto_fit.monte_info.De(i,4)=0;
                  else De_temp=-(1/estimates(2))*log((-
monte_nat+estimates(1)+estimates(3))/estimates(1));
                    De(accept, 1)=De_temp;
                    accept=accept+1;
                    report.position(pos).grain(grain).auto_fit.monte_info.monte_fit_params(i,:)=estimates;
                    report.position(pos).grain(grain).auto_fit.monte_info.De(i,1)=0;
                    report.position(pos).grain(grain).auto_fit.monte_info.De(i,2)=0;
                    report.position(pos).grain(grain).auto_fit.monte_info.De(i,3)=De_temp;
                    report.position(pos).grain(grain).auto_fit.monte_info.De(i,4)=0;
                  end
                elseif chosen_fit==2
                  estimates=[];
                  %fit lin to two highest dose points first then exp +lin with
                  %start points from lin fitting
                  %what if intersects in two places? then finds first
                  %intersection
                  for temp_index=1:length(doses)
                    combined_matrix(1,temp_index)=doses(1,temp_index);
                    combined_matrix(2,temp_index)=monte_growth(1,temp_index);
                  end
                  %sort matrix by first row (doses), ascending
                  combined_matrix=combined_matrix';
                  combined_matrix=sortrows(combined_matrix);
                  sorted_doses=combined_matrix';
                  size_sorted=size(sorted_doses);
                  lin_fit_x(1)=sorted_doses(1,size_sorted(2));
                  lin_fit_x(2)=sorted_doses(1,size_sorted(2)-1);
                  lin_fit_y(1)=sorted_doses(2,size_sorted(2));
                  lin_fit_y(2)=sorted_doses(2,size_sorted(2)-1);
                  %find good start point
                  start_slope=(lin_fit_y(2)-lin_fit_y(1))/(lin_fit_x(2)-lin_fit_x(1));
                  start_inter=(lin_fit_y(1)+lin_fit_y(2)-start_slope*(lin_fit_x(1)+lin_fit_x(2)))/2;
                  start_point2 = [4 0.01 0];
                  sse = @(params2)sum((((params2(1) -params2(1)* exp(-doses*params2(2))+params2(3))-
monte_growth).^2));
                  [estimates2, fval2, exitflag2] = fminsearch(sse, start_point2);
                  %fit exp+lin
                  start_point = [estimates2(1) estimates2(2) start_slope 0];
                  options=optimset('Algorithm', 'levenberg-marquardt');
                  [estimates,resnorm,residual,exitflag] = lsqcurvefit(@(params, doses) params(1) -
params(1)* exp(-doses*params(2))+params(3)*doses+params(4), start_point, doses, monte_growth, [], [],
options )
                  exit_flag=exitflag;
                  if exit_flag>=0
                    if estimates(3)>0 %fit curve does not sat
                      [De_temp, fval, exitflag]=fzero(@(x) estimates(1)-estimates(1)*exp(-
x*estimates(2))+estimates(3)*x+estimates(4)-monte_nat, 0);
                      if exitflag<0 %fitting does not converge or terminated
                        fail_counter=fail_counter+1;
                        report.position(pos).grain(grain).auto_fit.monte_info.monte_fit_params(i,:)=[Inf Inf
Inf Inf];
                        report.position(pos).grain(grain).auto_fit.monte_info.De(i,1)=0;
                        report.position(pos).grain(grain).auto_fit.monte_info.De(i,2)=1;
```

```
                        report.position(pos).grain(grain).auto_fit.monte_info.De(i,3)=-(10^30);
                        report.position(pos).grain(grain).auto_fit.monte_info.De(i,4)=0;
                      else De(accept, 1)=De_temp;
                        accept=accept+1;
report.position(pos).grain(grain).auto_fit.monte_info.monte_fit_params(i,:)=estimates;
                        report.position(pos).grain(grain).auto_fit.monte_info.De(i,1)=0;
                        report.position(pos).grain(grain).auto_fit.monte_info.De(i,2)=0;
                        report.position(pos).grain(grain).auto_fit.monte_info.De(i,3)=De_temp;
                        report.position(pos).grain(grain).auto_fit.monte_info.De(i,4)=0;
                      end
                    elseif estimates(3)<0 %then the fit curve will have a max value
                      max_x=(-1/estimates(2))*(log(-estimates(3)/(estimates(2)*estimates(1))));
                      max_y=estimates(1)-estimates(1)*exp(-
estimates(2)*max_x)+estimates(3)*max_x+estimates(4);
                      if monte_nat>=max_y
                        De(accept, 1)=Inf;
                        accept=accept+1;
report.position(pos).grain(grain).auto_fit.monte_info.monte_fit_params(i,:)=estimates;
                        report.position(pos).grain(grain).auto_fit.monte_info.De(i,1)=1;
                        report.position(pos).grain(grain).auto_fit.monte_info.De(i,2)=0;
                        report.position(pos).grain(grain).auto_fit.monte_info.De(i,3)=Inf;
                        report.position(pos).grain(grain).auto_fit.monte_info.De(i,4)=max_x;
                      else [De_temp, fval, exitflag]=fzero(@(x) estimates(1)-estimates(1)*exp(-
x*estimates(2))+estimates(3)*x+estimates(4)-monte_nat, 0);
                        if exitflag<0 %fitting does not converge or terminated
                          fail_counter=fail_counter+1;
                          report.position(pos).grain(grain).auto_fit.monte_info.monte_fit_params(i,:)=[Inf
Inf Inf Inf];
                          report.position(pos).grain(grain).auto_fit.monte_info.De(i,1)=0;
                          report.position(pos).grain(grain).auto_fit.monte_info.De(i,2)=1;
                          report.position(pos).grain(grain).auto_fit.monte_info.De(i,3)=-(10^30);
                          report.position(pos).grain(grain).auto_fit.monte_info.De(i,4)=0;
                        else De(accept, 1)=De_temp;
                          accept=accept+1;
report.position(pos).grain(grain).auto_fit.monte_info.monte_fit_params(i,:)=estimates;
                          report.position(pos).grain(grain).auto_fit.monte_info.De(i,1)=0;
                          report.position(pos).grain(grain).auto_fit.monte_info.De(i,2)=0;
                          report.position(pos).grain(grain).auto_fit.monte_info.De(i,3)=De_temp;
                          report.position(pos).grain(grain).auto_fit.monte_info.De(i,4)=0;
                        end
                      end
                    end
                  else  %fitting does not converge or terminated; no De recorded in list
                    fail_counter=fail_counter+1;
                    report.position(pos).grain(grain).auto_fit.monte_info.monte_fit_params(i,:)=[Inf Inf Inf
Inf];
                    report.position(pos).grain(grain).auto_fit.monte_info.De(i,1)=-1;
                    report.position(pos).grain(grain).auto_fit.monte_info.De(i,2)=1;
                    report.position(pos).grain(grain).auto_fit.monte_info.De(i,3)=-(10^30);
                    report.position(pos).grain(grain).auto_fit.monte_info.De(i,4)=0;
                  end
                elseif chosen_fit==3
                  start_point = [0.05 0.005];
                  sse = @(params)sum((((params(1) +params(2)* doses)-monte_growth).^2));
                  estimates = fminsearch(sse, start_point);
                  De(accept, 1)=(monte_nat-estimates(1))/estimates(2);
                  accept=accept+1;
```

```
                report.position(pos).grain(grain).auto_fit.monte_info.monte_fit_params(i,:)=estimates;
                report.position(pos).grain(grain).auto_fit.monte_info.De(i,1)=0;
                report.position(pos).grain(grain).auto_fit.monte_info.De(i,2)=0;
                report.position(pos).grain(grain).auto_fit.monte_info.De(i,3)=(monte_nat-
estimates(1))/estimates(2);
                report.position(pos).grain(grain).auto_fit.monte_info.De(i,4)=0;
              end
              waitbar(i/monte_rounds,h)
            end
            delete(h)
            De_error=std(De);
            if isempty(De)==0
              report.position(pos).grain(grain).auto_fit.monte_info.all_fit_De(:,1)=De;
            end
            if isempty(De_error)==0
              report.position(pos).grain(grain).auto_fit.monte_info.std_De_err(1)=De_error;
            end
            if isempty(fail_counter)==0
              report.position(pos).grain(grain).auto_fit.monte_info.fail_counter(1)=fail_counter;
            end
          end
          waitbar((pos-1)*100+grain/600);
          %waitbar(grain/100);
          save( strcat('C:\...\Matlab reports\', current_file, 'temp.mat'), 'report');
        end
      else grain=1;
        report.position(pos).grain(grain).params.signal_lim=[signal_start signal_end];
        report.position(pos).grain(grain).params.bg_lim=[bg_start bg_end];
        report.position(pos).grain(grain).params.meas_error=meas_error;
        report.position(pos).grain(grain).params.mc_repeats=monte_rounds;
        report.position(pos).grain(grain).rej_criteria.zero_ratio(1)=zero_lim;
        report.position(pos).grain(grain).rej_criteria.r_ratio(1)=rr_lim;
        report.position(pos).grain(grain).rej_criteria.tx_err(1)=tx_err;
        %calculate Lx, Tx and errors over user defined integration
        %limits
        current_pos=pos;
        grain_no=grain;
        %error includes meas_error added in quad
        [y_points, y_error, nat_x, nat_y, nat_error, signal, background, all_y_points,
nat_tx_error]=get_y_points( dose_matrix, osl_cycle_counter, ir_cycle_counter, sar_type, current_pos,
OSL_data, IR_data, grain_no, signal_start, signal_end, bg_start,bg_end, meas_error)
        %fill in info about grain for report
        report.position(pos).grain(grain).growth_data.y_points=y_points;
        report.position(pos).grain(grain).growth_data.y_error=y_error;
        report.position(pos).grain(grain).growth_data.doses=doses;
        report.position(pos).grain(grain).growth_data.nat_y=nat_y;
        report.position(pos).grain(grain).growth_data.nat_error=nat_error;
        report.position(pos).grain(grain).growth_data.raw_data(1,:)=all_y_points(:);
        report.position(pos).grain(grain).growth_data.raw_data(2,:)=signal(:);
        report.position(pos).grain(grain).growth_data.raw_data(3,:)=background(:);
        combined_matrix(1,:)=doses(1,:);
        combined_matrix(2,:)=y_points(1,:);
        combined_matrix(3,:)=y_error(1,:);
        %sort matrix by first row (doses), ascending
        combined_matrix=combined_matrix';
        combined_matrix=sortrows(combined_matrix, 1);
        sorted_doses=combined_matrix';
```

```
        %calc zero ratio
        %if disc has 0 dose then calc zero-ratio
        if sorted_doses(1, 1)==0
           if nat_y==0
              zero_ratio=1;
           else zero_ratio=sorted_doses(2,1)/nat_y;
           end
           if sorted_doses(2,1)==0 || nat_y==0
              zero_ratio_err=0;
           else
zero_ratio_err=zero_ratio*((sorted_doses(3,1)/sorted_doses(2,1))^2+(nat_error/nat_y)^2)^.5;
           end
           if abs(zero_ratio)<=(zero_lim/100)|| [((zero_ratio+2*zero_ratio_err)>0) &&((zero_ratio-
2*zero_ratio_err)<0)]
              %if abs(zero_ratio)<=(zero_lim/100)
              zero_pass=0; %0 means passes
           else zero_pass=1;
           end
           % need? rejection_values.position(pos).grain(grain).values(1)=zero_ratio;
           %need? rejection_values.position(pos).grain(grain).values(2)=zero_ratio_err;
           %need? rejection_values.position(pos).grain(grain).zero_pass=zero_pass;
           report.position(pos).grain(grain).rej_criteria.zero_ratio(2)=zero_pass;
           report.position(pos).grain(grain).rej_criteria.zero_ratio(3)=zero_ratio;
           report.position(pos).grain(grain).rej_criteria.zero_ratio(4)=zero_ratio_err;
           has_rej_values(1,1)=1; %has zero ratio value
           has_rej_values(2,1)=zero_pass;
        else has_rej_values(1,1)=0; %has no zero dose
           has_rej_values(2,1)=0;
           report.position(pos).grain(grain).rej_criteria.zero_ratio(2)=-1;
        end
        %calc r-ratio if available
        [b1, m1, n1] = unique(sorted_doses(1,:), 'first');
        [b2, m2, n2] = unique(sorted_doses(1,:), 'last');
        [c,indices]=setdiff(m1,m2);
        if isempty(c)==0 % if there is a repeat dose,
           repeat_dose=sorted_doses(1,m1(indices(1)));  %use first one only
           first_y=sorted_doses(2,m1(indices(1)));
           first_y_err=sorted_doses(3,m1(indices(1)));
           second_y=sorted_doses(2,m2(indices(1)));
           second_y_err=sorted_doses(3,m2(indices(1)));
           if first_y==0
              r_ratio=0;
           else r_ratio=second_y/first_y;
           end
           if first_y==0 || second_y==0
              r_ratio_err=0;
           else r_ratio_err=r_ratio*((first_y_err/first_y)^2+(second_y_err/second_y)^2)^.5;
           end
           if abs(r_ratio-1)<=(rr_lim/100)|| [((r_ratio+2*r_ratio_err)>1) &&((r_ratio-2*r_ratio_err)<1)]
              %if abs(r_ratio-1)<=(rr_lim/100)
              rr_pass=0; %it passes
           else rr_pass=1;
           end
           report.position(pos).grain(grain).rej_criteria.r_ratio(2)=rr_pass;
           report.position(pos).grain(grain).rej_criteria.r_ratio(3)=r_ratio;
           report.position(pos).grain(grain).rej_criteria.r_ratio(4)=r_ratio_err;
           has_rej_values(1,2)=1;
```

```
            has_rej_values(2,2)=rr_pass;
        else has_rej_values(1,2)=0;  %no rejection value
            has_rej_values(2,2)=0;
            report.position(pos).grain(grain).rej_criteria.r_ratio(2)=-1;
        end
        if (nat_tx_error/all_y_points(2))>(tx_err/100)
            tx_pass=1;  %fails
        else tx_pass=0;    %passes
        end
        report.position(pos).grain(grain).rej_criteria.tx_err(2)=tx_pass;
        report.position(pos).grain(grain).rej_criteria.tx_err(3)=nat_tx_error;
        %rejection_values.position(pos).grain(grain).tx_pass=tx_pass;
        %check signal >3 sigma ABOVE bg
        std_dev=std(OSL_data.position(pos).grain(grain).cycle(1).timeseries(bg_start:bg_end));
        %all_y_points is difference of signal and avg background*signal
        %integ channels
        if (all_y_points(1)/(signal_end-signal_start +1))<(3*std_dev)
            sigma_pass=1; %fails
        else sigma_pass=0;
        end
        %rejection_values.position(pos).grain(grain).sigma_pass=sigma_pass;
        report.position(pos).grain(grain).rej_criteria.sigma=sigma_pass;
        %calc IR rejection
        IR_signal=sum(IR_data.position(pos).grain(grain_no).cycle(1).timeseries(signal_start:signal_end));
        IR_background=(signal_end-signal_start
+1)*mean(IR_data.position(pos).grain(grain_no).cycle(1).timeseries(bg_start:bg_end));
        IR_std_dev=std(IR_data.position(pos).grain(grain).cycle(1).timeseries(bg_start:bg_end));
        if ((IR_signal-IR_background)/(signal_end-signal_start +1))<(3*IR_std_dev)
            IR_pass=0; %fails
        else IR_pass=1;
        end
        report.position(pos).grain(grain).rej_criteria.ir_sigma=IR_pass;
        %if pass tx err and sigma then fit
        if tx_pass==0 && sigma_pass==0
            accepted_grains(index, 1)=pos;
            accepted_grains(index, 2)=grain;
            %now fit grain
            chi_array=cell(3,3);
            fit_type=1;
            [x_data, y_data, De, De_error, monte_results, weighted_resid, exit_flag,
fit_params]=fit_curve_no_gui(monte_rounds, mc, stable, fit_type, nat_y, nat_x, y_error, dose_matrix,
y_points, nat_error, osl_cycle_counter, ir_cycle_counter, current_pos)
            chi_array(1,1)={weighted_resid};
            chi_array(2,1)={De};
            chi_array(3,1)={fit_params};
            report.position(pos).grain(grain).auto_fit.weighted_resid(1)=weighted_resid;
            fit_type=2;
            [x_data, y_data, De, De_error, monte_results, weighted_resid, exit_flag,
fit_params]=fit_curve_no_gui(monte_rounds, mc, stable, fit_type, nat_y, nat_x, y_error, dose_matrix,
y_points, nat_error, osl_cycle_counter, ir_cycle_counter, current_pos)
            chi_array(1,2)={weighted_resid};
            chi_array(2,2)={De};
            chi_array(3,2)={fit_params};
            report.position(pos).grain(grain).auto_fit.weighted_resid(2)=weighted_resid;
            fit_type=3;
```

```
        [x_data, y_data, De, De_error, monte_results, weighted_resid, exit_flag,
fit_params]=fit_curve_no_gui(monte_rounds, mc, stable, fit_type, nat_y, nat_x, y_error, dose_matrix,
y_points, nat_error, osl_cycle_counter, ir_cycle_counter, current_pos)
        chi_array(2,3)={De};
        chi_array(1,3)={weighted_resid};
        chi_array(3,3)={fit_params};
        report.position(pos).grain(grain).auto_fit.weighted_resid(3)=weighted_resid;
        %need progress bar
        index=index+1;
        %choose which fit type to use
        for array_val=1:3
          if isfinite(chi_array{1, array_val})==1
            chi_matrix(array_val)=chi_array{1, array_val};
          else chi_matrix(array_val)=Inf;
          end
        end
        [min_val, chosen_fit]=min(chi_matrix(1,:));
        report.position(pos).grain(grain).auto_fit.chosen_fit=chosen_fit;
        report.position(pos).grain(grain).auto_fit.central_De=  chi_array{2,chosen_fit};
        report.position(pos).grain(grain).auto_fit.chosen_fit_params=chi_array{3,chosen_fit};
        %%%%%%%%%%%%get monte carlo De
        monte_rounds=2000;
        fail_counter=0; %use m as index
        accept=1;
        h = waitbar(0,horzcat(current_file, ' Disc ', num2str(pos), ' Grain ', num2str(grain)));
        De=[];
        for i=1:monte_rounds
          monte_nat=nat_y + nat_error*randn(1);
          auto_fit_eq.position(pos).grain(grain_no).monte_nat(i)=monte_nat;
          report.position(pos).grain(grain).auto_fit.monte_info.monte_nat(i)=monte_nat;
          for j=1:length(y_points)
            monte_growth(j)=y_points(j) + y_error(j)*randn(1);
          end
          report.position(pos).grain(grain).auto_fit.monte_info.monte_growth(i, :)=monte_growth;
          if chosen_fit==1  %fit exponential
            options=optimset('Algorithm', 'levenberg-marquardt');
            start_point = [4 0.01 0];
            estimates=[];
            [estimates,resnorm,residual,exitflag] = lsqcurvefit(@(params, doses) params(1) -params(1)*
exp(-doses*params(2))+params(3), start_point, doses, monte_growth, [], [], options )
            if exitflag>=0 && monte_nat>= (estimates(1)+estimates(3)) %fit converges but De never
intersects (don't need to worry about sigma here)
              De(accept, 1)=Inf; %to signify sat
              accept=accept+1;
              report.position(pos).grain(grain).auto_fit.monte_info.monte_fit_params(i,:)=estimates;
              report.position(pos).grain(grain).auto_fit.monte_info.De(i,1)=1;
              report.position(pos).grain(grain).auto_fit.monte_info.De(i,2)=0;
              report.position(pos).grain(grain).auto_fit.monte_info.De(i,3)=Inf;
              report.position(pos).grain(grain).auto_fit.monte_info.De(i,4)=-(1/estimates(2))*log((-
(.95*(estimates(1)+estimates(3)))+estimates(1)+estimates(3))/estimates(1)); %after which point within
95% of infinite response
            elseif exitflag<0 %fitting does not converge or terminated;
              fail_counter=fail_counter+1;
              report.position(pos).grain(grain).auto_fit.monte_info.monte_fit_params(i,:)=[Inf Inf Inf];
              report.position(pos).grain(grain).auto_fit.monte_info.De(i,1)=-1;
              report.position(pos).grain(grain).auto_fit.monte_info.De(i,2)=1;
              report.position(pos).grain(grain).auto_fit.monte_info.De(i,3)=-(10^30);
```

```
                report.position(pos).grain(grain).auto_fit.monte_info.De(i,4)=0;
            else De_temp=-(1/estimates(2))*log((-monte_nat+estimates(1)+estimates(3))/estimates(1));
                De(accept, 1)=De_temp;
                accept=accept+1;
                report.position(pos).grain(grain).auto_fit.monte_info.monte_fit_params(i,:)=estimates;
                report.position(pos).grain(grain).auto_fit.monte_info.De(i,1)=0;
                report.position(pos).grain(grain).auto_fit.monte_info.De(i,2)=0;
                report.position(pos).grain(grain).auto_fit.monte_info.De(i,3)=De_temp;
                report.position(pos).grain(grain).auto_fit.monte_info.De(i,4)=0;
            end
        elseif chosen_fit==2
            estimates=[];
            %fit lin to two highest dose points first then exp +lin with
            for temp_index=1:length(doses)
                combined_matrix(1,temp_index)=doses(1,temp_index);
                combined_matrix(2,temp_index)=monte_growth(1,temp_index);
            end
            %sort matrix by first row (doses), ascending
            combined_matrix=combined_matrix';
            combined_matrix=sortrows(combined_matrix);
            sorted_doses=combined_matrix';
            size_sorted=size(sorted_doses);
            lin_fit_x(1)=sorted_doses(1,size_sorted(2));
            lin_fit_x(2)=sorted_doses(1,size_sorted(2)-1);
            lin_fit_y(1)=sorted_doses(2,size_sorted(2));
            lin_fit_y(2)=sorted_doses(2,size_sorted(2)-1);
            %find good start point
            start_slope=(lin_fit_y(2)-lin_fit_y(1))/(lin_fit_x(2)-lin_fit_x(1));
            start_inter=(lin_fit_y(1)+lin_fit_y(2)-start_slope*(lin_fit_x(1)+lin_fit_x(2)))/2;
            start_point2 = [4 0.01 0];
            sse = @(params2)sum((((params2(1) -params2(1)* exp(-doses*params2(2))+params2(3))-
monte_growth).^2));
            [estimates2, fval2, exitflag2] = fminsearch(sse, start_point2);
            %fit exp+lin
            start_point = [estimates2(1) estimates2(2) start_slope 0];
            options=optimset('Algorithm', 'levenberg-marquardt');
            [estimates,resnorm,residual,exitflag] = lsqcurvefit(@(params, doses) params(1) -params(1)*
exp(-doses*params(2))+params(3)*doses+params(4), start_point, doses, monte_growth, [], [], options )
            exit_flag=exitflag;
            if exit_flag>=0
                if estimates(3)>0 %fit curve does not sat
                    [De_temp, fval, exitflag]=fzero(@(x) estimates(1)-estimates(1)*exp(-
x*estimates(2))+estimates(3)*x+estimates(4)-monte_nat, 0);
                    if exitflag<0 %fitting does not converge or terminated
                        fail_counter=fail_counter+1;
                        report.position(pos).grain(grain).auto_fit.monte_info.monte_fit_params(i,:)=[Inf Inf
Inf Inf];
                        report.position(pos).grain(grain).auto_fit.monte_info.De(i,1)=0;
                        report.position(pos).grain(grain).auto_fit.monte_info.De(i,2)=1;
                        report.position(pos).grain(grain).auto_fit.monte_info.De(i,3)=-(10^30);
                        report.position(pos).grain(grain).auto_fit.monte_info.De(i,4)=0;
                    else De(accept, 1)=De_temp;
                        accept=accept+1;
report.position(pos).grain(grain).auto_fit.monte_info.monte_fit_params(i,:)=estimates;
                        report.position(pos).grain(grain).auto_fit.monte_info.De(i,1)=0;
                        report.position(pos).grain(grain).auto_fit.monte_info.De(i,2)=0;
                        report.position(pos).grain(grain).auto_fit.monte_info.De(i,3)=De_temp;
```

```
                    report.position(pos).grain(grain).auto_fit.monte_info.De(i,4)=0;
                  end
                elseif estimates(3)<0 %then the fit curve will have a max value
                  max_x=(-1/estimates(2))*(log(-estimates(3)/(estimates(2)*estimates(1))));
                  max_y=estimates(1)-estimates(1)*exp(-
estimates(2)*max_x)+estimates(3)*max_x+estimates(4);
                  if monte_nat>=max_y
                    De(accept, 1)=Inf;
                    accept=accept+1;
report.position(pos).grain(grain).auto_fit.monte_info.monte_fit_params(i,:)=estimates;
                    report.position(pos).grain(grain).auto_fit.monte_info.De(i,1)=1;
                    report.position(pos).grain(grain).auto_fit.monte_info.De(i,2)=0;
                    report.position(pos).grain(grain).auto_fit.monte_info.De(i,3)=Inf;
                    report.position(pos).grain(grain).auto_fit.monte_info.De(i,4)=max_x;
                  else [De_temp, fval, exitflag]=fzero(@(x) estimates(1)-estimates(1)*exp(-
x*estimates(2))+estimates(3)*x+estimates(4)-monte_nat, 0);
                    if exitflag<0 %fitting does not converge or terminated
                      fail_counter=fail_counter+1;
                      report.position(pos).grain(grain).auto_fit.monte_info.monte_fit_params(i,:)=[Inf Inf
Inf Inf];
                      report.position(pos).grain(grain).auto_fit.monte_info.De(i,1)=0;
                      report.position(pos).grain(grain).auto_fit.monte_info.De(i,2)=1;
                      report.position(pos).grain(grain).auto_fit.monte_info.De(i,3)=-(10^30);
                      report.position(pos).grain(grain).auto_fit.monte_info.De(i,4)=0;
                    else De(accept, 1)=De_temp;
                      accept=accept+1;

report.position(pos).grain(grain).auto_fit.monte_info.monte_fit_params(i,:)=estimates;
                      report.position(pos).grain(grain).auto_fit.monte_info.De(i,1)=0;
                      report.position(pos).grain(grain).auto_fit.monte_info.De(i,2)=0;
                      report.position(pos).grain(grain).auto_fit.monte_info.De(i,3)=De_temp;
                      report.position(pos).grain(grain).auto_fit.monte_info.De(i,4)=0;
                    end
                  end
                end
              else  %fitting does not converge or terminated; no De recorded in list
                fail_counter=fail_counter+1;
                report.position(pos).grain(grain).auto_fit.monte_info.monte_fit_params(i,:)=[Inf Inf Inf
Inf];
                report.position(pos).grain(grain).auto_fit.monte_info.De(i,1)=-1;
                report.position(pos).grain(grain).auto_fit.monte_info.De(i,2)=1;
                report.position(pos).grain(grain).auto_fit.monte_info.De(i,3)=-(10^30);
                report.position(pos).grain(grain).auto_fit.monte_info.De(i,4)=0;
              end
            elseif chosen_fit==3
              start_point = [0.05 0.005];
              sse = @(params)sum((((params(1) +params(2)* doses)-monte_growth).^2));
              estimates = fminsearch(sse, start_point);
              De(accept, 1)=(monte_nat-estimates(1))/estimates(2);
              accept=accept+1;
              report.position(pos).grain(grain).auto_fit.monte_info.monte_fit_params(i,:)=estimates;
              report.position(pos).grain(grain).auto_fit.monte_info.De(i,1)=0;
              report.position(pos).grain(grain).auto_fit.monte_info.De(i,2)=0;
              report.position(pos).grain(grain).auto_fit.monte_info.De(i,3)=(monte_nat-
estimates(1))/estimates(2);
              report.position(pos).grain(grain).auto_fit.monte_info.De(i,4)=0;
            end
```

```
            waitbar(i/monte_rounds,h)
          end
          delete(h)
          De_error=std(De);
          if isempty(De)==0
            report.position(pos).grain(grain).auto_fit.monte_info.all_fit_De(:,1)=De;
          end
          if isempty(De_error)==0
            report.position(pos).grain(grain).auto_fit.monte_info.std_De_err(1)=De_error;
          end
          if isempty(fail_counter)==0
            report.position(pos).grain(grain).auto_fit.monte_info.fail_counter(1)=fail_counter;
          end
          report.position(pos).grain(grain).auto_fit.monte_info.De(i,4)=0;
        end
        %h=waitbar(grain/100);
        save( strcat('C:\...\Matlab reports\', current_file, 'temp.mat'), 'report');
      end
   else pos=pos+1;
   end
end
```

Curve Fitting Procedure

```
function [x_data, y_data, De, De_error, monte_results, weighted_resid, exit_flag,
fit_params]=fit_curve_no_gui(monte_rounds, mc, stable, fit_type, nat_y, nat_x, y_error, dose_matrix,
y_points, nat_error, osl_cycle_counter, ir_cycle_counter, current_pos)
exit_flag=100;
doses=dose_matrix.position(current_pos).dose;
fit_params=[];
if osl_cycle_counter(current_pos, 1)>0
   x_data=[];
   y_data=[];
   De=[];
   De_error=[];
   monte_results=[];
   weighted_resid=[];
   fit_params=[];
   if fit_type==1
      %fit exponential
      start_point = [4 0.01 0];
      %weighted by errors squared
      sse = @(params)sum((((params(1) -params(1)* exp(-doses*params(2))+params(3))-
y_points).^2)./(y_error.^2));
      [estimates, fval, exitflag] = fminsearch(sse, start_point);
      exit_flag=exitflag;
      if exitflag>=0  %if can be fit
         weighted_resid=sum(((y_points-(estimates(1)-estimates(1)*exp(-
doses*estimates(2))+estimates(3))).^2)./(y_error.^2));
         fit_params=estimates;
         %calc equivalent dose central value with fit curve provided not
         %taking log of negative number or 0
         %if de overlap params(1)+params(3) value at one sigma then sat
         %and don't find De
```

```
        if (estimates(1)>0 & estimates(2)>0 & isfinite(estimates(1))==1 & isfinite(estimates(2))==1 &
isfinite(estimates(3))==1)&((nat_y-nat_error)<=(estimates(1)+estimates(3))) &
((nat_y+nat_error)>=(estimates(1)+estimates(3)))
            %then de is sat
            De(1,1)=[10^17];
            De(1,2)=-(1/estimates(2))*log((-(nat_y-2*nat_error)+estimates(1)+estimates(3))/estimates(1));
        elseif (estimates(1)>0 & estimates(2)>0 & isfinite(estimates(1))==1 & isfinite(estimates(2))==1 &
isfinite(estimates(3))==1)&((nat_y-nat_error)>(estimates(1)+estimates(3))) %then de supersat
            De(1,1)=[10^20];
            De(1,2)=[10^20];
        elseif (estimates(1)>0 & estimates(2)>0 & isfinite(estimates(1))==1 & isfinite(estimates(2))==1 &
isfinite(estimates(3))==1)&&((-nat_y+estimates(1)+estimates(3))/estimates(1))>0
            De(1,1)=-(1/estimates(2))*log((-nat_y+estimates(1)+estimates(3))/estimates(1));
            De(1,2)=0;
        else
            De(1,1)=-(10^30); %used for when De can't be fit for some reason
            De(1,2)=0;
        end
    else weighted_resid=Inf;
        De(1,1)=-(10^30); %used for when De can't be fit for some reason
        De(1,2)=0;
    end
    %these estimates are weighted depending on the point
  elseif fit_type==2
    %fit lin to two highest dose points first then exp +lin with
    %start points from lin fitting
    %what if intersects in two places?
    for temp_index=1:length(doses)
        combined_matrix(1,temp_index)=doses(1,temp_index);

        combined_matrix(2,temp_index)=y_points(1,temp_index);
    end
    %sort matrix by first row (doses), ascending
    combined_matrix=combined_matrix';
    combined_matrix=sortrows(combined_matrix);
    sorted_doses=combined_matrix';
    size_sorted=size(sorted_doses);
    lin_fit_x(1)=sorted_doses(1,size_sorted(2));
    lin_fit_x(2)=sorted_doses(1,size_sorted(2)-1);
    lin_fit_y(1)=sorted_doses(2,size_sorted(2));
    lin_fit_y(2)=sorted_doses(2,size_sorted(2)-1);
    temp_test(:,1)=lin_fit_x;
    temp_test(:,2)=lin_fit_y;
    %find good start point for lin
    start_slope=(lin_fit_y(2)-lin_fit_y(1))/(lin_fit_x(2)-lin_fit_x(1));
    start_inter=(lin_fit_y(1)+lin_fit_y(2)-start_slope*(lin_fit_x(1)+lin_fit_x(2)))/2;
    start_point2 = [4 0.01 0];
    %weighted by errors squared
    sse = @(params2)sum((((params2(1) -params2(1)* exp(-doses*params2(2))+params2(3))-
y_points).^2)./(y_error.^2));
    [estimates2, fval2, exitflag2] = fminsearch(sse, start_point2);
    %fit exp+lin
    if isreal(estimates2(1))==1 & isfinite(estimates2(1))==1 & isreal(estimates2(2))==1 &
isfinite(estimates2(2))==1 & isreal(start_slope)==1 & isfinite(start_slope)==1
        start_point = [estimates2(1) estimates2(2) start_slope 0];
    else start_point=[4 0.01 1 0];
    end
```

```
    sse = @(params)sum((((params(1) -params(1)* exp(-doses*params(2))+params(3)*doses+params(4))-
y_points).^2)./(y_error.^2));
    [estimates, fval, exitflag] = fminsearch(sse, start_point);
    exit_flag=exitflag;
    if exit_flag>=0 %curve fitting succeeds
      weighted_resid=sum(((y_points-(estimates(1)-estimates(1)*exp(-
doses*estimates(2))+estimates(3)*doses+estimates(4))).^2)./(y_error.^2));
      fit_params=estimates;
      if (estimates(1)>0 & estimates(2)>0 & isfinite(estimates(1))==1 & isfinite(estimates(2))==1 &
isfinite(estimates(3))==1 & isfinite(estimates(4))==1)& estimates(3)<0 %curve sats at some point
        max_x=-(1/estimates(2))*log(-estimates(3)/(estimates(1)*estimates(2)));
        max_y=estimates(1)+estimates(4)+(estimates(3)/estimates(2))*(1-log(-
estimates(3)/(estimates(1)*estimates(2))));
        if ((nat_y-nat_error)<=max_y) & ((nat_y+nat_error)>=max_y)
          %then de is sat
          De(1,1)=[10^17];
          [De1, fval, exitflag3]=fzero(@(x) estimates(1)-estimates(1)*exp(-
x*estimates(2))+estimates(3)*x+estimates(4)-(nat_y-2*nat_error), 0);
          if exitflag3<=0 %fitting does not converge or terminated
            De(1,2)=-(10^30);
          else De(1,2)=De1;
          end
        elseif ((nat_y-nat_error)>max_y) %then de supersat
          De(1,1)=[10^20];
          De(1,2)=[10^20];
        else
          [De1, fval, exitflag]=fzero(@(x) estimates(1)-estimates(1)*exp(-
x*estimates(2))+estimates(3)*x+estimates(4)-nat_y, 0);
          De(1,1)=De1;
          De(1,2)=0;
          if exitflag<0 %if De can't be fit then it is neg 10^30
            De(1,1)=-(10^30);
          end
        end
      elseif (estimates(1)>0 & estimates(2)>0 & isfinite(estimates(1))==1 & isfinite(estimates(2))==1 &
isfinite(estimates(3))==1 & isfinite(estimates(4))==1)
        [De1, fval, exitflag]=fzero(@(x) estimates(1)-estimates(1)*exp(-
x*estimates(2))+estimates(3)*x+estimates(4)-nat_y, 0);
        De(1,1)=De1;
        De(1,2)=0;
        if exitflag<0 %if De can't be fit then it is neg 10^30
          De(1,1)=-(10^30);
        end
      elseif isfinite(estimates(1))==1 &  isfinite(estimates(2))==1  &  isfinite(estimates(3))==1  &
isfinite(estimates(4))==1
        [De1, fval, exitflag]=fzero(@(x) estimates(1)-estimates(1)*exp(-
x*estimates(2))+estimates(3)*x+estimates(4)-nat_y, 0);
        De(1,1)=De1;
        De(1,2)=0;
        if exitflag<0 %if De can't be fit then it is neg 10^30
          De(1,1)=-(10^30);
        end
      else
        De(1,1)=-(10^30);
      end
    else weighted_resid=Inf; %can't fit curve
      fit_params=[];
```

```
        x_data=[];
        y_data=[];
        De(1,1)=-(10^30);
        De(1,2)=0;
      end
      %fit linear
    elseif fit_type==3
      y_data2=[];
      start_point = [0.05 0.005];
      sse = @(params)sum((((params(1) +params(2)* doses)-y_points).^2)./(y_error.^2));
      estimates = fminsearch(sse, start_point);
      fit_params=estimates;
      De(1,1)=(nat_y-estimates(1))/estimates(2);
      De(1,2)=0;
      %get x and y for plotting fitted curve
      weighted_resid=sum(((y_points-(estimates(1)+estimates(2)*doses)).^2)./(y_error.^2));
      exitflag=[];
    end
    De_error=[];
    monte_results=[];
else
    x_data=[];
    y_data=[];
    De=[];
    De_error=[];
    monte_results=[];
    weighted_resid=[];
    fit_params=[];
end
```

Appendix B: Bayesian model codes

This appendix provides the code used to run the Taforalt and Dar es-Soltan I Bayesian models in OxCal v4.1 (Bronk Ramsey, 2009a). Model details have been explained in Chapter 5. Each model is headed by a title (not part of the code), and the two models are separated by a solid line. Both models begin by defining measured parameters as follows: (aliquot_type)_(sample name)_(measured parameter). For the Taforalt model, aliquot types comprise multigrain ('mg'), single grain ('sg'), and VSA ('vsa')). Some parameters (such as alpha dose rate) have been calculated separately for various aliquot types due to grain size dependency. Since only multigrain aliquots were used for the Dar es-Soltan I model, aliquot type has not been indicated in that code. Sample names are those used throughout the text, and parameter types are as follows:

'a': alpha dose rate (Gy ka^{-1})

'b': beta dose rate (Gy ka^{-1})

'g': gamma dose rate (Gy ka^{-1})

'c': cosmic dose rate (Gy ka^{-1})

'de': equivalent dose value (Gy)

'H_a/b/g': water content correction values for alpha/beta/gamma dose (dimensionless)

'high_water/low_water/(sample name)_H2O': water content value (water mass/dry sample mass).

Taforalt

```
   Options()
{ Resolution=200; };
Plot()
{
 N("mg_TAF08_01_a", 0.049314397, 0.025267711);
 N("mg_TAF08_02_a", 0.040074008, 0.021806634);
 N("mg_TAF08_03_a", 0.055792056, 0.028334053);
 N("mg_TAF08_04_a", 0.055478829, 0.02816845);
 N("mg_TAF08_05_a", 0.061637003, 0.031438385);
```

N("mg_TAF08_06_a", 0.061016805, 0.031132207);
N("mg_TAF08_08_a", 0.058442046, 0.030204118);
N("mg_TAF08_10_a", 0.064556347, 0.033137336);
N("mg_TAF08_11_a", 0.057320649, 0.029159607);
N("mg_TAF08_12_a", 0.063015239, 0.032285582);
N("mg_TAF08_13_a", 0.057774847, 0.029535045);
N("mg_TAF08_14_a", 0.055779541, 0.028381869);
N("mg_TAF08_15_a", 0.054858631, 0.027881967);
N("mg_TAF08_16_a", 0.05916247, 0.030231147);
N("mg_TAF08_17_a", 0.039399925, 0.021578967);
N("mg_TAF09_01_a", 0.05056105, 0.025858972);
N("mg_TAF09_08_a", 0.050241565, 0.025657899);
N("mg_TAF09_20_a", 0.059168727, 0.030133573);
N("mg_TAF09_21_a", 0.052396613, 0.026664366);
N("mg_TAF09_22_a", 0.062557913, 0.031971559);
N("mg_TAF09_23_a", 0.059795182, 0.030428093);
N("mg_TAF09_24_a", 0.036077139, 0.020737389);
N("mg_TAF09_25_a", 0.037925217, 0.021174274);
N("mg_TAF09_26_a", 0.041314403, 0.022158678);
N("mg_TAF09_27_a", 0.047165607, 0.02431852);
N("mg_TAF09_34_a", 0.043770164, 0.023030478);
N("mg_TAF09_37_a", 0.0532324, 0.027104494);
N("mg_TAF09_40_a", 0.052791359, 0.026913054);
N("mg_TAF10_01_a", 0.046628114, 0.02424072);
N("mg_TAF10_02_a", 0.073714393, 0.039132737);
N("mg_TAF10_05_a", 0.07824732, 0.041854043);
N("mg_TAF10_06_a", 0.080334366, 0.043451869);
N("mg_TAF10_07_a", 0.085087198, 0.046905853);
N("mg_TAF10_10_a", 0.038133213, 0.021269366);
N("mg_TAF10_11_a", 0.068916688, 0.035987772);
N("mg_TAF10_14_a", 0.066959953, 0.035121444);
N("mg_TAF10_16_a", 0.04833397, 0.024810144);
N("mg_TAF10_17_a", 0.044635312, 0.023326221);
N("mg_TAF10_18_a", 0.052700843, 0.026778008);
N("sg_TAF08_01_a", 0.049314397, 0.025267711);
N("sg_TAF09_27_a", 0.047165607, 0.02431852);
N("sg_TAF08_02_a", 0.040074008, 0.021806634);
N("sg_TAF08_12_a", 0.063015239, 0.032285582);
N("sg_TAF08_13_a", 0.057774847, 0.029535045);
N("sg_TAF09_24_a", 0.036077139, 0.020737389);
N("sg_TAF09_25_a", 0.037925217, 0.021174274);
N("sg_TAF09_26_a", 0.041314403, 0.022158678);
N("sg_TAF09_27_a", 0.047165607, 0.02431852);
N("vsa_TAF09_35_a", 0.058120775, 0.029606601);
N("sg_TAF09_35_a", 0.049007427, 0.025123001);
N("vsa_TAF09_36_a", 0.050122035, 0.025594814);
N("sg_TAF09_36_a", 0.043463193, 0.022908852);
N("sg_TAF09_37_a", 0.0532324, 0.027104494);
N("sg_TAF09_38_a", 0.039159355, 0.021515009);
N("vsa_TAF09_39_a", 0.057231, 0.029227774);
N("sg_TAF09_39_a", 0.04838723, 0.024906114);
N("sg_TAF09_40_a", 0.045323787, 0.023631213);
N("mg_TAF08_01_b", 0.790125649, 0.051314755);
N("mg_TAF08_02_b", 0.49395579, 0.032846801);
N("mg_TAF08_03_b", 0.965663385, 0.061198621);
N("mg_TAF08_04_b", 0.933615823, 0.058981779);
N("mg_TAF08_05_b", 1.228103089, 0.079458624);

N("mg_TAF08_06_b", 1.235884917, 0.080733695);
N("mg_TAF08_08_b", 1.013461177, 0.064920593);
N("mg_TAF08_10_b", 1.610445802, 0.109919087);
N("mg_TAF08_11_b", 1.199861198, 0.080264302);
N("mg_TAF08_12_b", 1.454597386, 0.097913981);
N("mg_TAF08_13_b", 1.230417648, 0.082970504);
N("mg_TAF08_14_b", 1.061757209, 0.069793362);
N("mg_TAF08_15_b", 0.995363389, 0.064704951);
N("mg_TAF08_16_b", 1.151221556, 0.075250937);
N("mg_TAF08_17_b", 0.657212501, 0.046985661);
N("mg_TAF09_01_b", 0.881401208, 0.057393013);
N("mg_TAF09_08_b", 0.819450047, 0.05298084);
N("mg_TAF09_20_b", 1.45695004, 0.100675836);
N("mg_TAF09_21_b", 0.948308089, 0.062334572);
N("mg_TAF09_22_b", 1.348462647, 0.089048489);
N("mg_TAF09_23_b", 1.173265961, 0.075823334);
N("mg_TAF09_24_b", 0.469529219, 0.033250997);
N("mg_TAF09_25_b", 0.602239491, 0.04317784);
N("mg_TAF09_26_b", 0.595687381, 0.040084015);
N("mg_TAF09_27_b", 0.726133469, 0.047061337);
N("mg_TAF09_34_b", 0.600846696, 0.039258769);
N("mg_TAF09_37_b", 0.803411645, 0.054502491);
N("mg_TAF09_40_b", 0.616759255, 0.038506089);
N("mg_TAF10_01_b", 0.879185969, 0.061118567);
N("mg_TAF10_02_b", 1.244462815, 0.082141135);
N("mg_TAF10_05_b", 1.340285065, 0.08784232);
N("mg_TAF10_06_b", 1.47170031, 0.09821094);
N("mg_TAF10_07_b", 1.55569387, 0.103375488);
N("mg_TAF10_10_b", 0.478994537, 0.032995066);
N("mg_TAF10_11_b", 1.114021877, 0.073217714);
N("mg_TAF10_14_b", 1.104190753, 0.07374878);
N("mg_TAF10_16_b", 0.842105941, 0.056065172);
N("mg_TAF10_17_b", 0.608151102, 0.039147785);
N("mg_TAF10_18_b", 0.684685089, 0.044423514);
N("sg_TAF08_01_b", 0.790125649, 0.051314755);
N("sg_TAF09_27_b", 0.726133469, 0.047061337);
N("sg_TAF08_02_b", 0.49395579, 0.032846801);
N("sg_TAF08_12_b", 1.454597386, 0.097913981);
N("sg_TAF08_13_b", 1.230417648, 0.082970504);
N("sg_TAF09_24_b", 0.469529219, 0.033250997);
N("sg_TAF09_25_b", 0.602239491, 0.04317784);
N("sg_TAF09_26_b", 0.595687381, 0.040084015);
N("sg_TAF09_27_b", 0.726133469, 0.047061337);
N("vsa_TAF09_35_b", 0.901641581, 0.060227368);
N("sg_TAF09_35_b", 0.876909688, 0.058745781);
N("vsa_TAF09_36_b", 0.781649411, 0.054224485);
N("sg_TAF09_36_b", 0.760599949, 0.052903564);
N("sg_TAF09_37_b", 0.803411645, 0.054502491);
N("sg_TAF09_38_b", 0.502806498, 0.033726826);
N("vsa_TAF09_39_b", 0.934081609, 0.063671945);
N("sg_TAF09_39_b", 0.908676288, 0.062114265);
N("sg_TAF09_40_b", 0.599342023, 0.037531734);
N("mg_TAF08_01_g", 0.3617, 0.0177);
N("mg_TAF08_02_g", 0.273921607, 0.020574148);
N("mg_TAF08_03_g", 0.480358892, 0.034586646);
N("mg_TAF08_04_g", 0.465599221, 0.033999635);
N("mg_TAF08_05_g", 0.776000021, 0.032055877);

```
N("mg_TAF08_06_g", 0.77551145, 0.032196506);
N("mg_TAF08_08_g", 0.518426528, 0.037790468);
N("mg_TAF08_10_g", 0.537794639, 0.039653679);
N("mg_TAF08_11_g", 0.542437251, 0.040736495);
N("mg_TAF08_12_g", 0.584049872, 0.043259293);
N("mg_TAF08_13_g", 0.566791575, 0.042587879);
N("mg_TAF08_14_g", 0.616525676, 0.044837687);
N("mg_TAF08_15_g", 0.616525676, 0.044837687);
N("mg_TAF08_16_g", 0.636711157, 0.043052462);
N("mg_TAF08_17_g", 0.268374948, 0.019877869);
N("mg_TAF09_01_g", 0.380187303, 0.026245671);
N("mg_TAF09_08_g", 0.313382107, 0.02266206);
N("mg_TAF09_20_g", 0.558057594, 0.042026964);
N("mg_TAF09_21_g", 0.583560631, 0.043906);
N("mg_TAF09_22_g", 0.538535726, 0.040271709);
N("mg_TAF09_23_g", 0.53842798, 0.039521546);
N("mg_TAF09_24_g", 0.250220009, 0.010904694);
N("mg_TAF09_25_g", 0.314125726, 0.013875147);
N("mg_TAF09_26_g", 0.273134835, 0.019588528);
N("mg_TAF09_27_g", 0.302983473, 0.021927727);
N("mg_TAF09_34_g", 0.311339158, 0.023371571);
N("mg_TAF09_37_g", 0.4604943, 0.019455806);
N("mg_TAF09_40_g", 0.4326, 0.0169);
N("mg_TAF10_01_g", 0.294158987, 0.020832861);
N("mg_TAF10_02_g", 0.955576644, 0.065258203);
N("mg_TAF10_05_g", 0.9093824, 0.063347765);
N("mg_TAF10_06_g", 0.930232101, 0.064206362);
N("mg_TAF10_07_g", 0.931387064, 0.064254103);
N("mg_TAF10_10_g", 0.3158, 0.0143);
N("mg_TAF10_11_g", 0.561425103, 0.041990181);
N("mg_TAF10_14_g", 0.627704128, 0.046089063);
N("mg_TAF10_16_g", 0.440663238, 0.030929813);
N("mg_TAF10_17_g", 0.3386, 0.0157);
N("mg_TAF10_18_g", 0.3518, 0.0169);
N("sg_TAF08_01_g", 0.3617, 0.0177);
N("sg_TAF09_27_g", 0.302983473, 0.021927727);
N("sg_TAF08_02_g", 0.273921607, 0.020574148);
N("sg_TAF08_12_g", 0.584049872, 0.043259293);
N("sg_TAF08_13_g", 0.566791575, 0.042587879);
N("sg_TAF09_24_g", 0.250220009, 0.010904694);
N("sg_TAF09_25_g", 0.314125726, 0.013875147);
N("sg_TAF09_26_g", 0.273134835, 0.019588528);
N("sg_TAF09_27_g", 0.302983473, 0.021927727);
N("vsa_TAF09_35_g", 0.4969, 0.0221);
N("sg_TAF09_35_g", 0.4969, 0.0221);
N("vsa_TAF09_36_g", 0.4602, 0.0188);
N("sg_TAF09_36_g", 0.4602, 0.0188);
N("sg_TAF09_37_g", 0.4604943, 0.019455806);
N("sg_TAF09_38_g", 0.270348077, 0.019476946);
N("vsa_TAF09_39_g", 0.4872, 0.0194);
N("sg_TAF09_39_g", 0.4872, 0.0194);
N("sg_TAF09_40_g", 0.4326, 0.0169);
N("mg_TAF08_01_c", 0.03039728, 0.008044215);
N("mg_TAF08_02_c", 0.031325343, 0.008289115);
N("mg_TAF08_03_c", 0.056028859, 0.00780162);
N("mg_TAF08_04_c", 0.057561803, 0.008272463);
N("mg_TAF08_05_c", 0.059258471, 0.008417443);
```

N("mg_TAF08_06_c", 0.058601267, 0.008067596);
N("mg_TAF08_08_c", 0.070608836, 0.00904432);
N("mg_TAF08_10_c", 0.050328632, 0.008639741);
N("mg_TAF08_11_c", 0.051319409, 0.009040609);
N("mg_TAF08_12_c", 0.052528643, 0.00888013);
N("mg_TAF08_13_c", 0.053732034, 0.009473767);
N("mg_TAF08_14_c", 0.056631583, 0.008486893);
N("mg_TAF08_15_c", 0.056928822, 0.00863073);
N("mg_TAF08_16_c", 0.059285159, 0.008979196);
N("mg_TAF08_17_c", 0.041872491, 0.016122362);
N("mg_TAF09_01_c", 0.048895873, 0.008555676);
N("mg_TAF09_08_c", 0.051103491, 0.007678482);
N("mg_TAF09_20_c", 0.09367651, 0.00852838);
N("mg_TAF09_21_c", 0.090582556, 0.008166369);
N("mg_TAF09_22_c", 0.087080836, 0.007873304);
N("mg_TAF09_23_c", 0.084948135, 0.007819923);
N("mg_TAF09_24_c", 0.082109659, 0.012131301);
N("mg_TAF09_25_c", 0.075253777, 0.010610318);
N("mg_TAF09_26_c", 0.032751359, 0.008725997);
N("mg_TAF09_27_c", 0.032049435, 0.008537704);
N("mg_TAF09_34_c", 0.026803928, 0.007034457);
N("mg_TAF09_37_c", 0.033344161, 0.008929348);
N("mg_TAF09_40_c", 0.032049435, 0.008206853);
N("mg_TAF10_01_c", 0.027411365, 0.00716676);
N("mg_TAF10_02_c", 0.049750287, 0.009268069);
N("mg_TAF10_05_c", 0.049080531, 0.009484075);
N("mg_TAF10_06_c", 0.048860339, 0.009083112);
N("mg_TAF10_07_c", 0.048641656, 0.009177632);
N("mg_TAF10_10_c", 0.057315559, 0.008610431);
N("mg_TAF10_11_c", 0.064216057, 0.008979353);
N("mg_TAF10_14_c", 0.06205116, 0.008703976);
N("mg_TAF10_16_c", 0.081531587, 0.007512919);
N("mg_TAF10_17_c", 0.031300904, 0.008187731);
N("mg_TAF10_18_c", 0.030286172, 0.008475734);
N("sg_TAF08_01_c", 0.03039728, 0.008588443);
N("sg_TAF09_27_c", 0.032049435, 0.008450828);
N("sg_TAF08_02_c", 0.031325343, 0.008194115);
N("sg_TAF08_12_c", 0.052528643, 0.009261785);
N("sg_TAF08_13_c", 0.053732034, 0.00935553);
N("sg_TAF09_24_c", 0.082109659, 0.012268122);
N("sg_TAF09_25_c", 0.075253777, 0.010293478);
N("sg_TAF09_26_c", 0.032751359, 0.008530813);
N("sg_TAF09_27_c", 0.032049435, 0.008601567);
N("vsa_TAF09_35_c", 0.033970771, 0.009021942);
N("sg_TAF09_35_c", 0.033970771, 0.008630177);
N("vsa_TAF09_36_c", 0.03387191, 0.008717595);
N("sg_TAF09_36_c", 0.03387191, 0.008986016);
N("sg_TAF09_37_c", 0.033344161, 0.008556952);
N("sg_TAF09_38_c", 0.032911133, 0.00870574);
N("vsa_TAF09_39_c", 0.03220305, 0.008516398);
N("sg_TAF09_39_c", 0.03220305, 0.008716729);
N("sg_TAF09_40_c", 0.032049435, 0.008522043);
N("mg_TAF08_03_de", 59.12291036, 3.205925873);
N("mg_TAF08_04_de", 51.73670327, 2.8505646);
N("mg_TAF08_05_de", 56.40083909, 3.181118501);
N("mg_TAF08_06_de", 44.0088202, 2.428992503);
N("mg_TAF08_08_de", 40.91964013, 2.794417127);

```
N("mg_TAF08_10_de", 60.95697379, 1.733795724);
N("mg_TAF08_11_de", 45.32757808, 3.151420002);
N("mg_TAF08_12_de", 42.52619788, 2.83369224);
N("mg_TAF08_13_de", 32.83381916, 1.613657494);
N("mg_TAF08_14_de", 40.37356685, 1.665471873);
N("mg_TAF08_15_de", 44.11267676, 2.719621445);
N("mg_TAF08_16_de", 37.26527861, 1.894965391);
N("mg_TAF08_17_de", 13.70819094, 1.073824192);
N("mg_TAF09_01_de", 46.64440717, 3.305853009);
N("mg_TAF09_08_de", 47.07562214, 3.790426131);
N("mg_TAF09_20_de", 34.86408981, 2.080969282);
N("mg_TAF09_21_de", 36.3062512, 2.325386018);
N("mg_TAF09_22_de", 45.78060114, 1.405562253);
N("mg_TAF09_23_de", 45.33309454, 3.91071981);
N("mg_TAF09_24_de", 14.80547244, 0.600227496);
N("mg_TAF09_25_de", 19.27065749, 1.508763953);
N("mg_TAF09_26_de", 65.71905155, 10.69959226);
N("mg_TAF09_34_de", 146.2038, 6.0008);
N("mg_TAF09_37_de", 79.25012923, 7.830073253);
N("mg_TAF09_40_de", 64.85920977, 4.099462669);
N("mg_TAF10_01_de", 127.4138268, 12.37012449);
N("mg_TAF10_02_de", 33.88645227, 2.281352425);
N("mg_TAF10_05_de", 45.35979763, 3.866348518);
N("mg_TAF10_06_de", 43.7196063, 1.935523572);
N("mg_TAF10_07_de", 43.32404703, 2.679992704);
N("mg_TAF10_10_de", 11.90923698, 0.567559346);
N("mg_TAF10_11_de", 21.50383582, 0.943979589);
N("mg_TAF10_14_de", 39.09108012, 1.551605386);
N("mg_TAF10_16_de", 45.93290169, 2.888027521);
N("mg_TAF09_27_de", 87.20332731, 6.965622534);
N("mg_TAF10_17_de", 61.5096, 1.2264);
N("mg_TAF10_18_de", 73.77326073, 5.631442719);
N("sg_TAF09_27_de", 86.76744717, 8.55084238);
N("sg_TAF08_02_de", 74.8267554, 7.599512294);
N("sg_TAF08_12_de", 37.45784315, 1.891358714);
N("sg_TAF08_13_de", 29.94231945, 1.082095944);
N("sg_TAF09_24_de", 14.09605332, 0.387436237);
N("sg_TAF09_25_de", 18.32313444, 1.282415175);
N("sg_TAF09_26_de", 54.27081143, 2.718194195);
N("vsa_TAF09_35_de", 56.96189287, 2.63089919);
N("sg_TAF09_35_de", 48.51264006, 8.302605166);
N("vsa_TAF09_36_de", 55.54536306, 1.396183126);
N("sg_TAF09_36_de", 74.20567101, 16.690483);
N("sg_TAF09_37_de", 88.69275056, 8.797757821);
N("sg_TAF09_38_de", 41.7029445, 3.783760323);
N("vsa_TAF09_39_de", 76.63386818, 4.142365801);
N("sg_TAF09_39_de", 44.53668798, 18.51745988);
N("sg_TAF09_40_de", 71.56095071, 12.38704679);
N("mg_TAF08_01_de", 115.5792281, 11.11400668);
N("mg_TAF08_02_de", 97.33926204, 4.871999269);
N("sg_TAF08_01_de", 91.23131641, 9.652232658);
//correction factors
N("H_a", 1.5,.05*1.5 );
N("H_b", 1.25,.05*1.25 );
N("H_g",1.14 , .05*1.14);
//water contents
N("high_water", .1364, .0491);
```

```
N("low_water", .0336, .015);
Outlier_Model("General",T(5),U(0,4),"t");
Sequence()
{
 Boundary("Base Calcareous");
 Phase("Calcareous Group")
 {
  Sequence("Sector 1")
  {
   Combine("TAF08-01")
   {
    TAF08_01_mg=Age(1000*mg_TAF08_01_de/((mg_TAF08_01_b/(1+H_b*high_water))+…
          (mg_TAF08_01_a/(1+H_a*high_water))+(mg_TAF08_01_g/(1+H_g*high_water))+…
          mg_TAF08_01_    c))  { Outlier(0.05); };
     TAF08_01_sg=TAF08_01_sg=Age(1000*sg_TAF08_01_de/((sg_TAF08_01_b/(1+H_b*high_water))+…
          (sg_TAF08_01_a/(1+H_a*high_water))+(sg_TAF08_01_g/(1+H_g*high_water))+…
          sg_TAF08_01_c))  { Outlier(0.5); };
   };
   Date("Flowstone");
   Combine("TAF08-02")
   {
    TAF08_02_mg=Age(1000*mg_TAF08_02_de/((mg_TAF08_02_b/(1+H_b*high_water))+…
          (mg_TAF08_02_a/(1+H_a*high_water))+(mg_TAF08_02_g/(1+H_g*high_water))+…
          mg_TAF08_02_c))  { Outlier(0.5); };
    TAF08_02_sg=Age(1000*sg_TAF08_02_de/((sg_TAF08_02_b/(1+H_b*high_water))+…
          (sg_TAF08_02_a/(1+H_a*high_water))+(sg_TAF08_02_g/(1+H_g*high_water))+…
          sg_TAF08_02_c))  { Outlier(0.05); };
   };
  };
  Sequence("Sector 2 Cal")
  {
   Combine("TAF10-17" )
   {
    TAF10_17_mg=Age(1000*mg_TAF10_17_de/((mg_TAF10_17_b/(1+H_b*high_water))+…
          (mg_TAF10_17_a/(1+H_a*high_water))+(mg_TAF10_17_g/(1+H_g*high_water))+…
          mg_TAF10_17_c))  { Outlier(0.5); };
   };
   Phase("Sector 2 above Calcite")
   {
    Combine("TAF10-18"  )
    {
     TAF10_18_mg=Age(1000*mg_TAF10_18_de/((mg_TAF10_18_b/(1+H_b*high_water))+…
          (mg_TAF10_18_a/(1+H_a*high_water))+(mg_TAF10_18_g/(1+H_g*high_water))+…
          mg_TAF10_18_c))  { Outlier(0.5); };
    };
    Combine("TAF09-27")
    {
     TAF09_27_mg=Age(1000*mg_TAF09_27_de/((mg_TAF09_27_b/(1+H_b*high_water))+…
          (mg_TAF09_27_a/(1+H_a*high_water))+(mg_TAF09_27_g/(1+H_g*high_water))+…
          mg_TAF09_27_c))  { Outlier(0.5); };
     TAF09_27_sg=Age(1000*sg_TAF09_27_de/((sg_TAF09_27_b/(1+H_b*high_water))+…
          (sg_TAF09_27_a/(1+H_a*high_water))+(sg_TAF09_27_g/(1+H_g*high_water))+…
          sg_TAF09_27_c))  { Outlier(0.05); };
    };
    Combine("TAF09-40")
    {
     TAF09_40_mg=Age(1000*mg_TAF09_40_de/((mg_TAF09_40_b/(1+H_b*high_water))+…
```

```
        (mg_TAF09_40_a/(1+H_a*high_water))+(mg_TAF09_40_g/(1+H_g*high_water))+…
        mg_TAF09_40_c))  { Outlier(0.05); };
   TAF09_40_sg=Age(1000*sg_TAF09_40_de/((sg_TAF09_40_b/(1+H_b*high_water))+…
        (sg_TAF09_40_a/(1+H_a*high_water))+(sg_TAF09_40_g/(1+H_g*high_water))+…
        sg_TAF09_40_c))  { Outlier(0.05); };
  };
 };
};
};
Boundary("Cal/LL");
Combine("TAF09-39")
{
 TAF09_39_vsa=Age(1000*vsa_TAF09_39_de/((vsa_TAF09_39_b/(1+H_b*high_water))+…
        (vsa_TAF09_39_a/(1+H_a*high_water))+(vsa_TAF09_39_g/(1+H_g*high_water))+…
        vsa_TAF09_39_c))  { Outlier(0.5); };
 TAF09_39_sg=Age(1000*sg_TAF09_39_de/((sg_TAF09_39_b/(1+H_b*high_water))+…
        (sg_TAF09_39_a/(1+H_a*high_water))+(sg_TAF09_39_g/(1+H_g*high_water))+…
        sg_TAF09_39_c))  { Outlier(0.5); };
};
Boundary();
Phase("TAF09-26&38")
{
 Combine("TAF09_26")
 {
  TAF09_26_mg=Age(1000*mg_TAF09_26_de/((mg_TAF09_26_b/(1+H_b*high_water))+…
        (mg_TAF09_26_a/(1+H_a*high_water))+(mg_TAF09_26_g/(1+H_g*high_water))+…
        mg_TAF09_26_c))  { Outlier(0.05); };
  TAF09_26_sg=Age(1000*sg_TAF09_26_de/((sg_TAF09_26_b/(1+H_b*high_water))+…
        (sg_TAF09_26_a/(1+H_a*high_water))+(sg_TAF09_26_g/(1+H_g*high_water))+…
        sg_TAF09_26_c))  { Outlier(0.05); };
 };
 Combine("TAF09-38"  )
 {
  TAF09_38_sg=Age(1000*sg_TAF09_38_de/((sg_TAF09_38_b/(1+H_b*high_water))+…
        (sg_TAF09_38_a/(1+H_a*high_water))+(sg_TAF09_38_g/(1+H_g*high_water))+…
        sg_TAF09_38_c))  { Outlier(0.5); };
 };
};
Boundary();
Combine("TAF09-37")
{
 TAF09_37_mg=Age(1000*mg_TAF09_37_de/((mg_TAF09_37_b/(1+H_b*high_water))+…
        (mg_TAF09_37_a/(1+H_a*high_water))+(mg_TAF09_37_g/(1+H_g*high_water))+…
        mg_TAF09_37_c))  { Outlier(0.05); };
 TAF09_37_sg=Age(1000*sg_TAF09_37_de/((sg_TAF09_37_b/(1+H_b*high_water))+…
        (sg_TAF09_37_a/(1+H_a*high_water))+(sg_TAF09_37_g/(1+H_g*high_water))+…
        sg_TAF09_37_c))  { Outlier(0.05); };
};
Combine("TAF09-36")
{
 TAF09_36_vsa=Age(1000*vsa_TAF09_36_de/((vsa_TAF09_36_b/(1+H_b*high_water))+…
        (vsa_TAF09_36_a/(1+H_a*high_water))+(vsa_TAF09_36_g/(1+H_g*high_water))+…
        vsa_TAF09_36_c))  { Outlier(0.05); };
 TAF09_36_sg=Age(1000*sg_TAF09_36_de/((sg_TAF09_36_b/(1+H_b*high_water))+…
        (sg_TAF09_36_a/(1+H_a*high_water))+(sg_TAF09_36_g/(1+H_g*high_water))+…
        sg_TAF09_36_c))  { Outlier(0.5); };
};
```

```
 Date("LL/Pink");
 Combine("TAF09-35")
 {
  TAF09_35_vsa=Age(1000*vsa_TAF09_35_de/((vsa_TAF09_35_b/(1+H_b*high_water))+…
         (vsa_TAF09_35_a/(1+H_a*high_water))+(vsa_TAF09_35_g/(1+H_g*high_water))+…
         vsa_TAF09_35_c))  { Outlier(0.5); };
  TAF09_35_sg=Age(1000*sg_TAF09_35_de/((sg_TAF09_35_b/(1+H_b*high_water))+…
         (sg_TAF09_35_a/(1+H_a*high_water))+(sg_TAF09_35_g/(1+H_g*high_water))+…
         sg_TAF09_35_c))  { Outlier(0.05); };
  Date("Pink");
 };
 Boundary("Top Sector 2");
};
Sequence()
{
 Boundary("Base Yellow");
 Phase("Sectors 3 and 8")
 {
  Sequence("Sector 3 micro")
  {
   Date( "Hiatus_High_MP");
   Combine("TAF10-07")
   {
    TAF10_07_mg=Age(1000*mg_TAF10_07_de/((mg_TAF10_07_b/(1+H_b*high_water))+…
         (mg_TAF10_07_a/(1+H_a*high_water))+(mg_TAF10_07_g/(1+H_g*high_water))+…
         mg_TAF10_07_c))  { Outlier(0.05); };
   };
   Date( "Y5");
   Combine("TAF10-06")
   {
    TAF10_06_mg=Age(1000*mg_TAF10_06_de/((mg_TAF10_06_b/(1+H_b*high_water))+…
         (mg_TAF10_06_a/(1+H_a*high_water))+(mg_TAF10_06_g/(1+H_g*high_water))+…
         mg_TAF10_06_c))  { Outlier(0.05); };
   };
   Combine("TAF10-05")
   {
    TAF10_05_mg=Age(1000*mg_TAF10_05_de/((mg_TAF10_05_b/(1+H_b*high_water))+…
         (mg_TAF10_05_a/(1+H_a*high_water))+(mg_TAF10_05_g/(1+H_g*high_water))+…
         mg_TAF10_05_c))  { Outlier(0.05); };
   };
   Combine("TAF10-02")
   {
    TAF10_02_mg=Age(1000*mg_TAF10_02_de/((mg_TAF10_02_b/(1+H_b*high_water))+…
         (mg_TAF10_02_a/(1+H_a*high_water))+(mg_TAF10_02_g/(1+H_g*high_water))+…
         mg_TAF10_02_c))  { Outlier(0.05); };
   };
  };
  Sequence("Sector 3 standard")
  {
   Combine("TAF09-01")
   {
    TAF09_01_mg=Age(1000*mg_TAF09_01_de/((mg_TAF09_01_b/(1+H_b*high_water))+…
         (mg_TAF09_01_a/(1+H_a*high_water))+(mg_TAF09_01_g/(1+H_g*high_water))+…
         mg_TAF09_01_c))  { Outlier(0.05); };
   };
   Combine("TAF08-10")
   {
```

```
 TAF08_10_mg=Age(1000*mg_TAF08_10_de/((mg_TAF08_10_b/(1+H_b*high_water))+…
        (mg_TAF08_10_a/(1+H_a*high_water))+(mg_TAF08_10_g/(1+H_g*high_water))+…
        mg_TAF08_10_c))  { Outlier(0.05); };
 };
 Combine("TAF08-11")
 {
 TAF08_11_mg=Age(1000*mg_TAF08_11_de/((mg_TAF08_11_b/(1+H_b*high_water))+…
        (mg_TAF08_11_a/ (1+H_a*high_water))+(mg_TAF08_11_g/(1+H_g*high_water))+…
        mg_TAF08_11_c))  { Outlier(0.05); };
 };
 Combine("Y5_both")
 {
  Date( "=Y5");
  Date("Y5_again");
 };
 Combine("TAF08-12")
 {
 TAF08_12_mg=Age(1000*mg_TAF08_12_de/((mg_TAF08_12_b/(1+H_b*high_water))+…
        (mg_TAF08_12_a/(1+H_a*high_water))+(mg_TAF08_12_g/(1+H_g*high_water))+…
        mg_TAF08_12_c))  { Outlier(0.05); };
 TAF08_12_sg=Age(1000*sg_TAF08_12_de/((sg_TAF08_12_b/(1+H_b*high_water))+…
        (sg_TAF08_12_a/(1+H_a*high_water))+(sg_TAF08_12_g/(1+H_g*high_water))+…
        sg_TAF08_12_c))  { Outlier(0.05); };
 };
 Combine("TAF08-13")
 {
 TAF08_13_mg=Age(1000*mg_TAF08_13_de/((mg_TAF08_13_b/(1+H_b*high_water))+…
        (mg_TAF08_13_a/(1+H_a*high_water))+(mg_TAF08_13_g/(1+H_g*high_water))+…
        mg_TAF08_13_c))  { Outlier(0.05); };
 TAF08_13_sg=Age(1000*sg_TAF08_13_de/((sg_TAF08_13_b/(1+H_b*high_water))+…
        (sg_TAF08_13_a/(1+H_a*high_water))+(sg_TAF08_13_g/(1+H_g*high_water))+…
        sg_TAF08_13_c))  { Outlier(0.05); };
 };
};
Sequence("Sector 8")
{
 Combine("TAF09_08")
 {
 TAF09_08_mg=Age(1000*mg_TAF09_08_de/((mg_TAF09_08_b/(1+H_b*high_water))+…
        (mg_TAF09_08_a/(1+H_a*high_water))+(mg_TAF09_08_g/(1+H_g*high_water))+…
        mg_TAF09_08_c))  { Outlier(0.05); };
 };
 Combine("TAF08_03")
 {
 TAF08_03_mg=Age(1000*mg_TAF08_03_de/((mg_TAF08_03_b/(1+H_b*high_water))+…
        (mg_TAF08_03_a/(1+H_a*high_water))+(mg_TAF08_03_g/(1+H_g*high_water))+…
        mg_TAF08_03_c))  { Outlier(0.05); };
 };
 Combine("TAF08_04")
 {
 TAF08_04_mg=Age(1000*mg_TAF08_04_de/((mg_TAF08_04_b/(1+H_b*high_water))+…
        (mg_TAF08_04_a/(1+H_a*high_water))+(mg_TAF08_04_g/(1+H_g*high_water))+…
        mg_TAF08_04_c))  { Outlier(0.05); };
 };
 Boundary();
 Phase()
 {
```

```
 Combine("TAF08_05")
 {
  TAF08_05_mg=Age(1000*mg_TAF08_05_de/((mg_TAF08_05_b/(1+H_b*high_water))+…
        (mg_TAF08_05_a/(1+H_a*high_water))+(mg_TAF08_05_g/(1+H_g*high_water))+…
        mg_TAF08_05_c))  { Outlier(0.05); };
 };
 Combine("TAF08_06")
 {
  TAF08_06_mg=Age(1000*mg_TAF08_06_de/((mg_TAF08_06_b/(1+H_b*high_water))+…
        (mg_TAF08_06_a/(1+H_a*high_water))+(mg_TAF08_06_g/(1+H_g*high_water))+…
        mg_TAF08_06_c))  { Outlier(0.05); };
 };
};
Boundary();
Phase()
{
 Combine("TAF08_14")
 {
  TAF08_14_mg=Age(1000*mg_TAF08_14_de/((mg_TAF08_14_b/(1+H_b*high_water))+…
        (mg_TAF08_14_a/(1+H_a*high_water))+(mg_TAF08_14_g/(1+H_g*high_water))+…
        mg_TAF08_14_c))  { Outlier(0.05); };
 };
 Combine("TAF08_15")
 {
  TAF08_15_mg=Age(1000*mg_TAF08_15_de/((mg_TAF08_15_b/(1+H_b*high_water))+…
        (mg_TAF08_15_a/(1+H_a*high_water))+(mg_TAF08_15_g/(1+H_g*high_water))+…
        mg_TAF08_15_c))  { Outlier(0.05); };
 };
};
Boundary();
Phase()
{
 Combine("TAF08_16")
 {
  TAF08_16_mg=Age(1000*mg_TAF08_16_de/((mg_TAF08_16_b/(1+H_b*high_water))+…
        (mg_TAF08_16_a/(1+H_a*high_water))+(mg_TAF08_16_g/(1+H_g*high_water))+…
        mg_TAF08_16_c))  { Outlier(0.05); };
 };
 Sequence()
 {
  After( )
  {
   Date("=Y5_both");
  };
  Combine("TAF10_14")
  {
   TAF10_14_mg=Age(1000*mg_TAF10_14_de/((mg_TAF10_14_b/(1+H_b*high_water))+…
        (mg_TAF10_14_a/(1+H_a*high_water))+(mg_TAF10_14_g/(1+H_g*high_water))+…
        mg_TAF10_14_c))  { Outlier(0.05); };
  };
  Date("Sector_8_transition");
 };
};
Boundary();
Combine("TAF10_11")
{
 TAF10_11_mg=Age(1000*mg_TAF10_11_de/((mg_TAF10_11_b/(1+H_b*high_water))+…
```

```
        (mg_TAF10_11_a/(1+H_a*high_water))+(mg_TAF10_11_g/(1+H_g*high_water))+…
        mg_TAF10_11_c))  { Outlier(0.05); };
 };
 };
};
Boundary("Yellow/Grey");
Phase("Grey Series")
{
 Sequence("Sector 8")
 {
  Combine("TAF10_10")
  {
   TAF10_10_mg=Age(1000*mg_TAF10_10_de/((mg_TAF10_10_b/(1+H_b*low_water))+…
        (mg_TAF10_10_a/(1+H_a*low_water))+(mg_TAF10_10_g/(1+H_g*low_water))+…
        mg_TAF10_10_c))  { Outlier(0.05); };
  };
  Combine("TAF09_25")
  {
   TAF09_25_mg=Age(1000*mg_TAF09_25_de/((mg_TAF09_25_b/(1+H_b*low_water))+…
        (mg_TAF09_25_a/(1+H_a*low_water))+(mg_TAF09_25_g/(1+H_g*low_water))+…
        mg_TAF09_25_c))  { Outlier(0.5); };
   TAF09_25_sg=Age(1000*sg_TAF09_25_de/((sg_TAF09_25_b/(1+H_b*low_water))+…
        (sg_TAF09_25_a/(1+H_a*low_water))+(sg_TAF09_25_g/(1+H_g*low_water))+…
        sg_TAF09_25_c))  { Outlier(0.5); };
  };
  Combine("TAF09_24")
  {
   TAF09_24_mg=Age(1000*mg_TAF09_24_de/((mg_TAF09_24_b/(1+H_b*low_water))+…
        (mg_TAF09_24_a/(1+H_a*low_water))+(mg_TAF09_24_g/(1+H_g*low_water))+…
        mg_TAF09_24_c))  { Outlier(0.5); };
   TAF09_24_sg=Age(1000*sg_TAF09_24_de/((sg_TAF09_24_b/(1+H_b*low_water))+…
        (sg_TAF09_24_a/(1+H_a*low_water))+(sg_TAF09_24_g/(1+H_g*low_water))+…
        sg_TAF09_24_c))  { Outlier(0.5); };
  };
 };
 Combine("TAF08_17")
 {
  TAF08_17_mg=Age(1000*mg_TAF08_17_de/((mg_TAF08_17_b/(1+H_b*low_water))+…
        (mg_TAF08_17_a/(1+H_a*low_water))+(mg_TAF08_17_g/(1+H_g*low_water))+…
        mg_TAF08_17_c))  { Outlier(0.05); };
 };
 };
 Boundary("Grey Surface");
};
Sequence(“Sector 9 only”)
{
 Boundary(“Base Sector 9”);
 Combine("TAF10-16")
 {
  TAF10_16_mg=Age(1000*mg_TAF10_16_de/((mg_TAF10_16_b/(1+H_b*high_water))+…
        (mg_TAF10_16_a/(1+H_a*high_water))+(mg_TAF10_16_g/(1+H_g*high_water))+…
        mg_TAF10_16_c))  { Outlier(0.05); };
 };
 Combine("TAF09-23")
 {
  TAF09_23_mg=Age(1000*mg_TAF09_23_de/((mg_TAF09_23_b/(1+H_b*high_water))+…
        (mg_TAF09_23_a/(1+H_a*high_water))+(mg_TAF09_23_g/(1+H_g*high_water))+…
```

```
        mg_TAF09_23_c))  { Outlier(0.05); };
 };
 Combine("TAF09-22")
 {
  TAF09_22_mg=Age(1000*mg_TAF09_22_de/((mg_TAF09_22_b/(1+H_b*high_water))+…
        (mg_TAF09_22_a/(1+H_a*high_water))+(mg_TAF09_22_g/(1+H_g*high_water))+…
        mg_TAF09_22_c))  { Outlier(0.05); };
 };
 Combine("TAF09-21")
 {
  TAF09_21_mg=Age(1000*mg_TAF09_21_de/((mg_TAF09_21_b/(1+H_b*high_water))+…
        (mg_TAF09_21_a/(1+H_a*high_water))+(mg_TAF09_21_g/(1+H_g*high_water))+…
        mg_TAF09_21_c))  { Outlier(0.05); };
 };
 Combine("TAF09-20")
 {
TAF09_20_mg=Age(1000*mg_TAF09_20_de/((mg_TAF09_20_b/(1+H_b*high_water))+…
        (mg_TAF09_20_a/(1+H_a*high_water))+(mg_TAF09_20_g/(1+H_g*high_water))+…
        mg_TAF09_20_c))  { Outlier(0.05); };
 };
 Boundary("Top Sector 9");
};
};
```

Dar es-Soltan I

```
 Options()
{ Resolution=200;};
Plot()
{
 N("SOL1_05_01_a", 0.038877415, 0.01);
 N("SOL1_05_02_a", 0.04687741, 0.01);
 N("SOL1_05_03_a", 0.044703589, 0.01);
 N("SOL1_05_04_a", 0.045943984, 0.01);
 N("SOL1_05_05A_a", 0.054250949, 0.01);
 N("SOL1_05_05B_a", 0.059481955, 0.01);
 N("SOL1_05_06_a", 0.055503859, 0.01);
 N("SOL1_05_07_a", 0.056405997, 0.01);
 N("SOL1_05_08_a", 0.055184374, 0.01);
 N("SOL1_05_09_a", 0.056731739, 0.01);
 N("SOL1_05_10_a", 0.05734568, 0.01);
 N("SOL1_05_11_a", 0.061041835, 0.01);
 N("SOL1_05_12_a", 0.056105284, 0.01);
 N("SOL1_05_13_a", 0.058567302, 0.01);
 N("SOL1_05_14_a", 0.053029326, 0.01);
 N("SOL1_05_15_a", 0.05086802, 0.01);
 N("SOL1_05_16_a", 0.043475709, 0.01);
 N("SOL1_05_17_a", 0.043187511, 0.01);
 N("SOL1_05_18_a", 0.051788931, 0.01);
 N("SOL1_05_21_a", 0.046908697, 0.01);
 N("DES08_22_a", 0.038263475, 0.01);
 N("DES08_24_a", 0.03610217, 0.01);
 N("DES08_31_a", 0.061348805, 0.01);
 N("DES08_32_a", 0.064136566, 0.01);
 N("DES08_33_a", 0.072474819, 0.01);
```

```
N("DES08_34_a", 0.063510111, 0.01);
N("DES08_35_a", 0.061662033, 0.01);
N("DES08_21_a", 0.041038721, 0.01);
N("SOL1_05_01_b", 0.197141884, 0.012588391);
N("SOL1_05_02_b", 0.480121698, 0.027351293);
N("SOL1_05_03_b", 0.506449783, 0.030528604);
N("SOL1_05_04_b", 0.44740524, 0.025272043);
N("SOL1_05_05A_b", 0.71085864, 0.04159291);
N("SOL1_05_05B_b", 0.802484411, 0.046214985);
N("SOL1_05_06_b", 0.764780173, 0.044815764);
N("SOL1_05_07_b", 0.666774076, 0.037241108);
N("SOL1_05_08_b", 1.34312218, 0.092809829);
N("SOL1_05_09_b", 1.22121047, 0.081117748);
N("SOL1_05_10_b", 1.362744113, 0.092659224);
N("SOL1_05_11_b", 1.407532776, 0.093853902);
N("SOL1_05_12_b", 1.140073762, 0.075234391);
N("SOL1_05_13_b", 1.062015867, 0.067242684);
N("SOL1_05_14_b", 0.787659663, 0.048065466);
N("SOL1_05_15_b", 0.659685848, 0.039216338);
N("SOL1_05_16_b", 0.447309721, 0.026414648);
N("SOL1_05_17_b", 0.332899979, 0.018860166);
N("SOL1_05_18_b", 1.142866017, 0.078705544);
N("SOL1_05_21_b", 0.415810867, 0.0249341);
N("DES08_22_b", 0.178266906, 0.012183929);
N("DES08_24_b", 0.151421515, 0.010124905);
N("DES08_31_b", 1.399616628, 0.09302975);
N("DES08_32_b", 1.118793168, 0.067848819);
N("DES08_33_b", 1.547825202, 0.096932345);
N("DES08_34_b", 1.258568611, 0.079734087);
N("DES08_35_b", 0.898002999, 0.052104664);
N("DES08_21_b", 0.233384996, 0.014884605);
N("SOL1_05_01_g", 0.25791, 0.009029471);
N("SOL1_05_02_g", 0.33232, 0.014772655);
N("SOL1_05_03_g", 0.35087, 0.01436033);
N("SOL1_05_04_g", 0.40871, 0.014031113);
N("SOL1_05_05A_g", 0.49984, 0.021433828);
N("SOL1_05_05B_g", 0.49984, 0.025366682);
N("SOL1_05_06_g", 0.60306, 0.022055407);
N("SOL1_05_07_g", 0.47520, 0.022147);
N("SOL1_05_08_g", 0.78965, 0.031409003);
N("SOL1_05_09_g", 0.75652, 0.029395779);
N("SOL1_05_10_g", 0.77980, 0.032142458);
N("SOL1_05_11_g", 0.77538, 0.033949407);
N("SOL1_05_12_g", 0.64378, 0.028129402);
N("SOL1_05_13_g", 0.62451, 0.027839652);
N("SOL1_05_14_g", 0.53224, 0.02142656);
N("SOL1_05_15_g", 0.46880, 0.018969425);
N("SOL1_05_16_g", 0.24065, 0.012899912);
N("SOL1_05_17_g", 0.20388, 0.011783612);
N("SOL1_05_18_g", 0.71735, 0.027118264);
N("SOL1_05_21_g", 0.34613, 0.015863481);
N("DES08_22_g", 0.150682858, 0.008888444);
N("DES08_24_g", 0.123322858, 0.007273238);
N("DES08_31_g", 0.66614, 0.033933132);
N("DES08_32_g", 0.736740017, 0.030274337);
N("DES08_33_g", 0.65925, 0.039562268);
N("DES08_34_g", 0.624790.032209999);
```

```
N("DES08_35_g", 0.52427, 0.02657581);
N("DES08_21_g", 0.19563143, 0.010677586);
N("SOL1_05_01_c", 0.068812274, 0.034);
N("SOL1_05_02_c", 0.070712186, 0.035);
N("SOL1_05_03_c", 0.071586115, 0.035);
N("SOL1_05_04_c", 0.074137244, 0.037);
N("SOL1_05_05A_c", 0.075628668, 0.037);
N("SOL1_05_05B_c", 0.075628668, 0.037);
N("SOL1_05_06_c", 0.078209416, 0.039);
N("SOL1_05_07_c", 0.079396097, 0.039);
N("SOL1_05_08_c", 0.081223833, 0.040);
N("SOL1_05_09_c", 0.084077361, 0.042);
N("SOL1_05_10_c", 0.08639423, 0.043);
N("SOL1_05_11_c", 0.088103817, 0.044);
N("SOL1_05_12_c", 0.090577087, 0.045);
N("SOL1_05_13_c", 0.097793699, 0.048);
N("SOL1_05_14_c", 0.103626362, 0.051);
N("SOL1_05_15_c", 0.108917761, 0.054);
N("SOL1_05_16_c", 0.122047187, 0.061);
N("SOL1_05_17_c", 0.066889212, 0.033);
N("SOL1_05_18_c", 0.087072487, 0.043);
N("SOL1_05_21_c", 0.23236061, 0.056494506);
N("DES08_22_c", 0.066889212, 0.033);
N("DES08_24_c", 0.063264469, 0.031);
N("DES08_31_c", 0.083431303, 0.041);
N("DES08_32_c", 0.0796967, 0.039);
N("DES08_33_c", 0.077916628, 0.038);
N("DES08_34_c", 0.07507142, 0.037);
N("DES08_35_c", 0.073703275, 0.036);
N("DES08_21_c", 0.068812274, 0.034);
N("SOL1_05_01_de", 72.24448203, 4.829079159);
N("SOL1_05_02_de", 84.53489749, 4.580899187);
N("SOL1_05_03_de", 85.56376486, 5.410779546);
N("SOL1_05_04_de", 111.9646129, 6.692576221);
N("SOL1_05_05A_de", 116.0592312, 4.799493945);
N("SOL1_05_05B_de", 129.2268156, 9.12991876);
N("SOL1_05_06_de", 145.5342046, 8.014823431);
N("SOL1_05_07_de", 112.3155118, 8.44420169);
N("SOL1_05_08_de", 142.6587793, 4.361676127);
N("SOL1_05_09_de", 162.7702275, 11.08151939);
N("SOL1_05_10_de", 188.0886763, 10.24423913);
N("SOL1_05_11_de", 135.1520097, 5.993591844);
N("SOL1_05_12_de", 94.79548343, 3.794593385);
N("SOL1_05_13_de", 82.57826157, 5.274628024);
N("SOL1_05_14_de", 40.86041629, 2.162567563);
N("SOL1_05_15_de", 9.42053759, 0.382361387);
N("SOL1_05_16_de", 4.701102135, 0.087487337);
N("SOL1_05_17_de", 71.73437353, 9.212707636);
N("SOL1_05_18_de", 122.0727271, 8.527663707);
N("SOL1_05_21_de", 153.5965378, 17.73133107);
N("DES08_22_de", 47.91051008, 8.049545674);
N("DES08_24_de", 34.87646178, 2.378330822);
N("DES08_31_de", 124.5393887, 8.76598695);
N("DES08_32_de", 130.1788996, 6.998574504);
N("DES08_33_de", 145.4701803, 11.19099704);
N("DES08_34_de", 97.23752163, 5.353406726);
N("DES08_35_de", 110.6019383, 8.142351785);
```

```
N("SOL1_05_01_H2O", 0.052631579, 0.026);
N("SOL1_05_02_H2O", 0.128720238, 0.063700469);
N("SOL1_05_03_H2O", 0.205436893, 0.072653905);
N("SOL1_05_04_H2O", 0.239215686, 0.076782776);
N("SOL1_05_05A_H2O", 0.156640625, 0.066890877);
N("SOL1_05_05B_H2O", 0.156640625, 0.066890877);
N("SOL1_05_06_H2O", 0.181491465, 0.069796104);
N("SOL1_05_07_H2O", 0.194869487, 0.071385655);
N("SOL1_05_08_H2O", 0.140463282, 0.065032825);
N("SOL1_05_09_H2O", 0.193801781, 0.071258135);
N("SOL1_05_10_H2O", 0.155233069, 0.066728172);
N("SOL1_05_11_H2O", 0.128656915, 0.063693322);
N("SOL1_05_12_H2O", 0.171455488, 0.068615398);
N("SOL1_05_13_H2O", 0.140549978, 0.065042713);
N("SOL1_05_14_H2O", 0.062462098, 0.031);
N("SOL1_05_15_H2O", 0.051570836, 0.025);
N("SOL1_05_16_H2O", 0.135662063, 0.064486416);
N("SOL1_05_17_H2O", 0.017293439, 0.0086);
N("SOL1_05_18_H2O", 0.10990991, 0.054);
N("SOL1_05_21_H2O", 0.002111765, 0.0010);
N("DES08_22_H2O", 0.031075697, 0.015);
N("DES08_24_H2O", 0.035143109, 0.017);
N("DES08_31_H2O", 0.074248313, 0.037);
N("DES08_32_H2O", 0.172360591, 0.068721468);
N("DES08_33_H2O", 0.138192863, 0.06477415);
N("DES08_34_H2O", 0.118178658, 0.059);
N("DES08_35_H2O", 0.106069534, 0.053);
N("DES08_21_H2O", 0.052631579, 0.026);
//correction factors
N("H_a", 1.5,.05*1.5 );
N("H_b", 1.25,.05*1.25 );
N("H_g",1.14 , .05*1.14);
Sequence()
{
 Boundary();
 Phase("Group 1")
 {
  DES08_24_mg=Age(1000*DES08_24_de/((DES08_24_b/(1+H_b*DES08_24_H2O))+…
          (DES08_24_a/(1+H_a* DES08_24_H2O))+(DES08_24_g/(1+H_g* DES08_24_H2O))+…
          DES08_24_c));
  SOL1_05_17_mg=Age(1000*SOL1_05_17_de/((SOL1_05_17_b/(1+H_b*SOL1_05_17_H2O))+…
          (SOL1_05_17_a/(1+H_a* SOL1_05_17_H2O))+(SOL1_05_17_g/(1+H_g* SOL1_05_17_H2O))+…
           SOL1_05_17_c));
  DES08_22_mg=Age(1000*DES08_22_de/((DES08_22_b/(1+H_b*DES08_22_H2O))+…
          (DES08_22_a/(1+H_a* DES08_22_H2O))+(DES08_22_g/(1+H_g* DES08_22_H2O))+ …
          DES08_22_c));
  SOL1_05_01_mg=Age(1000*SOL1_05_01_de/((SOL1_05_01_b/(1+H_b*SOL1_05_01_H2O))+…
          (SOL1_05_01_a/(1+H_a* SOL1_05_01_H2O))+…(SOL1_05_01_g/(1+H_g* SOL1_05_01_H2O))+…
           SOL1_05_01_c));
  SOL1_05_02_mg=Age(1000*SOL1_05_02_de/((SOL1_05_02_b/(1+H_b*SOL1_05_02_H2O))+…
          (SOL1_05_02_a/(1+H_a* SOL1_05_02_H2O))+(SOL1_05_02_g/(1+H_g* SOL1_05_02_H2O))+ …
          SOL1_05_02_c));
  SOL1_05_03_mg=Age(1000*SOL1_05_03_de/((SOL1_05_03_b/(1+H_b*SOL1_05_03_H2O))+…
          (SOL1_05_03_a/(1+H_a* SOL1_05_03_H2O))+(SOL1_05_03_g/(1+H_g* SOL1_05_03_H2O))+…
           SOL1_05_03_c));
  SOL1_05_04_mg=Age(1000*SOL1_05_04_de/((SOL1_05_04_b/(1+H_b*SOL1_05_04_H2O))+…
          (SOL1_05_04_a/(1+H_a* SOL1_05_04_H2O))+(SOL1_05_04_g/(1+H_g* SOL1_05_04_H2O))+ …
```

```
        SOL1_05_04_c));
};
Boundary("G1G2 Transition");
Phase("Group 2")
{
 DES08_35_mg=Age(1000*DES08_35_de/((DES08_35_b/(1+H_b*DES08_35_H2O))+…
        (DES08_35_a/(1+H_a* DES08_35_H2O))+(DES08_35_g/(1+H_g* DES08_35_H2O))+…
         DES08_35_c));
 DES08_34_mg=Age(1000*DES08_34_de/((DES08_34_b/(1+H_b*DES08_34_H2O))+…
        (DES08_34_a/(1+H_a* DES08_34_H2O))+(DES08_34_g/(1+H_g* DES08_34_H2O))+…
         DES08_34_c));
SOL1_05_05A_mg=Age(1000*SOL1_05_05A_de/((SOL1_05_05A_b/(1+H_b*SOL1_05_05A_H2O))+…
        (SOL1_05_05A_a/(1+H_a* SOL1_05_05A_H2O))+…
        (SOL1_05_05A_g/(1+H_g* SOL1_05_05A_H2O))+ SOL1_05_05A_c));
 SOL1_05_05B_mg=Age(1000*SOL1_05_05B_de/((SOL1_05_05B_b/(1+H_b*SOL1_05_05B_H2O))+…
        (SOL1_05_05B_a/(1+H_a* SOL1_05_05B_H2O))+…
        (SOL1_05_05B_g/(1+H_g* SOL1_05_05B_H2O))+ SOL1_05_05B_c));
 SOL1_05_06_mg=Age(1000*SOL1_05_06_de/((SOL1_05_06_b/(1+H_b*SOL1_05_06_H2O))+…
        (SOL1_05_06_a/(1+H_a* SOL1_05_06_H2O))+(SOL1_05_06_g/(1+H_g* SOL1_05_06_H2O))+ …
        SOL1_05_06_c));
 DES08_33_mg=Age(1000*DES08_33_de/((DES08_33_b/(1+H_b*DES08_33_H2O))+…
        (DES08_33_a/(1+H_a* DES08_33_H2O))+(DES08_33_g/(1+H_g* DES08_33_H2O))+…
        DES08_33_c));
 SOL1_05_07_mg=Age(1000*SOL1_05_07_de/((SOL1_05_07_b/(1+H_b*SOL1_05_07_H2O))+…
        (SOL1_05_07_a/(1+H_a* SOL1_05_07_H2O))+(SOL1_05_07_g/(1+H_g* SOL1_05_07_H2O))+ …
        SOL1_05_07_c));
DES08_32_mg=Age(1000*DES08_32_de/((DES08_32_b/(1+H_b*DES08_32_H2O))+…
        (DES08_32_a/(1+H_a* DES08_32_H2O))+(DES08_32_g/(1+H_g* DES08_32_H2O))+ …
        DES08_32_c));
};
Boundary("G2G3 Transition");
Phase("Group 3")
{
 SOL1_05_08_mg=Age(1000*SOL1_05_08_de/((SOL1_05_08_b/(1+H_b*SOL1_05_08_H2O))+…
        (SOL1_05_08_a/(1+H_a* SOL1_05_08_H2O))+(SOL1_05_08_g/(1+H_g* SOL1_05_08_H2O))+ …
        SOL1_05_08_c));
 DES08_31_mg=Age(1000*DES08_31_de/((DES08_31_b/(1+H_b*DES08_31_H2O))+...
        (DES08_31_a/(1+H_a* DES08_31_H2O))+(DES08_31_g/(1+H_g* DES08_31_H2O))+…
        DES08_31_c));
 SOL1_05_09_mg=Age(1000*SOL1_05_09_de/((SOL1_05_09_b/(1+H_b*SOL1_05_09_H2O))+…
        (SOL1_05_09_a/(1+H_a* SOL1_05_09_H2O))+(SOL1_05_09_g/(1+H_g* SOL1_05_09_H2O))+…
        SOL1_05_09_c));
 SOL1_05_10_mg=Age(1000*SOL1_05_10_de/((SOL1_05_10_b/(1+H_b*SOL1_05_10_H2O))+…
        (SOL1_05_10_a/(1+H_a* SOL1_05_10_H2O))+(SOL1_05_10_g/(1+H_g* SOL1_05_10_H2O))+ …
        SOL1_05_10_c ));
 SOL1_05_18_mg=Age(1000*SOL1_05_18_de/((SOL1_05_18_b/(1+H_b*SOL1_05_18_H2O))+…
        (SOL1_05_18_a/(1+H_a* SOL1_05_18_H2O))+(SOL1_05_18_g/(1+H_g* SOL1_05_18_H2O))+…
        SOL1_05_18_c));
 SOL1_05_11_mg=Age(1000*SOL1_05_11_de/((SOL1_05_11_b/(1+H_b*SOL1_05_11_H2O))+…
        (SOL1_05_11_a/(1+H_a* SOL1_05_11_H2O))+(SOL1_05_11_g/(1+H_g* SOL1_05_11_H2O))+…
        SOL1_05_11_c));
};
Boundary("G3G4 Transition");
Phase("Group 4")
{
 SOL1_05_12_mg=Age(1000*SOL1_05_12_de/((SOL1_05_12_b/(1+H_b*SOL1_05_12_H2O))+…
        (SOL1_05_12_a/(1+H_a* SOL1_05_12_H2O))+(SOL1_05_12_g/(1+H_g* SOL1_05_12_H2O))+ …
```

```
        SOL1_05_12_c));
 SOL1_05_13_mg=Age(1000*SOL1_05_13_de/((SOL1_05_13_b/(1+H_b*SOL1_05_13_H2O))+…
        (SOL1_05_13_a/(1+H_a* SOL1_05_13_H2O))+(SOL1_05_13_g/(1+H_g* SOL1_05_13_H2O))+ …
        SOL1_05_13_c));
 };
 Boundary("G4G5 Transition");
 Phase("Group 5")
 {
 SOL1_05_14_mg=Age(1000*SOL1_05_14_de/((SOL1_05_14_b/(1+H_b*SOL1_05_14_H2O))+…
        (SOL1_05_14_a/(1+H_a* SOL1_05_14_H2O))+(SOL1_05_14_g/(1+H_g* SOL1_05_14_H2O))+ …
        SOL1_05_14_c));
 SOL1_05_15_mg=Age(1000*SOL1_05_15_de/((SOL1_05_15_b/(1+H_b*SOL1_05_15_H2O))+…
        (SOL1_05_15_a/(1+H_a* SOL1_05_15_H2O))+(SOL1_05_15_g/(1+H_g* SOL1_05_15_H2O))+ …
        SOL1_05_15_c));
 SOL1_05_16_mg=Age(1000*SOL1_05_16_de/((SOL1_05_16_b/(1+H_b*SOL1_05_16_H2O))+…
        (SOL1_05_16_a/(1+H_a* SOL1_05_16_H2O))+(SOL1_05_16_g/(1+H_g* SOL1_05_16_H2O))+ …
        SOL1_05_16_c));
 };
 Boundary();
};
};
```

Appendix C: Chaperon Rouge II measurement details

Equivalent dose measurement and dosimetry calculations for the sample CR 724b1 are summarized here. All information has been obtained from Rhodes (1990).

Sample preparation was essentially the same the procedure used in this study, comprising dry or wet sieving, carbonate removal with HCl, HF etching, HCl to dissolve fluorides, acetone, and drying. According to the thesis, second sieving—to remove grain fragments after etching—was adopted part of the way through the study, so it is unclear whether the CR samples were second sieved. Samples were also density separated with sodium polytungstate (2.67 g cm^{-3}), and the lighter fraction was retained as quartz.

The thesis is unclear concerning the exact grain size fraction chosen for dating this particular sample. Possible size fractions mentioned include 90-125 µm, 125-180 µm and 180-250 µm (rarely). Grains were mounted in a monolayer upon stainless steel discs either with Rüsch Silkospray (90-125 µm) or Viscasil 60,000. Beta irradiation for equivalent dose estimation was provided by several manual or automated ^{90}Sr-^{90}Y sources, which were calibrated with gamma-irradiated aliquots of 90-125 µm quartz. Preheats were conducted by storing aliquots on an aluminum tray that was itself contained within an aluminum heat sink in a laboratory oven. Afterwards, aliquots were removed and left to cool at room temperature on another aluminum slab. In addition to natural sunlight, two solar simulators, an Oriel 300 W filtered xenon lamp and a Hönle Sol 2 doped mercury vapor tube, were used to bleach aliquots.

OSL measurements were made using selected components bolted to an optical table (Table C-1). A 514.4 nm argon-ion laser provided stimulation light, which was focused and guided into selected measurement chambers via a series of mirrors, prisms, lenses, and pinhole apertures. Laser power was monitored with a photodiode and adjusted manually when necessary. A Corning 7-52 filter in the beam line and an Ealing 514.5 Δ 10 nm interference filter at the entrance to the measurement chamber cut out blue plasma light. Within the

TABLE C-1. Sample measurement parameters for all samples from Chaperon Rouge I and II (Excerpted from Rhodes, 1990: Table 6.1). The starred sample has been remeasured for this thesis.

Sample	P0 (mW cm^{-2})	T0 (s)	PMT0	B1	BT1 (min)	D1 (Gy)	P1 (mW cm^{-2})	T1 (s)	PMT1	B2	BT2 (min)	D2 (Gy)	P2 (mW cm^{-2})	T2 (s)	PMT2	B3	BT3 (min)	P3 (mW cm^{-2})	T3	PMT3
724 g2 (i)	4.3	0.05	B	O	15	21	4.3	90	B	-	-	-	-	-	-	-	-	-	-	-
724 g2 (ii)	4.3	0.10	B	O	75	75	4.3	90	B	-	-	-	-	-	-	-	-	-	-	-
724 b1*	7.2	0.10	E	H	20	100	36	50	E	-	-	-	-	-	-	-	-	-	-	-
724 c1	7.2	0.10	E	S	15	25	36	100	E	S	15	5	36	10	E	H	100	36	100	E
724 d1	7.2	0.50	E	H	25	20	36	50	E	-	-	-	-	-	-	-	-	-	-	-
724 e1	7.2	0.50	E	H	25	20	36	50	E	-	-	-	-	-	-	-	-	-	-	-

Key:

PMT0/1/2/3—emission filters
- B: 4 x 7-59
- E: 6 x 7-59 + 2 mm BG 39

B1/2/3—bleaching sources
- S: natural sunlight
- O: Oriel solar simulator
- H: Hönle SOL 2?

measurement chamber, various combinations of mirrors and sample holders provided optical stimulation at room temperature. Several combinations of emission filter were used (varying stringencies), and an EMI 9635Q PMT measured emission intensity.

Aliquots were organized into batches for preheating and measurement so any systematic changes in the equipment would increase scatter rather than systematically offset the estimated equivalent dose. Experiments showed that scatter due to equipment variation and the movement of aliquots between stations was less than that induced by intrinsic aliquot intensity scatter. Equivalent dose measurements for age calculation were made via an additive dose technique, in which a single dose response curve is created from the luminescence responses of several tens of discs. PMT dark counts and background levels were subtracted from the OSL emissions. The net signal was then normalized to account for intensity differences by one of two methods:

1) Natural normalization: Aliquots are normalized by the intensity of a short-shine OSL measurement prior to any other treatment. The laser exposure time is chosen to deplete the initial signal by less than 5%, and the final equivalent dose is corrected to take this small depletion into account.

2) Dose normalization: After measurement and bleaching of the OSL emissions due to natural or laboratory irradiation, a standard dose (between 2 and 10 Gy) is given. The aliquots are preheated, and the OSL (first several seconds) due to the standard dose is measured then used as a normalization value after dark and background subtraction.

Each additive dose response curve was fit with either linear or exponential functions for extrapolation of the equivalent dose. All equivalent dose estimates for the sample were used to create a shine plateau. The mean of those equivalent doses falling in the plateau was chosen as the final equivalent dose. Regeneration dose response curves were also measured to investigate growth curve characteristics and saturation levels. TL glow curves were obtained to identify any samples with feldspar contamination, and these were rejected from the date calculations.

Dose rates were estimated for Chaperon Rouge II samples based on two on-site measurement techniques: use of a 4-channel portable gamma spectrometer from Harwell and burial of 'Oxford' calcium fluoride dosimetry capsules. The gamma spectrometer was calibrated using doped concrete blocks, and performance was tested by measurement of a radium or monazite source both before and after field measurements. Correction for attenuation due to present day water content was made via standard methods. Dosimeter capsules comprised copper casings filled with calcium fluoride, which were thermally reset by heating to at least $350^{o}C$ immediately prior to burial. After twelve months, capsules were retrieved, and returned to the laboratory. Dose deposited during travel from the site to the laboratory was measured by an accompanying capsule and subtracted. Measured burial dose was corrected for attenuation effects of the capsule wall (a factor of 1.1), a self dose rate of 0.1 Gy ka-1, and incident cosmic ray dose.

Elemental concentrations of K, Th, and U were estimated from on-site gamma spectrometer measurements, allowing the calculation of alpha and beta dose rates in addition to direct measurement of gamma dose rate. Though alpha counting of several quartz extracts indicated no detectable dose above background (0.1 c ks-1), a value of 5% of the bulk alpha dose rate was included as an internal alpha contribution. Alpha calculations assumed an a-value of 0.1. Cosmic dose rates for this site were estimated based on Prescott and Stephan (1982). Grain size attenuation was based on the values of Mejdahl (1979). Present day water content was estimated via standard methods, i.e. gravimetric analysis of sample ends. Water content attenuation values were taken from Aitken (1985), and burial history water content estimates were based upon estimates of saturated water content (based on porosity calculations from tube sample density) and discussion with archaeologists and geologists. All reported values for the Chaperon Rouge II dose rate estimates are given in Table C-2. It seems that calculations were made with the assumption of decay series equilibrium, as no mention is made of disequilibrium values for this site or the neighboring site, Chaperon Rouge I.

TABLE C-2. Calculated dose rates, equivalent dose, and age calculated by Rhodes (1990) for samples from Chaperon Rouge I and II. Excerpted from Tables 6-4 and B.3 (Rhodes, 1990).

Sample	4 ch. γ-spec. (Gy ka-1)	Estimated Cosmic Dose (Gy ka-1)	Capsule (Total) (Gy ka-1)	Capsule (Corrected) (Gy ka-1)	Total Dose Rate (Gy ka-1)	De (Gy)	Age (ka)
724b1	0.47	0.14	0.64	0.44	1.12 ± 0.08	46.0 ± 6.0	41.1±6.1
724c1	0.24	0.15	--	--	0.65 ± 0.06	17.3 ± 1.0	26.6±2.9
724d1	0.23	0.16	0.48	0.25	0.65 ± 0.06	7.8 ± 0.5	12.0±1.3
724e1	0.25	0.19	0.46	0.18	0.66 ± 0.06	2.7 ± 0.9	4.1±1.4